MICROCRACKS INDUCE OSTEOBLAST ALIGNMENT AND MATURATION ON HYDROXYAPATITE SCAFFOLDS

By

Yutian Shu

A DISSERTATION

Submitted to
Michigan State University
in partial fulfillment of the requirements
for the degree of

DOCTOR OF PHILOSOPHY

Chemical Engineering and Materials Science

2012

ABSTRACT

MICROCRACKS INDUCE OSTEOBLAST ALIGNMENT AND MATURATION ON HYDROXYAPATITE SCAFFOLDS

By

Yutian Shu

Physiological bone tissue is a mineral/collagen composite with a hierarchical structure. The features in bone, such as mineral crystals, fibers, and pores can range from the nanometer to the centimeter in size. Currently available bone tissue scaffolds primarily address the chemical composition, pore size, and pore size distribution. While these design parameters are extensively investigated for mimicking bone function and inducing bone regeneration, little is known about microcracks, which is a prevalent feature found in fractured bone *in vivo* and associated with fracture healing and repair. Since the purpose of bone tissue engineering scaffold is to enhance bone regeneration, the coincidence of microcracks and bone densification should not be neglected but rather be considered as a potential parameter in bone tissue engineering scaffold design.

The purpose of this study is to test the hypothesis that microcracks enhance bone healing. *In vitro* studies were designed to investigate the osteoblast (bone forming cells) response to microcracks in dense (94%) hydroxyapatite substrates. Microcracks were introduced using a well-established Vickers indentation technique. The results of our study showed that microcracks induced osteoblast alignment, enhanced osteoblast attachment and more rapid maturation. These findings may provide insight into fracture healing mechanism(s) as well as improve the design of bone tissue engineering orthopedic scaffolds for more rapid bone regeneration.

ACKNOWLEDGMENTS

I would like to thank my advisor, Professor Melissa Baumann for her guidance during my pursuit of doctoral degree. She provided me opportunities to participate in various research activities, gave me chance to meet people with professional knowledge in related fields of endeavor. She also taught me how to think critically, how to work with undergraduate students, and helped me with improving my English as a second language.

I would also like to thank Professor Eldon Case for sharing his wealthy knowledge and enlightening ideas with me, and for advice on becoming a devoted, honest and efficient researcher. I also appreciate Professor Laura McCabe and Professor Jeff Sakamoto for their help and suggestions on my coursework and research.

Last but not least, I would like to thank all my lab coworkers, Chelsea House, Craig Pearson, Fei Ren, Kaitlin Tyler, Marc Schlaud, Megan Buczkow, Rob Friederichs, Sarah Meyer, and Xiaofeng Fan, for their assistance during the completion of my research.

TABLE OF CONTENTS

LIST OF TABLES……………………………………………………………….9

LIST OF FIGURES…………………………………………………………….10

CHAPTER 1
INTRODUCTION……………………………………………………………….1
    References………………………………………………………………….4

CHAPTER 2
BACKGROUND………………………………………………………………...6
    The composition and structure of bone…………………………………..6
    Microcracking in bone……………………………………………………….9
    Bone remodeling and osteoblast function………………………………..12
    Biomaterials surface properties affecting osteoblasts……………………..14
    Hydroxyapatite applications……………………………………………….17
    Residual stress and microcracking………………………………………..19
    Vickers micro-indentation…………………………………………………..22
    References…………………………………………………………………..30

CHAPTER 3
CELL CULTURING PROTOCOLS……………………………………………39
    Thawing……………………………………………………………………...39
    Feeding……………………………………………………………………….40
    Splitting……………………………………………………………………….40
    Freezing……………………………………………………………………...41
    Sterilize handling…………………………………………………………….42
    References…………………………………………………………………...44

CHAPTER 4
MICROCRACKS INDUCE OSTEOBLAST ALIGNMENT AND ACCELERATE
MATURATION ON HYDROXYAPATITE SCAFFOLDS………………………..46
    Abstract……………………………………………………………………….46
    Introduction and background……………………………………………….47
    Materials and methods……………………………………………………...51
        HA specimen preparation…………………………………………….51
        HA characterization…………………………………………………...52
        Cell culture…………………………………………………………….53
        OB attachment and growth…………………………………………...53
        OB maturation…………………………………………………………..54
        CLSM imaging of OBs………………………………………………...55
    Statistics……………………………………………………………………...55
    Results………………………………………………………………………..56
        HA characterization…………………………………………………...56
        OB attachment and alignment………………………………………..58

OB attachment……………………………………………………..58
CLSM micrographs of OB attachment at four hours…………60
Alignment angle (θ) distribution……………………………..62
Comparison of aligned and non-aligned cells………………..64
The positions of aligning cells on microcracked HA…………65
OB growth and maturation……………………………………….67
Discussion…………………………………………………………………...70
OB attachment and growth……………………………………….70
OB shape on the CLSM micrographs……………………………72
Distribution of OB alignment angles……………………………..73
OB alignment towards the microcracked zone……………………73
Relationship between aggregated aligned cells and the size of microcracked zone………………………………………………...76
Microcrack boundary defined by radial/lateral cracks……………77
OB maturation………………………………………………………..79
Conclusion……………………………………………………………………..80
References……………………………………………………………………..82

CHAPTER 5
MICROCRACKS ACCELERATE CALLCIUM RELEASE FROM HYDROXYAPATITE…………………………………………………………………..94
Introduction………………………………………………………………….94
Materials and methods……………………………………………………..95
Results and discussion……………………………………………………..97
Conclusion…………………………………………………………………102
References…………………………………………………………………103

CHAPTER 6
CLSM OF CALCIUM PHOSPHATE PRECIPITATION FROM CRACKED HYDROXYAPATITE………………………………………………………………107
Introduction…………………………………………………………………107
Materials and methods……………………………………………………107
Results and discussion……………………………………………………108
Conclusions…………………………………………………………………110
References…………………………………………………………………112

CHAPTER 7
OSTEOBLAST SPATIAL DISTRIBUTION AFTER 1, 2, AND 4 HOURS ATTACHMENT………………………………………………………………………114
References…………………………………………………………………120

CHAPTER 8
SLOW GROWTH OF MICROCRACKS IN HYDROXYAPATITE INTRODUCED BY MICROINDENTATION………………………………………………………122
Abstract………………………………………………………………………122
Introduction and background……………………………………………..123
Experiment procedure……………………………………………………126
Materials and characterization methods…………………………126
Vickers indentation and crack length measurement…………….127
Results and discussion……………………………………………………128

Material characterization……………………………………………..128
E, H, and K_c for HA specimens……………………………………129
Load dependence of initial radial and lateral crack length……...130
Radial crack growth and perturbation from lateral cracks during aging……………………………………………………………133
Load dependent exponential growth of radial cracks………133
Perturbation from lateral crack……………………………..136
Other factors that may affect the growth of radial cracks……….139
Summary and Conclusions………………………………………………141
Appendix A………………………………………………………………143
References………………………………………………………………146

CHAPTER 9

SUMMARY AND FUTURE DIRECTIONS…………………………………..154

APPENDICES

APPENDIX A BONE RESPONSE TO MECHANICAL STIMULI AND THE LOCAL STRAIN-CUE HYPOTHESIS……………………………………….158

APPENDIX B CALCIUM CONCENTRATION MEASUREMENT USING ATOMIC ABSORPTION SPECTROSCOPY………………………………..164

APPENDIX C SOLID STATE SINTERING OF HYDROXYAPTITIE AT 1360℃………………………………………………………………….. ..166

REFERENCES……………………………………………………………170

LIST OF TABLES

Table 2.1 Chemical compositions of bone measured by Berzelius……………..6

Table 2.2 Comparison of the mechanical properties of long bone and common biomaterials used for bone replacement………………………………………..8

Table 7.1 Goodness of fitting tests for cell distribution data on non-cracked HA……………………………………………………………………………….117

Table 7.2 Goodness of fitting tests for cell distribution data on cracked HA...119

Table C-1 List of sintering profile, density, porosity and volume change……169

LIST OF FIGURES

Figure 2.1 Longitude femur section showing trabecular and cortical bone. Photo taken by Paul Crompton [2011] at University of Wales College of Medicine. For interpretation of the references to color in this and all other figures, the reader is referred to the electronic version of this dissertation……………………………………………………………………..8

Figure 2.2 Illustration of the surface contact angle of water drop on an ideal solid surface surrounded by gas……………………………………………….16

Figure 2.3 Elastic/plastic indention model of spherical symmetry with a hydrostatic core near contact region with indenter, plastic deformation zone" around the hydrostatic core, and elastic matrix………………………………23

Figure 2.4 (A) Elastic/plastic combination at maximum load P which is a summation of (B) reversible elastic component at load P and (C) irreversible residual component after unloading…………………………………………...24

Figure 2.5 Elastic/plastic sharp contact indentation generates median, radial and lateral cracks……………………………………………………………..25

Figure 2.6 Residual component of stress field below indentation which remains upon unloading and lateral crack of distance h below the free surface. The dashed lines depict the median/radial crack system…………………………28

Figure 4.1 (a) Radial cracks introduced by Vickers indentation at 4.91 N; (b) A 7×7 grid with a 2 mm interval indentation pattern on HA specimens…………52

Figure 4.2 XRD spectra of as-received HA powder from vendor and pulverized sintered HA specimen. Both powders showed representative peaks for HA crystal and no impurity phases were detected………………………………..56

Figure 4.3 SEM image of (a) polished non-cracked HA surface and (b) cracked HA surface and CLSM Z-stack maximum reflection intensity projections of (c) polished non-cracked HA surface and (d) cracked HA surface. On the cracked HA surface, Vickers indentation impression is the center diamond shape. Accompanying radial cracks and lateral crack spalling are pointed out by white and black arrows, respectively………………………………………………57

Figure 4.4 CLSM fluorescence images of OBs attached to non-cracked HA specimens at (a) 1 hour, (b) 2 hours and (c) 4 hours, and cracked HA specimens at (d) 1 hour, (e) 2 hours and (f) 4 hours. White arrows show positions of Vickers indentations and cracks. The OBs were stained with

Rhodamine Phalloidin (Actin) and Hoescht 33342 (nucleus). The Rhodamine Phalloidin Actin fluorescence stain was excited at 543 nm and emission was detected through a BA560-620 nm emission filter (represented in red). The Hoechst 33342 nucleus stain was excited with UV light at 405 nm and emission was detected through a BA430-470 emission filter (represented in blue)……………………………………………………………………………59

Figure 4.5 OB attachment is increased on cracked HA specimens at 4 hours. OBs were seeded at an initial density of 11,320 cells/cm^2. OB attachments on non-cracked and cracked HA specimens at 1, 2 and 4 hours are represented by the relative percentage of cells seeded. Error bars represent standard error. While no significant difference between OB attachment on non-cracked and cracked HA specimens were detected at 1 and 2 hours, significant increase of OB attachment by approximately 28% on cracked HA specimens was detected at 4 hours using Student's t-test (*$p<0.05$). Three specimens were used for each condition and the experiments were tripled……………………………….59

Figure 4.6 Illustration of angle θ between cell elongation direction (cyan line) and line connecting cell nucleus and indentation center (yellow line) on micrographs of cracked HA. The indentation impression and radial crack pattern are illustrated by white lines. The black crosses mark examples of cells showing no apparent elongation direction. The OBs were stained with Rhodamine Phalloidin (Actin) and Hoescht 33342 (nucleus). The Rhodamine Phalloidin Actin fluorescence stain was excited at 543 nm and emission was detected through a BA560-620 nm emission filter (represented in red). The Hoechst 33342 nucleus stain was excited with UV light at 405 nm and emission was detected through a BA430-470 emission filter (represented in blue)……………………………………………………………………………61

Figure 4.7 A schematic of cells with different elongation directions with respect to the indentation site. Cells with $\theta<45°$ are considered as aligned cells, while cells with $\theta \geq 45°$ are considered as non-aligned cells………………………… 63

Figure 4.8 Probability density histograms of θ for a) non-cracked HA (N=489) and b) cracked HA (N=587) fit to uniform distribution as shown by the thick solid black line. N is the total number of cells considered in the probability density histograms. The goodness of fit was tested using the Kolmogorov-Smirnov method. The θ distribution for non-cracked HA fitted to uniform distribution ($p>0.05$). The θ distribution for cracked HA did not fit to the uniform distribution ($p<0.05$)……………………………………………………64

Figure 4.9 The relative fractions of aligned cells ($\theta<45°$) and non-aligned cells ($\theta \geq 45°$ and circular cells) on a) non-cracked HA and b) cracked HA at 4 hours. Significantly more non-aligned cells than aligned cells were detected from non-cracked HA micrographs, while the opposite was observed from cracked HA micrographs. The significance of difference was detected using Student’s t-test ($p<0.05$)……………………………………………………………………65

Figure 4.10 The micrograph was partitioned into a central circle of 15 µm in radius and 15 µm wide outer rings (a). The number of OBs with aligned tendency ($\theta<45°$) in the center circle and outer rings (15 µm wide) were counted and normalized by the area respectively (b). Most cells with aligned tendency ($\theta<45°$) were found in the annulus 75 to 90 µm from the indentation center (b), which is around the tip of the radial cracks from Vickers indentation (a)……………………………………………………………………………………66

Figure 4.11 OB growth is not affected by the presence of cracks on HA specimens. OBs were seeded at an initial density of 11,320 cells/cm^2. OB growths on non-cracked and cracked HA specimens at 1, 3 and 5 days are represented by the relative percentage of cells seeded. Error bars represent standard errors. No significant differences between OB growths on non-cracked and cracked HA specimens were detected ($*p<0.05$). Three specimens were used for each condition and the experiments were tripled…67

Figure 4.12 OB maturation characterized by (a) AP expression and (b) AP activity was enhanced on cracked HA specimens. OBs were seeded at initial density of 20,000 cells/cm^2. After 21 days of cell culturing, AP gene expression was examined using RNA extracted from cell layers. Gene expression was normalized to levels of an unmodified housekeeping gene, HPRT. AP activity was assessed on cell layers and then measured by spectrophotometer. Significant increases in both (a) AP gene expression and (b) AP activity were detected using Student’s t-test ($*p<0.05$). Error bars represent standard errors. Three specimens were used for each condition and the experiments were tripled…………………………………………………………………………..68

Figure 4.13 (a) Runx2, (b) Col-I and (c) OC expressions on non-cracked and cracked HA at 21 days. All gene expression was examined using RNA extracted from cell layers. Gene expression was normalized to levels of an unmodified housekeeping gene, HPRT. Significant increase in Runx2 expression on cracked HA specimens was detected using Student’s t-test ($*p \leq 0.05$). No significant differences in Col-I and OC expressions between non-cracked and cracked HA specimens were detected. Error bars represent standard errors. Three specimens were used for each condition and the experiments were tripled……………………………………………………..69

Figure 4.14 CLSM Z-stack maximum fluorescence intensity projections of OB mineral depositions on (a) non-cracked and (b) cracked HA at 21 days. The OBs were pulsed with Xylenol Orange every other day during culturing since day four. The Xylenol Orange fluorescence stain was excited at 543 nm and emission was detected through a BA560-620 emission filter (represented in orange)……………………………………………………………………………70

Figure 5.1 ESEM images of the same indentation impression on HA surface (a) before immersing in distilled water, (b) 4 hours after immersion in distilled water, and (c) 24 hours after immersion in distilled water……………………...97

Figure 5.2 The plot of calcium concentration released from non-cracked (○) and cracked (□) HA specimens as a function of time. Error bars represent standard deviations. The non-cracked HA calcium release data were fit to equation (1), which yielded a coefficient of determination $R^2 = 0.977$. The cracked HA calcium release data were fit to equation (2), which yielded a coefficient of determination $R^2 = 0.986$………………………………………..99

Figure 6.1 CLSM Z-stack maximum fluorescence intensity projections of calcium depositions on (a) non-cracked and (b) cracked HA in the absence of cell culture. The OBs were pulsed with Xylenol Orange every other day during culturing since day four. The Xylenol Orange fluorescence stain was excited at 543 nm and emission was detected through a BA560-620 emission filter (represented in orange)……………………………………………………….108

Figure 7.1 Schematic of the measurement of osteoblast location with respect to the indentation region on a cracked HA micrograph. The cell location is characterized by the radial distance from indentation center, r and angle α..114

Figure 7.2 Schematic of the measurement of osteoblast location with respect to the indentation region on a non-cracked HA micrograph. The cell location is characterized by the radial distance from indentation center, r and angle α..115

Figure 7.3 The radial distance, r distributions (left column) and the angle, α distributions (right column) after 1 (first row), 2 (second row) and 4 hours (third row) of attachment on non-cracked HA. The r distributions were fit to Rayleigh distribution (mauve solid line), and the α distributions were fit to Uniform distribution (black solid line) using EasyFit. The radial distance r distributions did not fit to Rayleigh distribution at all hours ($p<0.01$), while the angle α distributions were uniform at all hours………………………………………117

Figure 7.4 The radial distance, r distributions (left column) and the angle, α distributions (right column) after 1 (first row), 2 (second row) and 4 hours (third row) of attachment on cracked HA. The r distributions were fit to Rayleigh distribution (mauve solid line), and the α distributions were fit to Uniform distribution (black solid line) using EasyFit. The radial distance r distributions did not fit to Rayleigh distribution at all hours ($p<0.01$), while the angle α distributions were uniform all hours……………………………………………..118

Figure 8.1 SEM images of (a) a thermally etched surface of a 94.3% dense HA specimen, where the average grain size calculated using line intercept method (a total of 210 intercepts) was 7.9 µm and (b) a polished surface of a 95.4% dense HA specimen, where uniformly distributed spherical or quasi spherical pores with a few interconnected or entrapped pores were observed. The diameters of the surface-breaking pores are less than 3 µm………………...128

Figure 8.2 (a) The average initial radial crack length as a function of Vickers indentation loads. The error bars represent the standard deviations. The collected data were fit to equation (8). The coefficient of determination R^2 is 0.997. (b) The average initial lateral crack length as a function of Vickers indentation loads. The error bars represent the standard deviations. The collected data were fit to equation (9). The coefficient of determination R^2 is 0.998……………………………………………………………………………132

Figure 8.3 The average radial crack length as a function of time, normalized with respect to the initial radial crack length at each load. The normalized values were then plotted versus time with a common unit value at time zero. The error bars represent the standard deviation. The collected data were fit to equation (11). The coefficient of determination R^2 for the 0.98 N, 1.96 N, 2.94 N, and 4.91 N loads were 0.934, 0.931, 0.987, and 0.992, respectively……134

Figure 8.4 The time constant τ obtained from the least-square fit of equation (11) to the average radial crack length versus time data for the 0.98 N, 1.96 N, 2.94 N, and 4.91 N loads. The error bars represent the standard deviation from each curve fitting………………………………………………………………….136

Figure 8.5 A schematic of the fully developed indentation crack system, where c^R is the half radial crack length and c^L is the lateral crack size....................137

Figure 8.6 The relative frequency of lateral cracks observed intersecting with free surface from 15 indentations at each of the five Vickers indentation loads (0.98 N, 1.96 N, 2.94 N, 4.91 N, and 9.81 N)….……………………………138

Figure 8.7 The average ratio of initial lateral crack length (c_0^L) over half initial radial crack length (c_0^R) (●), and the average ratio of saturated lateral crack length (c_S^L) over half saturated radial crack length (c_S^R) (■) as a function of Vickers indentation loads. The error bars represent the standard deviations……………………………………………………………………...139

Figure B-1 Schematic of atomic absorption spectrophotometer structure….164

Figure C-1 The logarithm of volume change increases linearly with the logarithm of time. The data were fit to equation (3). The coefficient of determination R^2 = 0.98………………………………………………………….169

CHAPTER 1

INTRODUCTION

The vertebrate skeletal system experiences cyclic forces that are tensile, compressive and/or shear in nature during daily activities such as walking, running and jumping, which could lead to the formation and accumulation of microcracks in bone [Hazenberg et al. 2009]. Bone with tolerable minor damage can be repaired and renewed through the remodeling process *in vivo* which involves both bone resorption by osteoclasts (OCs) and bone formation by osteoblasts (OBs) [Hadjidakis and Androulakis 2006]. Since bone densification was linked to the presence of microcracks in racing horses and/or greyhounds [Burr et al. 1985, Muir et al. 1999], we have hypothesized that microcracks lead to enhanced OB cell maturation. Understanding how microcracking affects OB cells could provide insight into fracture healing mechanism(s) as well as change the design parameters for the development of orthopedic scaffolds that promote faster bone healing.

Hydroxyapatite (HA or $Ca_{10}(PO_4)_6(OH)_2$) comprises two-thirds of the inorganic component of physiological bone and is therefore an ideal substrate material to assess the effect of microcracks on bone healing by examining OB maturation [Park and Lakes 2007]. In this study, a 7X7 grid of microcracks were introduced onto an HA substrate using Vickers indentation. At set time intervals [Shu et al. 2003], OB attachment, proliferation and maturation were evaluated using the appropriate assays along with CLSM (confocal laser scanning microscopy) characterization. The response of OBs to microcracks was investigated by comparing cell behavior (attachment, alignment, spatial distribution, proliferation and maturation) on microcracked and non-microcracked HA specimens.

Further, the calcium ions released from both non-cracked and cracked HA surfaces were examined using atomic absorption spectroscopy (AAS) based on the work of Duchyne et al. [1993], who found that changes in calcium concentration in the microenvironment led to changes in OB response. In order to determine if the presence of microcracks affects calcium ion release (HA surface dissolution), non-cracked and cracked HA specimens were immersed in distilled water at 37ºC for different time intervals. The calcium ion concentrations in distilled water from both groups were measured using AAS.

Another focus of my research is to understand the behavior of cracks introduced into the HA scaffold using Vickers indentation. HA is brittle in nature and environmental crack growth has been observed by different researchers [Benaqqa et al. 2003 and 2004, Barinov et al. 2005].

The slow growth of radial cracks introduced by Vickers indentations in HA in ambient air was conducted for two purposes. First, slow crack growth was examined to understand the general slow crack growth phenomenon in HA, since HA has been widely used in various fields as will be discussed in Chapter 2, to predict crack propagation in bone, as the propagation of cracks has been shown to lead to catastrophic bone fracture [Fratzl 2008]. This study examines the slow growth of radial cracks induced by Vickers indentation in dense HA (94% of theoretical density) during aging in ambient air as a function of time. We found that there is a load dependence of the radial crack growth and this is linked to the partitioning of the residual strain energy by the lateral crack growth.

REFERENCES

REFERENCES

[Barinov et al. 2005] Barinov SM, Fadeeva IV, Fateeva LV, and Tumanov SV. Delayed fatigue of hydroxy- and fluoro- hydroxyapatite ceramics in simulated body fluid. Key Eng Mater 2005; 290: 366-369.

[Benaqqa et al. 2005] Benaqqa C, Chevalier J, Saadaoui M, and Fantozzi G. Investigation crack growth process in dense hydroxyapatite using the double torsion method. Fract Mech Ceram 2005;14: 387-397.

[Burr et al. 1985] Burr DB, Martin RB, Schaffler MB, and Radin EL. Bone remodeling in response to fatigue microdamage. J Biomech, 1985;18: 189-200.

[Ducheyne et al. 1993] Ducheyne P, Radin S, and King L. The effect of calcium phosphate ceramic composition and structure on *in vitro* behavior. I. Dissolusion. J Biomed Mater Res 1993; 27: 25-34.

[Fratzl 2008] Fratzl P. When the cracks begin to show. Nat Mater 2008; 7: 610-612.

[Hadjidakis and Androulakis 2006] Hadjidakis DJ and Androulakis II. Bone remodeling. Ann NY Acad Sci 2006;1092: 385-396.

[Hazenberg et al. 2009] Hazenberg JG, Hentunen TA, Heino TJ, Kurata K, Lee TC, and Taylor D. Microdamage detection and repair in bone: Fracture mechanics, histology, cell biology. Technol Health Care 2009; 17: 67-75.

[Muir et al. 1999] Muir P, Johnson KA, and Ruaux-Mason CP. *In vivo* matrix microdamage in a naturally occurring canine fatigue fracture. Bone 1999; 25: 571-576.

[Park and Lakes 2007] Park JB and Lakes RS. (2007). Biomaterials: An Introduction. Madison: Springer.

[Shu et al. 2003] Shu R, McMullen R, Baumann MJ, and McCabe LR. Hydroxyapatite accelerates differentiation and suppress growth of MC3T3-E1 osteoblasts. J Biomed Mater Res A 2003; 67: 1196-1204.

CHAPTER 2

BACKGROUND

THE COMPOSITION AND STRUCTURE OF BONE

Bone is the major calcified tissue in vertebrates and provides mechanical support to muscle attachment as well as protection for vulnerable internal organs. Bone is considered as a composite material consisting of approximately 33.3% organic and 66.7% inorganic components as shown in Table 2.1 [Gray 2008]. The exact proportion of each component in bone may vary as a function of bone type, and for the same bone type, the composition can vary with age, gender, species. The organic matrix provides traction and torsion tolerance and the inorganic mineral providing rigidity and compressive strength [Park and Lakes 2007].

Table 2.1 Chemical compositions of bone measured by Berzelius [Gray 2008]

	Chemical Composition	Relative Proportion of Bone Constituents (%)
Organic Matter	Gelatine and Blood-vessels	33.30
Inorganic	Phosphate of Lime	51.04
	Carbonate of Lime	11.30
	Fluoride of Calcium	2.00
	Phosphate of Magnesia	1.16
	Soda and Chloride of Sodium	1.20
Total		100.00

The main component of the organic matrix is type I collagen, which provides a backbone for bone mineral crystal deposition. When the collagen molecules change due to genetic abnormality, such as for the case of brittle bone disease, the bone mineral crystals become smaller and may deposit outside the collagen fibrils [Vetter et al. 1991, Traub et al. 1994]. While collagen provides the basis for bone mineralization, collagen itself does not initiate or facilitate bone mineralization [Mergenhagen et al. 1960]. Instead of collagen, non-collagenous proteins regulates the bone matrix mineralization [Termine et al. 1981, Endo and Glimcher 1989].

The mineral component of bone shows chemical similarity with the mineral hydroxyapatite (HA or $Ca_{10}(PO_4)_6(OH)_2$). The Ca:P ratio in HA is 1.67:1, but in the analysis of bone mineral, this ratio varies from 1.3:1 to 1.9:1 [Gokhale et al. 2001]. The mineral component of bone results from bone mineralization, which is a process involving crystal nucleation and growth that is regulated by matrix proteins. The crystal nuclei form through homogeneous and /or heterogeneous nucleation. In homogeneous nucleation, ions in the solution collide until reaching a critical size where they form a stable critical nucleus. The crystal then grows as ions are added to the nucleus. At higher ion concentrations, the accumulation of ions and/or ion clusters may favor more nucleation. However, homogeneous nucleation is rare, requiring a much higher energy when compared to heterogeneous nucleation. Heterogeneous nucleation occurs on already present foreign surface where the non-collagenous matrix proteins serve as nucleators and lead to discrete mineral deposition along the collagen fibers [Gower 2011]. After the initial crystal formation, the crystals may grow through agglomeration and lengthening [Mitchell et al. 2001, Falini et al. 2001].

The structure of bone, when examined at the microscopic scale, has two forms: woven and lamellar. Woven bone is composed of disoriented collagen fibers and has isotropic mechanical properties. In contrast, lamellar bone has oriented collagen fibers which result in anisotropic mechanical properties. Depending on the structural organization of the woven and lamellar bone, two bone morphologies can form: cortical (dense and/or compact) and trabecular (spongy and/or cancellous) (Figure 2.1).

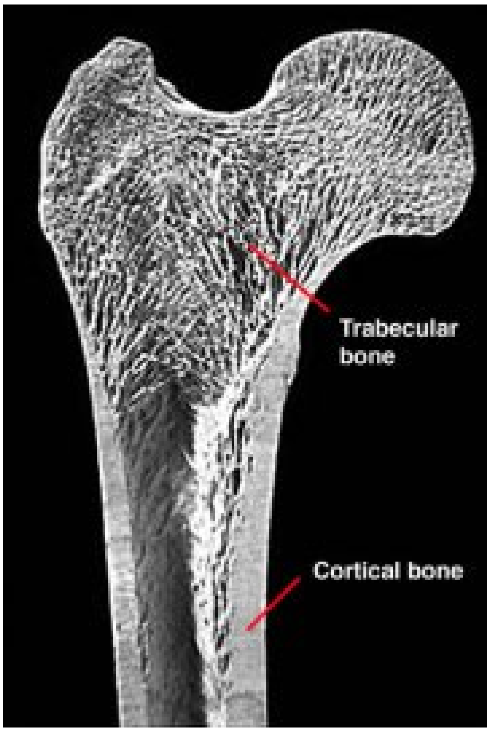

Figure 2.1 Longitude femur section showing trabecular and cortical bone. Photo taken by Paul Crompton [2011] at University of Wales College of Medicine. For interpretation of the references to color in this and all other figures, the reader is referred to the electronic version of this dissertation.

Load bearing is the major function of bone in the body, mechanical properties are thus of great importance in characterizing bone. The mechanical properties of bones, such as modulus of elasticity, toughness, tensile strength, and failure strain vary with shape, mineral content, humidity of the environment, and mechanical testing techniques, etc. [Park and Lakes 2007]. A comparison between the Young's modulus (GPa) and tensile strength (MPa) of physiological bone and several commonly used bone implant materials (longitude testing direction) is shown in Table 2.2 [Park and Lakes 2007, Carew et al. 2004].

Table 2.2 Comparison of the mechanical properties of long bone and common biomaterials used for bone replacement [Park and Lakes 2007, Carew et al. 2004]

Materials	Tensile Strength (MPa)	Young's Modulus (GPa)
Femur (Long Bone)	121	17.2
Al_2O_3	1000 to 10,000	350
Co-Cr Alloy [a]	735	225
316 S.S. [b]	600 (1000) [c]	210
PMMA	35 to 50	3.0
Polyethylene	23 to 40	0.6 to 1.8

a 28% Cr, 2% Ni, 7% Mo, 0.3% C (max), Co balance.
b Stainless steel, 18% Cr, 14% Ni, 2 to 4% Mo, 0.03 C (max), Fe balance.
c Values in parentheses are for the cold-worked state.

MICROCRACKING IN BONE

Bone microdamage occurs in the form of microcracks in humans

[Blickenstaff 1966, Schaffler et al. 1995, Lee et al. 2000], thoroughbred racing horses [Stepnik et al. 2004, Da Costa Gomez et al. 2004] and greyhounds [Johnson et al. 2001, Muir et al. 1999] following repetitive physical activity. For example, while the strain levels in human bone during walking reach $\varepsilon = 3 \times 10^{-4}$ to 8×10^{-4}, and during running reach $\varepsilon = 8 \times 10^{-4}$ to 1.2×10^{-3}, this is less than the threshold failure strain in a single cycle. However, the repetitive nature of these activities leads to an accumulation of microdamage [Lanyon et al. 1975, Burr et al. 1996]. Unless such activity ceases or declines dramatically, this microdamage can coalesce into macrocracks, leading to catastrophic fracture [Blickenstaff 1966, Schaffler et al. 1989 and 1990].

The connection between bone microcracks and repetitive physical activity was first postulated by Frost [1960], who used Fuchsin staining to detect their presence. More recently, microcracks have been identified in bone using increasingly sophisticated techniques including optical and confocal laser scanning microscopy (CLSM) using Fuchsin haematoxylin [Schaffler et al. 1995, Lee et al. 2000, Da Costa Gomez et al. 2004, Muir et al. 1999] and eosin [Johnson et al. 2001] and fluorescent staining [Zioupos and Currey 1994], scanning electron microscopy (SEM) [Stepnik et al. 2004] and radiography [Blickenstaff 1966].

In most cases, if the physical activity that causes damage is reduced, catastrophic failure can be prevented because bone has the ability to dynamically remodel following the onset of microdamage. Osteoclasts (OCs) are specialized bone cells that resorb bone, while osteoblasts (OBs) generate new bone in the vicinity of the microcracks [Burr 2002]. OC and OB activities are increased when the syncytium, adjacent to areas of bone microdamage, signals for remodeling to begin through increased osteocyte apoptosis. The details of bone remodeling and the function of osteoblast will be reviewed in the following section. This coupling between remodeling and microcracking may paradoxically result in a lower incidence of initial catastrophic fracture because of the ability of the microcracks to dissipate energy through crack formation, which in turn signals bone healing.

Besides bone, microcracking in HA and other brittle materials is also commonly observed during the release of residual stresses [Withers and Bhadshia 2001, Marshall et al. 1983], which can be introduced into the ceramic body during fabrication, handling, and use due to mismatch in material properties, such as elasticity, plasticity, and thermal expansion coefficient [Withers and Bhadshia 2001 and 2002]. The details of residual stress and microcracking will be discussed in a later section. On one hand, the existence of microcracks can deteriorate mechanical properties such as the Young’s modulus and the fracture strength [Case 2002]; on the other hand, microcracks can enhance the fracture toughness of brittle ceramics by redistributing the stress or releasing the residual stress at the major crack tip [Shum and Hutchinson 1990], thus preventing catastrophic fracture.

BONE REMODELING AND OSTEOBLAST FUNCTION

Bone continues to grow from its inception until skeletal maturity. It responds to stresses, healing following fatigue and/or fracture through a dynamic process called bone remodeling that occurs throughout our lifetime [Hadjidakis and Androulakis 2006]. During bone remodeling, osteoclasts remove bone at the bone surface and osteoblasts form new bone matrix in the cavities left from the bone resorption. Bone mineralization begins with calcium and phosphate precipitation following by crystallization, forming the hydroxyapatite phase [Hadjidakis and Androulakis 2006]. Osteoblasts play an important role in bone mineralization by promoting apatite crystal formation and growth on the extracellular matrix (ECM) [Hessel et al. 2002]. Thus the understanding of osteoblast function is essential for successful bone tissue engineering.

Mature osteoblasts are highly secretory cells, and the secretory products include mainly type I collagen and other non-collagenous proteins such as bone sialoprotein, osteocalcin, and osteopotin [Marks and Odgren 2002]. It is hypothesized that osteoblast facilitate mineralization by producing matrix vesicles, which provides microenvironment for hydroxyapatite crystallization [Boskey 1998].

The interaction of osteoblasts with the substrate surface includes attachment/adhesion, proliferation, and finally maturation phases [Anselme 2000]. Adhesion, being the first phase of cell/substrate interaction, plays an important role in determining the subsequent proliferation and differentiation stages. The adhesion of osteoblasts involves various kinds of biological proteins, such as extracellular matrix (ECM) proteins, membrane proteins and cytoskeleton proteins [Anselme 2000, Goldstein 2006].

Before interacting with the substrate surface, osteoblasts will first secrete ECM proteins, which then adsorb to the substrate surface. After that, proteins on the cell membrane then combine with the adsorbed ECM proteins, thereby realizing the linkage to the substrate surface [Hiortso and Roos 1994]. Among all of the ECM proteins, collagen, fibronectin, vitronectin, and laminin are known to be the proteins that influence anchorage-cell adhesions [Cristenson et al. 2007]. The integrin family on the OB cell membrane is in charge of cell/substrate adhesion [Anselme 2000, Goldstein 2006]. These integrins combine with ECM proteins which contain the specific arginine-glycine-aspartic (RGD) peptide sequence adsorbed on the substrate surface [Grzesik and Robey 1994, Balasundaram et al. 2006].

Osteoblasts could also migrate on the substrate surface from dynamic interactions with surrounding cells and the substrate. This involves the formation and fixation of lamellipodium on their leading edge, generation of energy required for movement and finally, the release of adherence at the rear [Anselme 2000]. After adhesion, osteoblasts proliferate through mitosis and secrete ECM matrix for later mineralization, which occurs in the last phase of differentiation.

The differentiation of mature osteoblasts *in vitro* is a multi-stage process, which is characterized by different phenotypes. The interaction between biomaterials and osteoblasts can thus be assessed by examining the characteristic phenotypical gene expressions, such as Runx2, collagen I (COL I), alkaline phosphatase (AP), osteocalcin (OC), etc. [Aubin 2001]. Runx2 is the transcription factor that regulates the differentiation of pluripotent mesenchymal progenitor cells into osteoblast lineage. COL I, alkaline phosphatase and osteocalcin are three characteristic genes that regulate the development of osteoblast matrix secretion, differentiation and mineralization [Aubin 2001].

BIOMATEIRAL SURFACE PROPERTIES AFFECTING OSTEOBLASTS

The effect of a biomaterial on osteoblast response is largely dependent upon the surface characteristics of the substrate. Rather than being a passive anchorage support for osteoblasts, the substrate surface can interact with the cells as reflected by differential cell adhesion, alignment, proliferation, and maturation on different biomaterial surfaces [Grinnell 1978]. The surface characteristics of a substrate material include surface chemistry, surface topography, surface roughness, surface area, surface hydrophobicity, and/or hydrophilicity, as well as the surface energy.

The surface chemistry primarily depends on the chemical composition of the surface and may significantly differ from the bulk chemistry. By modifying the surface chemical composition, the cell/substrate interaction could be influenced [Romand et al. 1995, Alves et al. 2008, Hench and Ethridge 1982]. For example, using self-assembling methods, several model studies, in which the surfaces of materials were chemically modeled, showed that terminal amine and carboxylic acid groups could improve adhesion while surfaces with polyethylene glycol subunits inhibited cell adhesion [Tegoulia and Cooper 2000].

The surface topography of materials has been shown to restrict sites of cell adhesion and dictate cell orientation [Wiemann et al. 2007]. A century-old study found that the substrate topography of spider webs dictated the orientation of adherent cells [Harrison 1912]. In a study carried out Martin Wiemann et al. [2007] revealed that osteoblast orientation was influenced on the micro scale, showing that osteoblast-like cells could be contact-guided by parallel grooves. Other studies found that grooves of ~0.5 microns deep and 4~20 microns wide were ideal for cell alignment [Ismail et al. 2007].

The hydrophobicity of a material surface can be characterized by the contact angle (θ) of a water drop on the surface (Figure 2.2) [Hench and Ethridge 1982]. Generally speaking, water drop has a higher contact angle on a hydrophobic surface, and a smaller angle on a hydrophilic surface. Studies on 13 different kinds of polymers demonstrated significantly larger cell spreading on hydrophilic surfaces compared with hydrophobic surfaces [Schakenraad et al. 1986]. Polar chemical functional groups (hydrophilic) were found to improve cell adhesion while non-polar ones (hydrophobic) hinder cell adhesion [Tegoulia and Cooper 2000, Scotchford et al. 1998]. MacDonald et al. [2004] applied thermal and chemical methods to modify the surface properties of a Ti-6Al-4V alloy in a way that the hydrophobicity of the alloy surfaces was artificially altered by changing the surface area and roughness. Surfaces with a larger surface area and roughness were found to be more hydrophilic. Both a significant increase in fibronectin and MG63 cell attachment were observed on more hydrophilic surfaces [MacDonald et al. 2004].

Surface bonds (external surfaces and grain boundaries) are different from the bulk in that the atomic bonds at surfaces are unsaturated [Park and Lakes 2007, Hench and Ethridge 1982]. From a thermodynamic point of view, the unsaturated surface atoms are at a higher free energy (G) [Hench and Ethridge 1982]. When two different phases are in contact, they tend to minimize their interfacial energy which corresponds to a minimum free energy of the system [Hillert 2008]. In the case of a free surface (or external surface), the free energy could be calculated from the contact angle (θ) of a specific liquid drop on the surface (Figure 2.2).

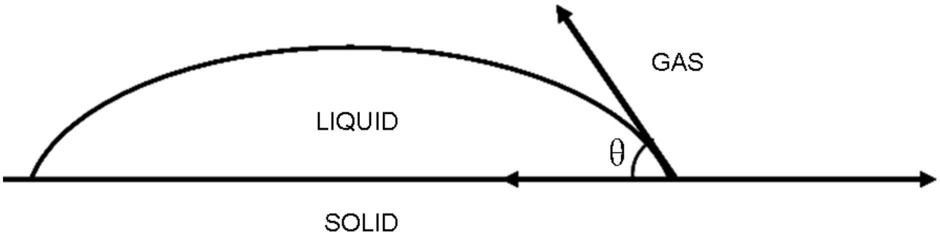

Figure 2.2 Illustration of the surface contact angle of water drop on an ideal solid surface surrounded by gas [Hench and Ethridge 1982].

The contact angle is defined by analyzing the force on a liquid drop when it was placed on a solid surface and surrounded by gas as shown in equation 1 (apply to ideal surface) [Hench and Ethridge 1982]. The three phases, solid (s), liquid (l), and gas (g) are immiscible.

$$\gamma_{SL} = \gamma_{SL} + \gamma_{LG} \cos\theta \tag{1}$$

where γ_{SG} is the interfacial tension between solid and gas phases; γ_{SL} is the interfacial tension between solid and liquid phase; γ_{LG} is the interfacial tension between liquid and gas phases; θ is the contact angle shown in Figure 2.2. The increase in cell adhesion corresponds to an increase in surface area and surface energy [He et al. 2004, Webster and Ejiofor 2004, Webster et al. 1999].

HYDROXYAPATITE APPLICATIONS

The presence of HA in natural teeth and bone makes it a good candidate biomaterial for hard tissue substitution [Park and Lakes 2007]. The HA surface can adsorb functional biomolecules, and the change of surface electronic state due to biomolecule adsorption enables HA thin films to be used as biosensors [Masanobu et al. 2005]. HA coatings on metal implants promote earlier and stronger bonding between the host bone and the implant, as well as increase uniform bone growth at the bone-implant interface [Furlong and Osborn 1991, Geesink et al. 1988]. Porous ceramic implants based on HA have also been designed for space filling osteogenesis [Dong et al. 2001, Damien et al. 2003]. Dense HA, fabricated using spark plasma sintering, showed an improvement in the bone-like apatite crystal growth [Nakahira et al. 2002]. Fang et al. [1995] fabricated transparent HA, using microwave sintering, for use as observation windows for percutaneous devices used by Aoki et al. [1987].

The use of HA as a catalyst support has also been extensively explored. Mori et al. [2003] created a novel heterogeneous Lewis acid catalyst for Diels-Alder and Aldol reactions utilizing HA for the hybrid-catalyst, which presented high activity for useful carbon-carbon bond forming reactions as well as high reusability. Mori et al. [2004] in a later study, created an HA supported palladium nano-cluster for selective alcohol oxidation using molecular oxygen, which could effectively promote alcohol oxidation under atmospheric oxygen pressures. Venugopal and Scurrell [2003] used HA as a support for gold catalyst which was exceedingly active for water gas shift reaction at low temperatures.

Nagai and Nishino [1988] proposed the use of porous HA for a CO_2 sensor based on the changes in electrical conductivity induced in HA by CO_2. One year later, Owada et al. [1989] found that the logarithm of the electrical conductivity of their yttrium substituted calcium HA sensor decreased linearly, as the relative humidity increased from 30% to 65%, suggesting the application of HA as a humidity sensor. Measurements of the dielectric and current-voltage properties of an HA thin film in the frequency range from 1 KHz to 1MHz showed HA may be used as an insulating material for electronic circuits and as dielectric layers in microwave applications for biomedical devices [Hontsu et al. 1997].

HA has also been employed in the removal of heavy metals from the environment. Raicevic et al. [2004] demonstrated theoretically and experimentally that heavy metals in polluted soils could be immobilized by addition of HA to soils. HA organofunctionalized with silylating agents $(H_3CO)_3SiR$ also showed the ability to remove heavy cations from aqueous solution [Silva et al. 2006].

RESIDUAL STRESS AND MICROCRACKING

Residual stress can be introduced from the mismatch of material properties such as elasticity, plasticity, and thermal expansion coefficient within a system of interest [Bhadeshia 2002]. Residual stress can be classified into Type I (macroscopic), Type II (microscopic) and Type III (atomic scale) stresses according to the dimension it exhibits at equilibrium with the surroundings [Withers and Bhadshia 2001]. Common examples of Type I stresses are those that arise from a misfit of components in an assembly, different thermal stresses experienced by different parts, and non-uniform plastic deformation in machining processes such as grinding [Withers and Bhadshia 2001, Hoshide et al. 2001]. Common examples of microscopic residual stresses are the stresses that exist between different phases within a composite and/or resulting from phase transformation [Lawn et al. 1993]. Residual stresses that arise from point defects and/or dislocations are generally balances at atomic scales [Withers and Bhadshia 2001].

As residual stresses can develop easily and have an important influence on a materials performances and lifetime, the nature, distribution and role of residual stress in initiating and driving crack growth in brittle materials has been extensively studied in different systems.

Fu and Evans [1981] investigated the influence of grain size on the formation of secondary cracks in the vicinity of a primary crack in single phase polycrystals by calculating residual stress introduced by thermal expansion anisotropy. By considering a microstructure configuration that renders the maximum compressive stress along the primary crack opening direction as well as the maximum opening tensile stress at the secondary crack initiation sites, Fu and Evans [1981] calculated the critical grain size (l_c) for the initiation of secondary cracks, and found that the increase in fracture toughness between l_c and l_{cs} (critical grain size for spontaneous cracking) corresponded with experimental fracture energy of Al_2O_3, Nb_2O_5 and TiO_2 as a function of grain size.

When examining toughness for two-phase ceramics, Lawn et al. [1993] considered the insertion of compressed second-phase particles in the matrix and divided the bridging stress into two regions according to the crack opening scale within the matrix. They found a transitional crack length that corresponded to a minimum toughness and a mechanism change of how the second phase particles affected matrix microcracking. Below that transitional crack length, compressed second-phase particles provide tensile stress to the surrounding matrix for the initiation of cracks, while above the transitional crack length, the second-phase particles act as frictional barriers for grain sliding [Lawn et al. 1993]. The model proposed by Lawn et al. [1993] was well supported by the data from Al_2O_3/Al_2TiO_5 composite.

Cao et al. [1988] examined the nature and distribution of residual stresses in systems consisting of two brittle ceramics bonded with a ductile metallic strip during cooling. They found that the maximum residual tensile stresses at the ceramic/metal interface. The residual tensile stresses were determined by the elastic mismatch resulted from differential thermal expansion coefficient ($\alpha_{metal} > \alpha_{ceramic}$) during cooling process. The elastic mismatch gave rises of cracking when considering an elastic field. The exact cracking or fracture resistance sites at the ceramic/metal interface, or within the brittle ceramic, varies with the thermal mismatch between the metal and the ceramic, the yield strength and the thickness of the metal layer. The prediction of cracking nonetheless relied on the interpretation of the intensity and distribution of the residual stress [Cao et al. 1988].

This demonstrates the importance of analyzing residual stress in determining microcracking in brittle materials, since materials tend to release residual stresses to get to a lower energy state. Microcracking is what accompanies residual stress release observed in brittle materials [Withers 2001 and Marshall 1982].

Available techniques that provide quantitative or qualitative information about residual stress were divided into destructive and non-destructive tests

[James and Lu 1996]. Destructive methods are mostly mechanical approaches such as hole drilling, ring core, layer removal, and sectioning, where a change in stresses between the new stress state and the old residual stress state was calculated [James and Lu 1996]. Non-destructive methods such as X-ray diffraction and neutron diffraction generally are based on the influence of residual stress on the materials' physical properties [James and Lu 1996].

Vickers indentation can itself be an approach to investigate residual stresses that are introduced through grinding and machining damage [Hoshide et al. 2001, Marshall et al. 1982]. Raman luminescence microscopy was used by Banini et al. [2001] in evaluating the residual component under Vickers indentation impression and their direct measurement of residual stress field was shown in accordance with predictions from theoretical analytical models.

VICKERS MICRO-INDENTATION

Vickers micro-indentation of brittle solids provides useful information for evaluating machining damage [Marshall et al. 1982] and grinding [Hoshide et al. 2001] as well as estimating residual stress [Jang 2009]. It is thus necessary to understand the nature and distribution of stresses in the vicinity of Vickers indentation and the cracking systems involved in the indentation process in order to use the Vickers indentation technique in our studies.

Vickers indentation with an included angle of 136° could be described by an elastic/plastic deformation mode [Chiang et al. 1982]. In a comprehensive review on indentation fracture by Lawn and Wilshaw [1975], the simplified model of stress field about Vickers indentations is illustrated in Figure 2.3. The material in contact with the indenter was assumed to form a hydrostatic core which pushed the surrounding material and resulted in the formation of a plastic zone, both of which were assumed to exhibit a spherical symmetry, and beyond the plastic zone, an elastic matrix [Lawn and Wilshaw 1975]. According to this model, a residual stress field could be developed from the formation of permanent deformation zone during the loading process without recovering after unloading [Lawn and Wilshaw 1975].

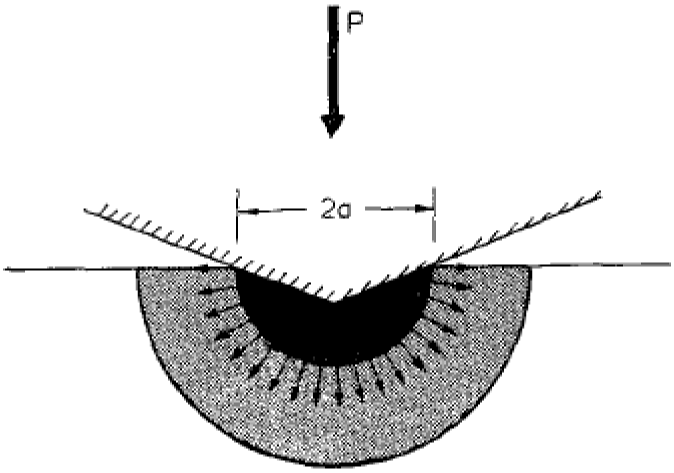

Figure 2.3 Elastic/plastic indention model of spherical symmetry with a “hydrostatic core” near contact region with indenter, “plastic deformation zone” around the “hydrostatic core”, and “elastic matrix” [Lawn and Wilshaw 1975].

Lawn et al. [1980] divided the stress field into a reversible elastic component and an irreversible residual component illustrated in Figure 2.4. Marshall and Lawn [1979] provided a more detailed explanation of the combination of symmetric tensile stress field and asymmetric compressive stress field in the formation of elastic component during loading. Chiang et al. [1981] described the plastic zone volume ΔV using maximum load P and the indentation volume V.

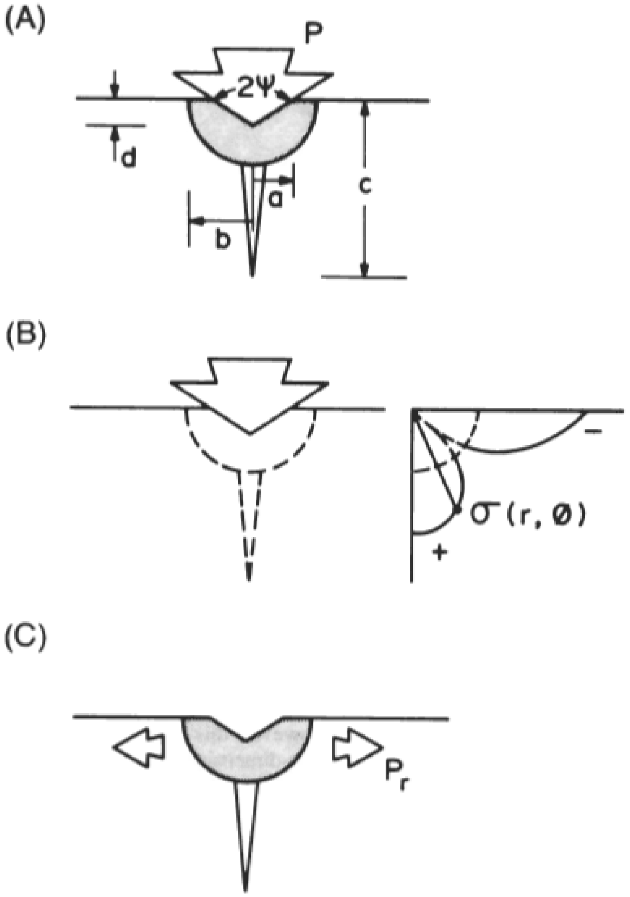

Figure 2.4 (A) Elastic/plastic combination at maximum load P which is a summation of (B) reversible elastic component at load P and (C) irreversible residual component after unloading [Lawn 1980].

Stress analysis of both the elastic and plastic zone could provide useful information for the formation and evolution of cracks during the loading and unloading cycles of Vickers indentation [Chiang et al. 1981]. By analyzing the stress field at the boundary between the plastic deformation zone and the elastic matrix, Chiang et al. [1981] concluded that the initiation of cracks close to the boundary was due to a maximized tension, a diminishing of tension in the elastic matrix, and the compressive nature of the residual plastic deformation zone.

During a complete cycle of loading and unloading in Vickers indentation, median, radial, and lateral cracks may form as illustrated in Figure 2.5 [Chiang et al. 1981].

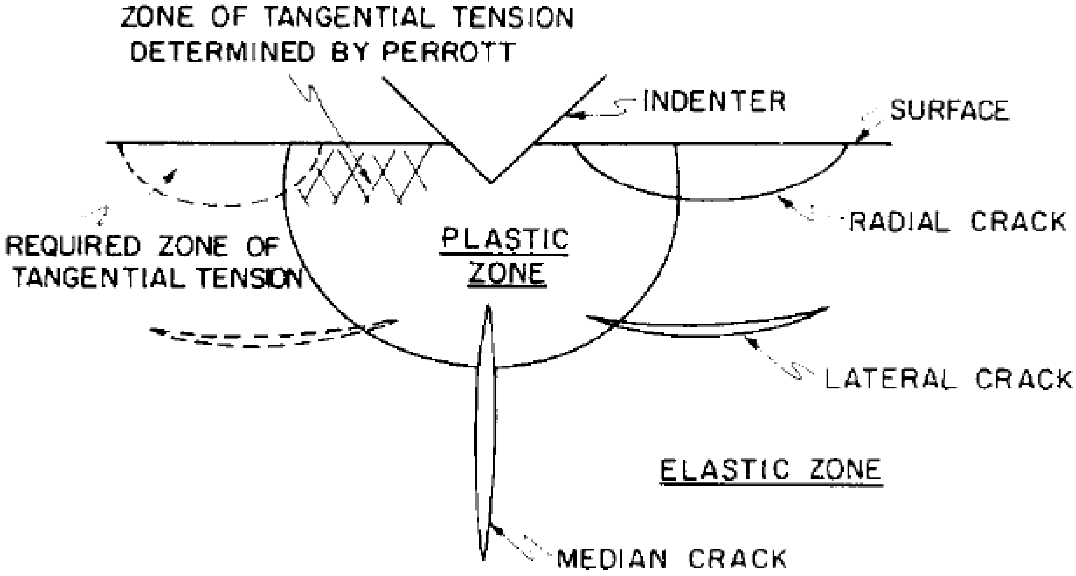

Figure 2.5 Elastic/plastic sharp contact indentation generates median, radial and lateral cracks [Chiang et al. 1981].

Lawn et al. [1980] and Marshall et al. [1982] examined propagation of both median/radial and lateral crack systems by analyzing the role of the elastic and the residual components of the stress field during indentation. The two crack systems were classified according to their orientations with respect to the loading plane, where the median/radial cracks were found to lay within the loading plane while the lateral cracks in planes parallel to the surface [Lawn et al. 1980].

As depicted by Figure 2.5, cracking occurs mostly within the elastic field outside the plastic deformation zone, and the intensity of the elastic field was maximized at maximum loading P and recovered during the removal of the indenter [Chiang et al. 1981, Lawn et al. 1980]. The irreversible residual plastic deformation zone was created during loading and stayed below the indentation impression after unloading as a compressed semi-sphere within the elastic matrix. Thus, during loading the propagation of the median crack was enhanced by the downward tensile stress and the propagation of the radial crack was prevented by the asymmetric compressive stress within the elastic field (Figure 2.4B). Upon unloading, the residual plastic zone remained to influence the crack evolution, particularly to drive the radial crack growth [Lawn et al. 1980].

Both the elastic and residual components were incorporated in the calculation of fracture toughness, denoted by K_c, during loading and unloading, and compared with experimental observations by Lawn et al. [1980]. They concluded that the residual plastic deformation zone played a dominant role in determining the final crack configuration, which was characterized by an equilibrium crack length upon unloading in an inert ambient environment especially at a lower H/E (hardness to Young's modulus) ratio. The relationship between equilibrium radial crack length c^R and maximum indentation load P is described by equation 2,

$$c^R = \{\S_r^R (\cot\psi)^{2/3}[(E/H)^{1/2}/K_C]\}^{2/3} P^{2/3} \tag{2}$$

where $\S_r^R$ is a constant, ψ is the half angle for Vickers indentation, and E, H, K_C are Youngs' modulus, hardness, and fracture toughness, respectively. E, H, and K_C can be considered invariant for a system at equilibrium with its surroundings [Lawn et al. 1980].

Analysis on the evolution of a lateral crack system based on the summation stress field of an elastic component and a residual component (illustrated by Figure 2.6) also showed that the residual plastic deformation zone provided the driving force for lateral crack propagation. This is similar to the case of radial crack propagation except that the relationship between the lateral crack length c^L and the maximum indentation load P was described by equation 3 [Marshall et al. 1982]. Observations from experimental measurements in various ceramics showed that lateral cracks mostly resided at the plastic deformation zone radius [Marshall 1982]. Similar to radial crack propagation, the dominant role of residual component was also magnified at lower H/E ratio [Marshall et al. 1982].

$$c^L = \{(\zeta_L / A^{1/2})(\cot\psi)^{5/6}[(E/H)^{3/4} / K_C H^{1/4}]\}^{1/2} P^{5/8} \quad (3)$$

where ζ_L and A are constants [Marshall et al. 1982].

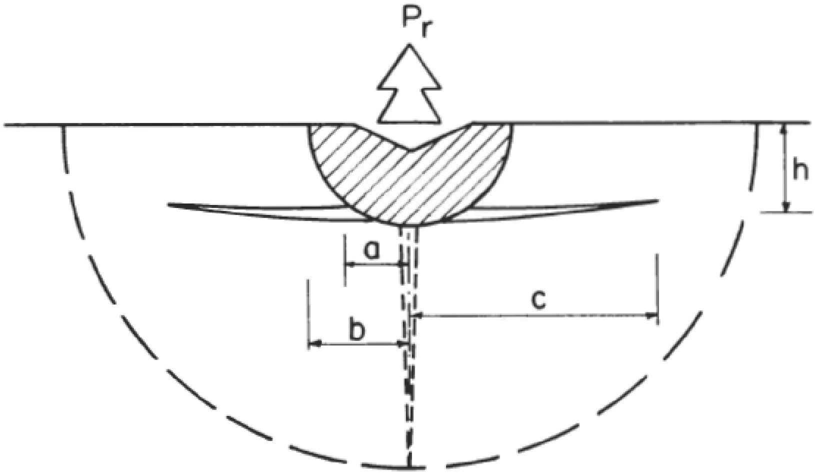

Figure 2.6 Residual component of stress field below indentation which remains upon unloading and lateral crack of distance h below the free surface. The dashed lines depict the median/radial crack system [Marshall et al. 1982].

The fact that both radial and lateral cracks evolve upon unloading as discussed above [Lawn et al. 1980, Marshall et al. 1982] indicates that the energy stored in the residual plastic deformation zone has two outlets, which may add complexity in interpreting the slow growth of radial cracks based on the relaxation of residual stresses. It is necessary to measure the residual stresses in the compressive deformation zone and/or at the tensile crack tip arises in order to understand the slow growth behavior of indentation-induced radial cracks in hydroxyapatite. The methods for measuring this residual stress were discussed in the previous section.

For most ceramics and/or glasses, a general trend of diminishing strength with time was observed in ambient air, the molecular mechanism of which was investigated by Michalske et al. [1983] considered a chemical concerted reaction driven by the strain energy at the crack tip. However, the environment effect on slow crack growth in HA is not addressed in the current study.

REFERENCES

REFERENCES

[Alves et al. 2008] Alves CM, Yang Y, Marton D, Carnes DL, Ong JL, and Sylvia VL et al. Plasma surface modification of poly (D, L-Lactic acid) as a tool to enhance protein adsorption and the attachment of different cell types. J Biomed Mater Res Part B 2008; 87B: 59-66.

[Anselme 2000] Anselme K. Osteoblast adhesion on biomaterials, Biomaterials 2000; 21: 667-681.

[Aoki et al. 1987] Aoki H, Akao M, Shin Y, Tsuzi T, and Togawa T. Sintered hydroxyapatite for a percutaneous device and its clinical application. MED PROG TECHNOL 1987; 12: 213-220.

[Aubin 2001] Aubin JE. Regulation of osteoblast formation and function. Rev Endocr and Metab Disorders 2001; 2: 81-94.

[Balasundaram et al. 2006] Balasundaram G, Sato M, and Webster TJ. Using hydroxyapatite nanoparticles and decreased crystallinity to promote osteoblast adhesion similar to functionalizing with RGD. Biomaterials 2006; 27: 2798-2805.

[Banini et al. 2001] Banini GK, Chaudhri MM, Smith R, and Hayward IP. Measurement of residual stresses around Vickers indentations in a ruby crystal using a Raman luminescence microscope. J Physic D: Appl Physic 2001; 34: L122-L124.

[Bhadeshia 2002] Bhadeshia HKDH. Residual Stress: Material Factors. Totten G, Howes M, and Inoue T, editors. Handbook of Residual Stress and Deformation of Steel. Materials Park, Ohio: ASM International; 2002: 3-10.

[Blickenstaff 1966] Blickenstaff LD. Fatigue fracture of the femoral neck. J Bone Joint Surg 1966; 48A: 1031-1047.

[Boskey 1998] Boskey AL. Biomineralization: conflicts, challenges, and opportunities. J Cell Biochem 1998; Suppl 30-31: 83-91.

[Burr 2002] Burr DB. Targeted and nontargeted remodeling. Bone 2002; 30: 2-4.

[Burr et al. 1996] Burr DB, Milgrom C, Fyhrie DP, Forwood M, Nyska M, and Finestone A et al. *In vivo* measurement of human tibial strains during vigorous activity. Bone 1996; 18: 405-410.

[Cao et al. 1988] Cao HC, Thouless MD, and Evans AG. Residual stresses and cracking in brittle solids bonded with a thin ductile layer. Acta Metall 1988; 36: 2037-2046.

[Carew et al. 2004] Carew EO, Lemons JE, Ranter BD, Vesely I, and Volger E. Biomaterials Science: An Introduction to Materials in Medicine. 2nd ed. Ratner BD et al. Eds. 2004: Elsevier Academic Press.

[Case 2002] Case ED. The saturation of thermomechanical fatigue in brittle materials. Alibadi MH, editors. Thermo-Mechanical Fatigue and Fracture. Southampton, UK: WIT Press; 2002: 137-208.

[Chiang et al. 1982] Chiang SS, Marshall DB, and Evans AG. The response of solids to elastic/plastic indentation. I. Stresses and residual stresses. J Appl Physic 1982; 53: 298-311.

[Christenson et al. 2007] Christenson EM, Anseth KS, van den Beucken JJ, Chan CK, Ercan B, and Jansen JA et al. Nanobiomaterial applications in orthopedics. J Orthop Res 2007; 25:11-22.

[Christenson et al. 2007] Christenson EM, Anseth KS, van den Beucken JJP, Chan CK, Ercan B, and Jansen JA et al. Nanobiomaterial applications in orthopedics. J Orthop Res 2007; 25: 11-22.

[Crompton 2011] Crompton P. Facts about bones – bone: a living dynamic tissue. International osteoporosis foundation 2011.

[Da Costa Gomez et al. 2004] Da Costa Gomez TM, Radtke CL, Kalscheur VL, Swain CA, Scollay MC, Edwards RB et al. Effect of focused and radial extracorporeal shock wave therapy on equine bone microdamage. Vet Surg 2004; 33: 49-55.

[Damien et al. 2003] Damien E, Hing K, Saeed S, and Revell PA. A preliminary study on the enhancement of the osteointegration of a novel synthetic hydroxyapatite scaffold *in vivo*. J Biomed Mater Res 2003; 66: 241-246.

[Dong et al. 2001] Dong J, Kojima H, Uemura T, Kikuchi M, Tateishi T, and Tanaka J. *In vivo* evaluation of a novel porous hydroxyapatite to sustain osteogenesis of transplanted bone marrow-derived osteoblastic cells. J Biomed Mater Res 2001; 57: 208-216.

[Endo and Glimcher 1989] Endo A and Glimcher MJ. The effect of complexing phosphoproteins to decalcified collagen on *in vitro* calcification. Connect Tissue Res 1989; 21: 179-90.

[Falini et al. 2001] Falini G, Fermani S, and Ripamonti A. Oriented crystallization of octacalcium phosphate into beta-chitin scaffold. J Inorg Biochem 2001; 84: 255-258.

[Fang et al. 1995] Fang Y, Agrawal DY, Roy DM, and Roy R. Fabrication of transparent hydroxyapatite ceramics by ambient-pressure sintering. Mater Lett 1995; 23: 147-151.

[Frost 1960] Frost HL. Presence of microscopic cracks *in vivo* in bone. Henry Ford Hospital Medical Bulletin 1960; 8: 27-35.

[Fu and Evans 1981] Fu Y and Evans AG. Microcrack Zone Formation in Single Phase Polycrystals. Acta Metall 1981; 30: 1619-1625.

[Furlong and Osborn 1991] Furlong RJ and Osborn JF. Fixation of hip prostheses by hydroxyapatite ceramic coatings. J Bone Joint Surg 1991; 73B: 741-745.

[Geesink et al. 1988] Geesink RGT, de Groot K, and Klein CP., Bonding of bone to apatite-coated implants. J Bone Joint Surg 1988; 70B: 17-22.

[Gokhale et al. 2001] Gokhale J, Robey PG, and Boskey AL. Osteoporosis. in The Biochemistry of Bone, 2nd ed. Marcus R, Feldman D, Kelsey J, Eds. 2001 San Diego: Academic Press.

[Goldstein 2006] Goldstein AS. Tissue Engineering and Artificial Organs. 3rd ed. Bronzino JD, editors. Electrical engineering handbook series; 2006.

[Gower 2011] Gower LB. Mineralization of dense collagen scaffolds using a polymer-induced liquide-precursor (PILP) process. Composites at Lake Louise, 2011.

[Gray 2008] Gray H. (2008). The classic 1860 edition: Gray’s Anatomy. London: Arcturus.

[Grinell 1978] Grinell F. Cellular adhesiveness and extracellular substrata. Int rev Cytol 1978; 53: 65-144.

[Grzesik and Robey 1994] Grzesik WJ and Robey PG. Bone-Matrix Rgd Glycoproteins - Immunolocalization and Interaction with Human Primary Osteoblastic Bone-Cells in-Vitro. J Bone Miner Res 1994; 9: 487-496.

[Hadjidakis and Androulakis 2006] Hadjidakis DJ and Androulakis II. Bone remodeling. Annal New York Acad Sci 2006; 1092: 385-396.

[Harrison 1912] Harrison RG. The cultivation of tissues in extraneous media as a method of morphogenetic study. Anatom Record 1912; 6: 181-193.

[He et al. 2004] He HW, Li GD, Li B, and Chen ZQ. Effects of surface microstructure of hydroxyapatite on protein adsorption and biological performance of osteoblasts. Appl Surf Sci 2008; 255: 565-567.

[Hench and Ethridge 1982] Hench LL and Ethridge EC. (1982) Biomaterials: An Interfacial Approach. Biophysics and Bioengineering Vol 4. New York: Academic Press, Inc.

[Hessel et al. 2002] Hessle L, Johnson KA, Anderson HC, Narisawa S, Sali A, and Goding JW et al. Tissue-nonspecific alkaline phosphatase and plasma cell membrane glycoprotein-1 are central antagonistic regulators of bone mineralization. Proceed National Acad Sci 2002; 99: 9445-9449.

[Hillert 2008] Hillert M. Phase Equilibria, Phase Diagrams and Phase Transformations-their Thermodynamic Basis. 2nd ed. 2008: Cambridge.

[Hjortso and Roos 1994] Hjortso MA and Roos JW. (1994). Cell Adhesion: Fundamentals and Biotechnological Applications. Marcel Dekker, Inc.

[Hontsu et al. 1997] Hontsu S, Matsumoto T, Ishii J, Nakamori M, Tabata H, and Kawai T. Electrical properties of hydroxyapatite thin films grown by pulsed laser deposition. Thin Solid Films 1997; 295: 214-217.

[Hoshide and Abe 2001] Hoshide T and Abe J. Grinding-Induced Residual Stress Estimation by Indentation-Fracture Method in Ground Silicon Nitrides. J Mater Eng Perform 2001; 10: 586-591.

[Ismail et al. 2007] Ismail FSM, rohanizadeh R, Atwa S, Mason RS, Ruys AJ, Martin PJ et al. The influence of surface chemistry and topography on the contact guidance of MG63 ostoeblast cells. J Mater Sci – Mater Med 2007; 18: 705-714.

[James and Lu 1996] James MR and Lu J. Introduction. Lu J, editors. Handbook of Measurement of Residual Stresses. Society for Experimental Mechanics; 1996: 1-4.

[Jang 2009] Jang J. Estimation of residual stress by instrumented indentation: A review. J Ceram Process Res 2009; 10: 391-400.

[Johnson et al. 2001] Johnson KA, Skinner GA, and Muir P. Site-specific adaptive remodeling of greyhound metacarpal cortical bone subjected to asymmetrical cyclic loading. Am J Veter Res 2001; 62: 787-793.

[Lanyon et al. 1975] Lanyon LE, Hampson WGJ, Goodship AE, and Shah JS. Bone deformation recorded in vivo from strain gauges attached to the human tibia shaft. Acta Orthop Scand 1975; 46: 256-268.

[Lawn and Wilshaw 1975] Lawn B and Wilshaw R. Indentation Fracture: Principles and Applications. J Mater Sci 1975; 10: 1049-1081.

[Lawn et al. 1980] Lawn BR, Evans AG and Marshall DB. Elastic/Plastic Indentation Damage in Ceramics: The Median/Radial Crack System. J Am Ceram Soc 1980; 63: 574-581.

[Lawn et al. 1993] Lawn BR, Padture NP, Braun LM, and Bennison SJ. Model for Toughness Curves in Two-Phase Ceramics: I, Basic Fracture Mechanics, J Am Ceram Soc 1993; 76: 2235-2240.

[Lee et al. 2000] Lee TC, O’Brien FJ, and Taylor D. The nature of fatigue damage in bone. Int J Fatigue 2000; 22: 847-853.

[MacDonald et al. 2004] MacDonald DE, Rapuano BE, Deo N, Stranick M, Somasundaran P, and Boskey AL. Thermal and chemical modification of titanium-aluminum-vanadium implant materials: effects on surface properties, glycoprotein adsorption, and MG63 cell attachment. Biomaterials 2004; 25: 3135-3146.

[Marks and Odgren 2002] Marks SC and Odgren RP. Structure and development of the skeleton. Bilezikian JP, Raisz LG and Rodan GA, editors. Principles of bone biology. New York: Academic Press; 2002: 3-15.

[Marshall and Lawn1979] D. B. Marshall, B. R. Lawn. Residual stress effects in sharp contact cracking, Part I Indentation fracture mechanics. J Mater Sci 1979; 14: 2001-2012.

[Marshall et al. 1982] Marshall DB, Lawn BR, and Evans AG. Elastic/Plastic Indentation Damage in Ceramics: The Lateral Crack System. J Am Ceram Soc 1982; 65: 561-566.

[Marshall et al. 1983] Marshall DB, Evans AG, Khuri Yakub BT, Tien JW and Kino GS. The nature of machining damage in brittle materials. Proc Royal Soc London A 1983; 385: 461-475.

[Masanobu et al. 2005] Masanobu K, Masami K, Hiroaki N, Koichi M, Takashi H, Shigeki H et al. Protein adsorption on patterned hydroxyapaptite thin films fabricated by pulsed laser deposition Japan J Appl Physics 2005; 44: L326-L327.

[Mergenhagen et al. 1960] Mergenhagen SE, Martin GR, Rizzo AA, Wright DN, and Scott DB. Calcification *in vivo* of implanted collagens. Biochim Biophys Acta 1960; 43: 563-565.

[Michalske and Freiman 1983] Michalske TA and Freiman SW. A Molecular Mechanism for Stress Corrosion in Vitreous Silica. J Am Ceram Soc-Green 1983; 66: 284-288.

[Mitchell et al. 2001] Mitchell CA, Yu L, and Ward MD. Selective nucleation and discovery of organic polymorphs through epitaxy with single crystal substrates. J Am Chem Soc 2001; 123: 10830-10839.

[Mori et al. 2003] Mori K, Hara T, Mizugaki T, Ebitani K, and Kaneda K. Hdroxyapatite-Bound Cationic Ruthenium Complexes as Novel Heterogeneous Lewis Acid Catalysts for Diels-Alder and Aldol Reactions. J Am Chem Soc 2003; 125: 11460-11461.

[Mori et al. 2004] Mori K, Hara T, Mizugaki T, Ebitani K, and Kaneda K. Hydroxyapatite-Supported Palladium Nanoclusters: A Highly Active Heterogeneous Catalyst for Selective Oxidation of Alcohols by Use of Molecular Oxygen. J Am Chem Soc 2004; 126: 10657-10666.

[Muir et al. 1999] Muir P, Johnson KA, and Ruaux-Mason CP. *In vivo* matrix microdamage in a naturally occurring canine fatigue fracture. Bone 1999; 25: 571-576.

[Nagai and Nishino1988] Nagai M and Nishino T. A new type of CO2 gas sensor comprising porous hydroxyapatite ceramics. Sensor Actuat 1988; 15: 145-151.

[Nakahira et al. 2002] Nakhira A, Tamai M, Aritani H, Nakamura S, and Yamashita K. Biocompatibility of dense hydroxyapatite prepared using an SPS process. J Biomed Mater Res 2002; 62: 550-557.

[Ong et al. 2008] Ong KL, Manley MT, and Kurtz SM. Have contemporary hip resurfacing designs reached maturity? A review. J Bone Joint Surg – Am Vol 2008; 90A: 81-88.

[Owada et al. 1989] Owada H, Yamashita K, Umegaki T, and Kanazawa T. Humidity-sensitivity of yttrium substituted apatite ceramics. Solid State Ionics 1989; 35: 401-404.

[Park and Lakes 2007] Park JB and Lakes RS. (2007). Biomaterials: An Introduction. Madison: Springer.

[Raicevic et al. 2005] Raicevic S, Kaludjerovic-Radoicic T, and Zouboulis AI. In situ stabilization of toxic metals in polluted solids using phosphates: theoretical prediction and experimental verification. J Hazardous Mater B 2005; 117: 41-53.

[Romand et al. 1995] Romand M, Gailard F, Charbonnier M, Prakash NS, Deshayes L, and Linossier I. Adhesion science and surface analysis, typlical examples. J Adhesion 1995; 55: 1-16.

[Schaffler et al. 1989] Schaffler MB, Radin EL, and Burr DB. Mechanical and morphological effects of strain rate on fatigue of compact bone. Bone 1989; 10: 207-214.

[Schaffler et al. 1990] Schaffler MB, Radin EL, and Burr DB. Long-term fatigue behavior of compact bone at low strain magnitude and rate. Bone 1990; 11: 321-326.

[Schaffler et al. 1995] Schaffler MB, Choi K, and Milgrom C. Aging and matrix microdamage accumulation in human compact bone. Bone 1995; 17: 521-525.

[Schakenraad et al. 1986] Schakenraad JM, Busscher HJ, Wildevuur CR, and Arends J. The influence of substratum surface free-energy on growth and spreading of human-fibroblasts in the presence and absence of serum-proteins. J Biomed Mater Res 1986; 20: 773-784.

[Scotchford et al. 1998] Scotchford CA, Cooper E, Leggett GJ, and Downes S. Growth of human osteoblast-like cells on alkanethiol on gold self-assembled monolayers: The effect of surface chemistry. J Biomed Mater Res 1998; 41: 431-442.

[Shum and Hutchinson 1990] Shum DKM and Hutchinson JW. On toughening by microcracks. Mech Mater 1990; 9: 83-91.

[Silva et al. 2006] Silva OG, Silva Filho EC, Gonseca MG, and Arakaki LNH et al. Hydroxyapatite organofunctionalized with silylating agents to heavy cation removal. J Colloid Interface Sci 2006; 302: 485-491.

[Stepnik et al. 2004] Stepnik MW, Radtke CL, Scollay MC, Oshel PE, Albrecht RM, Santschi EM et al. Scanning electron microscopic examination of third metacarpal/third metatarsal bone failure surfaces in thoroughbred racehorses with condylar fracture. Vet Surg 2004; 33: 2-10.

[Tegoulia and Cooper 2000] Tegoulia VA and Cooper SL. Leukocyte adhesion on model surfaces under flow: Effects of surface chemistry, protein adsorption, and shear rate. J Biomed Mater Res 2000; 50: 291-301.

[Termine et al. 1981] Termine JD, Kleinman HK, Whitson SW, Conn KM, McGarvey ML, and Martin GR. Osteonectin, a bone-specific protein linking mineral to collagen. Cell 1981; 26: 99-105.

[Traub et al. 1994] Traub W, Arad T, Vetter U, and Weiner S. Ultrastructural studies of bones from patients with osteogenesis imperfecta. Matrix Biol 1994; 14: 337-345.

[Venugopal and Scurrell 2003] Venugopal A and Scurrell MS. Hydroxyapatite as a novel support for gold and ruthenium catalysts: Behavior in the water gas shift reaction. Appl Catal A: Gen 2003; 245: 137-147.

[Vetter et al. 1991] Vetter U et al. Changes in apatite crystal size in bones of patiens with osteogenesis imperfecta. Calcif Tissue Int 1991; 49: 248-250.

[Webster and Ejiofor 2004] Webster TJ and Ejiofor JU. Increased osteoblast adhesion on nanophase metals: Ti, Ti_6Al_4V, and CoCrMo. Biomaterials 2004; 25: 4731-4739.

[Webster et al. 1999] Webster TJ, Siegel RW, and Bizios R. Osteoblast adhesion on nanophase ceramics. Biomaterials 1999; 20: 1221-1227.

[Wiemann et al. 2007] Wiemann M, Bingmann D, Franzka S, Hartman N, Urch H, and Epple M. Oriented growth of osteoblast-like cells on two dimensionally structured films of functionalized calcium phosphate nanoparticles on a silicon substrate. Adv Eng Mater 2007; 9: 1077-1081.

[Withers and Bhadshia 2001] Withers PJ and Bhadshia HKDH. Residual Stress Part 2-Nature and Origins. Mater Sci Tech 2001; 17: 366-375.

[Zioupos and Currey 1994] Zioupos P and Currey JD. The extent of microcracking and the morphology of microcracks in damaged bone. J Mater Sci 1994; 29: 978-986.

CHAPTER 3

CELL CULTURING PROTOCOLS

Basic cell culturing steps include: thawing, feeding, splitting, counting, and freezing. The MC3T3-E1 cell line used in this study was from the McCabe's lab on campus. In the current study, the cell passage number was 21~23 to guarantee consistent and comparable cell behavior between control and experimental groups. The passage number reflects the age of cells, in other words, the subculture time of the cells. With the increase in passage number, the cell population doubling time increases.

THAWING

The cells are stored in 1.8 ml cryogenic vials in liquid nitrogen, the boiling temperature of which is 77 K (-196℃ or -321° F) at atmospheric pressure. The handling of frozen cells thus requires the use of temperature resistant gloves to avoid frost damage to the skin.

The rule of thumb for cell preservation is fast thaw (< 5 minutes) and slow freeze. Leaving cells in cryogenic vials for long times leads to cell death. Cells can be thawed either by rubbing between warm hands or placing in a warm water bath. After thawing, the cells should be distributed evenly in 3-5 culture dishes with warm complete media (CM). The CM refers to α-MEM (alpha minimum essential media, Invitrogen, Carlsbad, CA) supplemented with 10% FBS (fetal bovine serum, Atlanta Biologicals, Lawrenceville, GA).

Depending on the passage number of the cells and the actual experimental design, the number of culture dishes for thawing may vary. The cell plates should be rocked slowly from side to side, and front to back, for an even distribution of cells across the plate and to avoid piling up at specific spots. The plates should not be rotated as the cells could be brought to the plate edges due to centrifuge force rather than distribute uniformly.

FEEDING

After thawing, cells are kept in an incubator (37℃, 5% CO_2 and 95% air) for 24 hours which allows the cells reattaching to plate surface. Feeding refers to the process of replacing the complete media. The old media in the culture dishes were aspirated away using a vacuum system. This step removes the dead cells that failed to reattach during the thawing step. The warmed-up complete media is then added to the culture dishes. After feeding, cells are moved back to the incubator. Depending on the experiment design, cells are fed every 1 to 3 days.

SPLITTING

Splitting refers to the step during which cells are removed from the substrate surface either for subculture or for specific studies. Usually, cells are fed with CM 24 hours prior to splitting. To determine when to split, cells should be checked on a daily basis. When about 25 cells are visible in the field of view using the 10x transmitted light microscope, the cells are ready for splitting. If the cells start to fill the field of view and appear to touch each other (confluency), the cells should not be used for studies, as subcloning may have already take place, which leads to changes in cell behavior [Bellows et al. 2004].

To split cells, the old media is first aspirated from the culture dishes the same way as in the feeding step. After removing the media, 0.5% Trypsin-EDTA (Trypsin-ethylenediaminetetraacetic acid, Invitrogen, Carlsbad, CA) is added to the plate, enough to cover the surface (e.g. 1 to 2 ml for 100 mm petri dish). This step detaches cells from the plate. For better results, the plates are rocked from side to side, as well as back and forth. However, this step should not last for more than 2 minutes as the Trypsin-EDTA could damage the cells. 1 to 2 ml of complete media is then added to the plates, and the plate surface is washed several times to gather most of the detached cells. The cell suspensions are then pipetted into 50 ml centrifuge tubes. The empty plate is brought to the transmitted light microscope to check if most of the cells are attached. The above steps are repeated if necessary. The total number of cells gathered in the suspension is counted using a hemacytometer. After counting, the cells could be subcultured with lower density in more plates, used for specific studies, or frozen for future use.

FREEZING

When there are excess cells left from studies, or when the desired passage number is reached, cells could be frozen for future use. The typical number of cells frozen in a 1.8 ml cryogenic vial is around 1 million. The preceding freezing steps are similar to splitting, which includes aspirating away the old media, trypsinizing, washing, and pipetting the cell suspension and followed by cell counting. After cell counting, the cells are centrifuged at 3000 rpm for 10 minutes. A white colored cell pallet should be visible after separating the cells from the media. After dumping the waste media from centrifuging, the cells should be re-suspended in the freezing media, the amount of which is dependent on the cell number. The freezing media is a mixture of 90% complete media and 10% DMSO (dimethyl sulfoxane, Sigma Aldrich), which is a cryoprotectant that protects cells from damage caused by low temperature. For each cryogenic vial, about 1.5 ml of freezing media is added.

In contrast to thawing, the most important thing to remember is to freeze slowly. The cryogenic vials are in a -80℃ freezer overnight and are then moved into the liquid nitrogen tank. If the same vial of cells will be used within 2 weeks, they can also be stored in the -80℃ freezer. However, for longer term storage, cells should be kept in the liquid nitrogen tank.

STERILE HANDLING

All the cell handling described above should be conducted in a sterilized environment to prevent possible contamination. Sterilization during cell culture mainly includes the following aspects: First, the biosafety cabinets should be maintained in a sterile condition at all time. The biosafety cabinets are where all cell handling takes place. The UV light inside the cabinets should always be on when not in use. Prior to use, the inner surface of the cabinets should be sprayed with 70% alcohol or isopropanol. The culture dishes, centrifuge tubes, cryogenic vials, and six-well plates should not be open outside of the cabinet hood. All the tools that will be used during cell culture should be sterilized either by autoclave (if applicable) and sprayed with 70% alcohol or isopropanol before entering the hood. Pipette tips should be autoclaved before using.

The incubator used for cell culturing should be cleaned and the removable parts autoclaved. The HEPA filter in the incubator is regularly replaced according to the HEPA replacement signal approximately every six months. The water bath in the incubator is filled with autoclaved distilled water. Supplements of aqua blue and a copper penny is added to help keeping out bacteria and/or yeast infections.

REFERENCES

REFERENCES

[Bellows et al. 2004] Bellows CG, Sodek J, Yao KL, Aubin JE. Phenotypic differences in subclones and long-term cultures of clonally derived rat bone cell lines.

CHAPTER 4

MICROCRACKS INDUCE OSTEOBLAST ALIGNMENT AND ACCELERATE MATURATION ON HYDROXYAPATITE SCAFFOLDS

ABSTRACT

The response of MC3T3-E1 mouse osteoblasts (OBs) to microcracks was investigated by comparing cell behavior on microcracked and non-microcracked hydroxyapatite (HA or $Ca_{10}(PO_4)_6(OH)_2$) specimens. Four hours after seeding, OB attachment was significantly greater on the microcracked HA specimens compared to non-cracked HA specimens ($p<0.05$). Confocal laser scanning microscope (CLSM) micrographs taken at this time demonstrated that the cells were randomly oriented on non-cracked HA specimens but preferentially aligned in the direction of the microcracks on the microcracked HA. OB proliferation was not influenced by the presence of microcracks. In contrast, OB maturation was enhanced on the microcracked HA, as shown by the significant increase ($p<0.05$) in alkaline phosphate (AP) activity and Runx2 and alkaline phosphatase gene expression at 21 days. CLSM images taken at 21 days indicate that mineral/bone deposition is concentrated at the indentation site on cracked HA specimens. Our findings suggest that microcracks induce OB recruitment, matrix synthesis and bone formation/healing at crack sites.

INTRODUCTION AND BACKGROUND

Fatigue fracture is common in greyhounds [Muir et al. 1999], horses [Estberg et al. 1996] and human athletes, especially runners [Brukner et al. 1996, Burr 1997] due to the repeated, cyclically applied stresses. In an in vivo study of racing greyhounds, Muir et al. [1999] found linear microcracks in the fatigue fracture of the central tarsal bone. Microcracking in bone is a common form of fatigue injury [Muir et al. 1999, Zarrinkalam et al. 2005, Taylor and Lee 1998, O'Brien et al. 2003, Hazenberg et al. 2009] where the tip-to-tip lengths of the resulting linear microcracks range from approximately 50 to 300 µm [Taylor and Lee 1998, Schaffler et al. 1989, Burr et al. 1990, Burr and Martin 1993, Mori and Burr 1993, Lee 1995, Lee et al. 1998].

From the mechanical standpoint, the formation of microcracks in the vicinity of the fatigue fracture [Muir et al. 1999, Zarrinkalam et al. 2005, Radtke et al. 2003, Burr et al. 1990] may prevent catastrophic bone failure by dissipating the strain energy at the advancing crack tip, thereby improving the overall bone toughness [An et al. 2011, Taylor and Prendergast 1995]. Microcracks also play an important physiological role in triggering bone healing and/or bone remodeling when the bone is adapting to an externally applied stress [Burr et al. 1985, Muir et al. 1999, Lee 1995, Martin and Burr 1989, Martin 1992, Mori and Burr 1993, Prendergast and Taylor 1994, Taylor 1997]. Although fatigue microcracks in bone have been shown to stimulate bone healing and/or remodeling, stress fractures occur if the microcracks accumulate at a rate faster than the rate of bone repair [O'Brien et al. 2003].

Bone remodeling is an interactive process between osteoclasts (OCs) and osteoblasts (OBs), where the former resorb existing bone and the latter form new bone [Hadjidakis and Androulakis 2006, Huiskes et al. 1987, Cowin and Hegedus 1976, Verborgt et al. 2000]. A desirable bone implant fosters faster bone formation and thus heals faster. This response is largely dependent on the interaction between the OBs and the implant substrate surface [Anselm 2000]. Enhanced in vivo bone remodeling in the vicinity of microcracks gives rise to our hypothesis that OBs prefer microcracks over intact, non-cracked HA scaffolds because the OB response to the microcracks mimics the natural fracture repair cascade events in physiologic bone.

HA, the main inorganic component of bone, is a widely used bone implant material [Smith et al. 2006a and 2006b, Shu et al. 2003, Hossain et al. 2005]. The interconnections among the microstructural-physical properties and the biological properties of HA and bone is a critical area of research. In terms of microstructural-physical properties, our group has examined the porosity dependence of a broad range of physical properties of HA [Hoepfner and Case 2002 and 2003, Ren et al. 2009, Fan et al. submitted Part I and Part II 2011, Singh et al. 2005 and 2006] along with microcracking and fracture in HA [Hoepfner and Case 2004, Fan et al. submitted 2011, Case et al. 2005]. In terms of the biological properties, the interactions between OBs and HA has also been investigated, including OB attachment, growth and differentiation

[Smith et al. 2006a and 2006b, Shu et al. 2003, Hossain et al. 2005] and gene expression [Xie et al. 2004].

Our collective understanding of HA and in particular, microcracking in HA, enables us to investigate the mechanism(s) by which OBs respond to microcracks in HA bone tissue engineering scaffolds. An improved understanding of the crack-cell interface, whether a function of the changes in the localized physical/chemical properties of the scaffold, could in turn lead to improved bio-functionality of the HA scaffolds and a greater insight into the mechanism(s) involved in fracture healing.

Early interactions of OBs with substrate surfaces include sequential attachment/adhesion, growth/proliferation and maturation/differentiation stages [Anselme 2000]. The attachment/adhesion of OBs, the first stage of cell/substrate interaction, is the initial step in determining the long-term viability and function of OBs. Rather than directly interacting with the naked substrate, cells secrete extracellular matrix (ECM) proteins that are adsorbed by the substrate surface. The cell attachment/adhesion phase is then achieved by the interaction of cell membrane proteins with the ECM proteins [Anselm 2000]. The ECM can alter cell shape and alignment through adhesive interactions with the cell cytoskeleton, which then in turn affects the arrangement of the ECM by exerting contracting forces [Numaguchi et al. 2003, Ingber and Folkman 1989, Singhvi et al. 1994, Huang et al. 1998, Parker et al. 2002]. Alterations in cell shape and alignment affect cell growth, motility, differentiation and apoptosis [Ingber 2002]. Thus, knowledge of these parameters is essential in evaluating cell/substrate interactions.

Cell alignment, cell shape and cell migration, guided by the substrate surface topography, were called contact guidance by Weiss [Weiss 1941]. Observations of cells guided by surface topography date back to 1912 when Harrison observed cell growth along the fibers of spider webs [Harrison 1912]. The surface topographies that have been shown to guide cells range in scale from the nano- (1 to 100 nm) to micro- (0.1 to 100 μm) scale [Curtis and Wilkinson 1998].

OB alignment is extensively studied by researchers because the anisotropic mechanical properties of bone are a function of the bone cell/collagen matrix alignment [Weiner et al. 1999, Ziv et al. 1996, Ascenzi and Benvenuti 1986]. Alignment of OBs and cell-produced collagen matrix was observed on anisotropic surface features, mostly parallel ridges and/or grooves introduced by electron beam/laser/Langmuir-Blodgett lithography at both the nano- and micro- scale [Lenhert et al. 2005, Zhu et al. 2005, Puckett et al. 2008, Yang et al. 2008]. In cases where grooves/ridges are introduced by abrasion [Calzado-Martin et al. 2011], both surface roughness and cracks have been shown to result [Couto et al. 1994]. However, for Vickers indentation, the cracking is controlled and localized, producing divots rather than ridges.

While parallel ridges and/or grooves have been shown to alter the entire substrate surface [Lenhert et al. 2005, Zhu et al. 2005, Puckett et al. 2008, Yang et al. 2008], Vickers indentation introduces a localized microcracked site (less than 100 µm in radius in this study. Vickers indentation cracks were thus introduced to HA substrate surfaces to test if OB alignment may prompt enhanced bone formation at and around the sites of localized microcracks in bone [Burr and Martin 1993, Mori and Burr 1993, Stafford et al. 1994].

In this chapter, OB attachment, alignment, growth and maturation were investigated on Vickers indentation microcracked HA to identify cellular responses to and benefits of introducing microcracks to biomimetic bone scaffolds.

MATERIALS AND METHODS

HA specimen preparation

Following established procedures, HA powders (Taihei, Osaka, Japan) with a particle size of 4-6 µm were uniaxially pressed at 28 MPa for one minute in a 32-mm diameter steel pellet die. The green HA specimens were then sintered in air at 1360°C for 4 hours. The sintered specimens were then polished to a 0.5 µm finish using diamond paste to obtain a flat, uniform surface. Microcracks were introduced to the polished surfaces using Vickers indentation with a Shimadzu micro-hardness tester at 4.9 N with a loading time of 5 seconds in ambient air at room temperature. Indents were introduced in a 7×7 grid with a 2 mm interval as shown schematically in Figure 4.1.

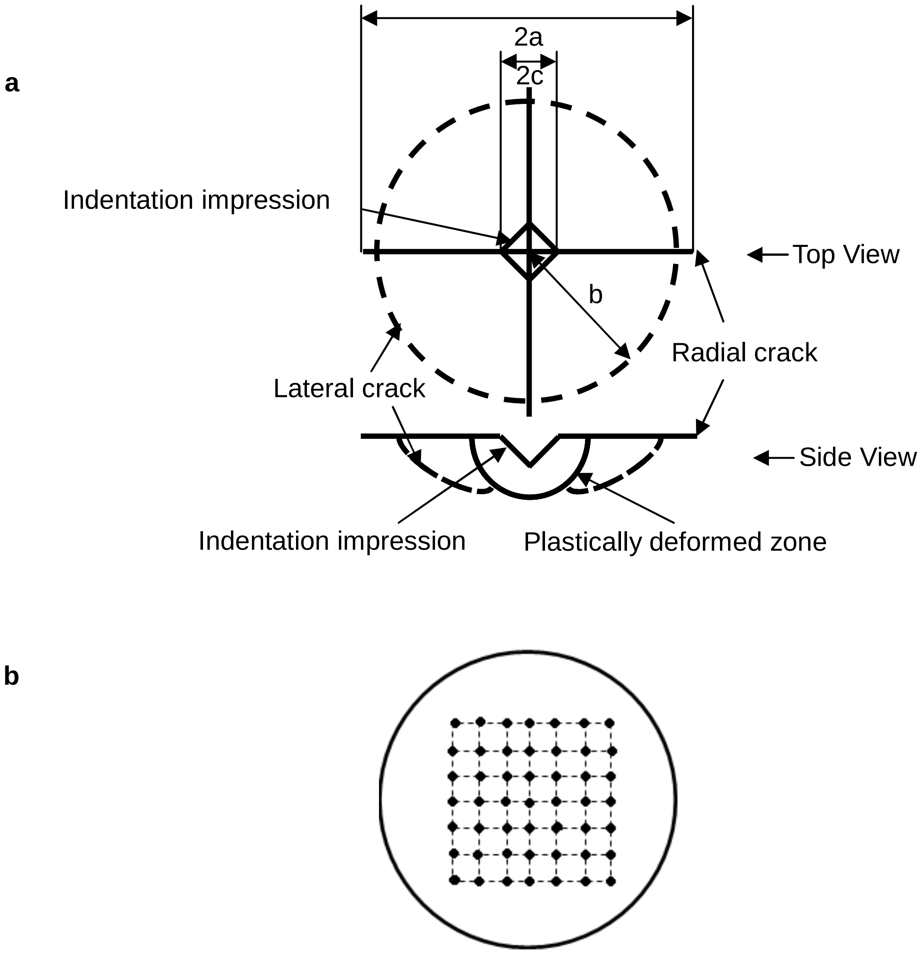

Figure 4.1 (a) Radial cracks introduced by Vickers indentation at 4.91 N; (b) A 7×7 grid with a 2 mm interval indentation pattern on HA specimens.

HA characterization

The phase purity of HA, both as-received powder and pulverized powder from sintered HA specimen was determined by X-ray diffraction (XRD) using Bruker D2 Phaser diffractometer equipped with Cu X-ray radiation operating at 30 kV, 10 mA and at sweep rates of 0.5° 2θ /min. The sample placed in a PMMA sample holder was rotated at 5°/min. The surface morphology of both cracked and non-cracked HA surfaces were imaged using scanning electron microscope (SEM) (JEOL-6400V SEM, JEOL Ltd., Japan) and confocal laser scanning microscope (CLSM) (Zeiss LSM 5 Pascal, Carl Zeiss, Inc., Thornwood, NY).

Cell culture

OB cells were seeded at a density of 11,320/cm^2 for the evaluation of cell attachment and growth. For cell maturation studies cells were seeded at a concentration of 20,000/cm^2. Cells were fed every other day with α-MEM media supplemented with 10% fetal bovine serum (FBS), 100 units Penicillin and 100 μg Streptomycin. The media was further supplemented with 2 mM inorganic phosphate and 2.5 μg/mL ascorbic acid to promote differentiation when cells reached confluence. Following lab protocols [Shu et al. 2003], cells were cultured in a humidified atmosphere containing 95% air and 5% CO_2 at 37 °C.

OB attachment and growth

For attachment and growth trials, three microcracked and three non-cracked HA specimens were used per time point. Cell attachment was evaluated at 1, 2 and 4 hours while cell growth was evaluated at 1, 3 and 5 days. Each experiment was repeated three times. In the cell attachment and growth studies, cells were fixed and stained with Hoechst 33342, and cell numbers counted using Cell Profiler. The relative fractions of attachment and growth were calculated by normalizing the cell density at each time period with the initial seeding density.

OB maturation

Cells were cultured on cracked and non-cracked HA discs for 21 days. Each experiment contained triplicate HA disks of each condition. To assess the level of maturation in the culture, staining was carried out to assess extracellular matrix and mineralization. AP staining was performed by incubating the OBs for 30 minutes at 37℃ with 0.5 mg/ ml naphthol AS-MX phosphate disodium salt with 1 mg/mL Fast Red TR salt in a 10.2 M Tris buffer, pH 8.4. AP quantization was performed by solubilizing the precipitated salt in 100% TCA, diluting 1:10, and reading at 540 nm as previously described [McCabe et al. 1996].

For molecular analyses of maturation and gene expression, RNA was isolated from OBs harvested from non-cracked and microcracked HA at 21 days, using Tri Reagent (Molecular Research Center, Inc., Cincinnati, OH). RNA integrity was assessed by formaldehyde-agarose gel electrophoresis. cDNA was synthesized by reverse transcription with Superscript II Reverse Transcriptase Kit and oligo $dT_{(12-18)}$ primers (Invitrogen, Carlsbad, CA) and amplified by real-time PCR with iQ SYBR Green Supermix (Biorad, Hercules, CA) and gene-specific primers synthesized by Integrated DNA Technologies (Coralville, IA). Hypoxanthine guanine phosphoribosyl transferase (HPRT) mRNA levels do not fluctuate between conditions and were used as an internal control. Other primers used are previously described [Botolin et al. 2006, Motyl et al. 2011].

CLSM imaging of OBs

OBs on cracked and non-cracked HA specimens were stained with Rhodamine Phalloidin actin stain and Hoechst nucleus stain at 1, 2 and 4 hours. The OB morphology and spatial distribution were imaged using CLSM (Olympus FluoView, Tokyo, Japan). In order to view the cell orientation in all directions with respect to the center of the microcracked region, the fluorescent micrographs of microcracked HA specimens were taken in a way such that the microcracked region was close to the center of the field of view. At four hours, a total of 30 micrographs were collected for both the control (non-cracked) and the experimental (cracked groups), with at least 500 cells analyzed per condition.

Xylenol Orange powder (Sigma-Aldrich Co., St. Louis, MO) was dissolved in distilled water to make a 20 mM stock solution which was added to differential media for detecting calcium formation [Wang et al. 2006]. Mineralization was assessed by pulsing the culture with 20 μM Xylenol Orange and then visualizing the disk using CLSM (Olympus FluoView, Tokyo, Japan).

STATISTICS

Student’s t-test was used to test the statistical significance of the differences where a value of $p < 0.05$ was considered significant.

RESULTS

HA characterization

The XRD analysis of as-received HA powder and pulverized sintered HA specimen showed that both HA powders were crystalline with characteristic peaks matching with the standard JCPDS 9-432 (Joint Committee on Powder Diffraction Standards, Swarthmore, PA). No phases other than HA were detected (Figure 4.2).

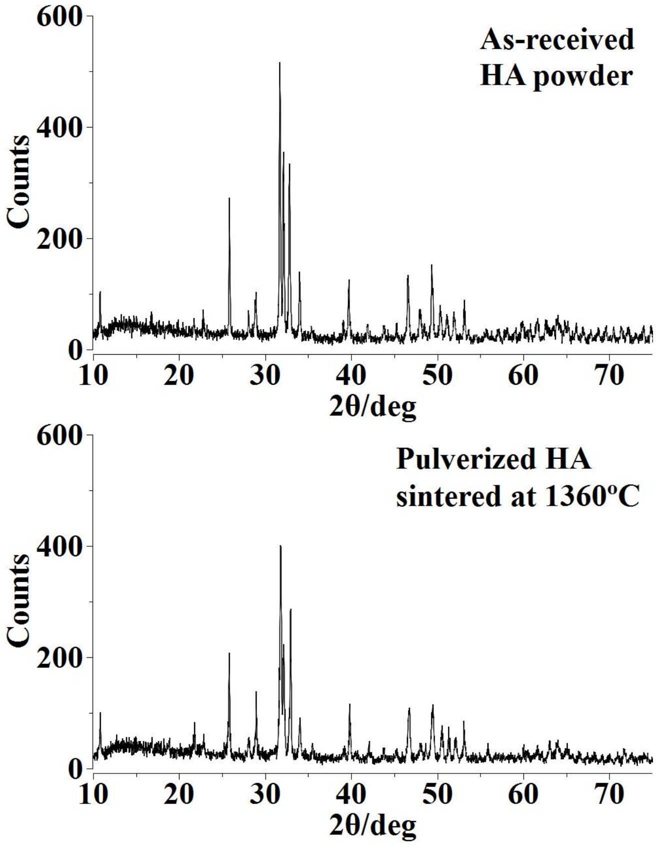

Figure 4.2 XRD spectra of as-received HA powder from vendor and pulverized sintered HA specimen. Both powders showed representative peaks for HA crystal and no impurity phases were detected.

Both the SEM and CLSM images of non-cracked HA showed a smooth surface with uniformly distributed, isolated, surface-breaking pores approximately 3 µm in diameter (Figure 4.3a and 4.3c). The SEM image of the cracked HA specimens clearly showed both the indentation impressions and chipping at the vicinity of the indentation impression (Figure 4.3b). The CLSM image of cracked HA showed clear radial cracks (2c ≈ 180µm) aligned parallel to the indentation diagonal as well as quarter plate like lateral cracks (Figure 4.3d).

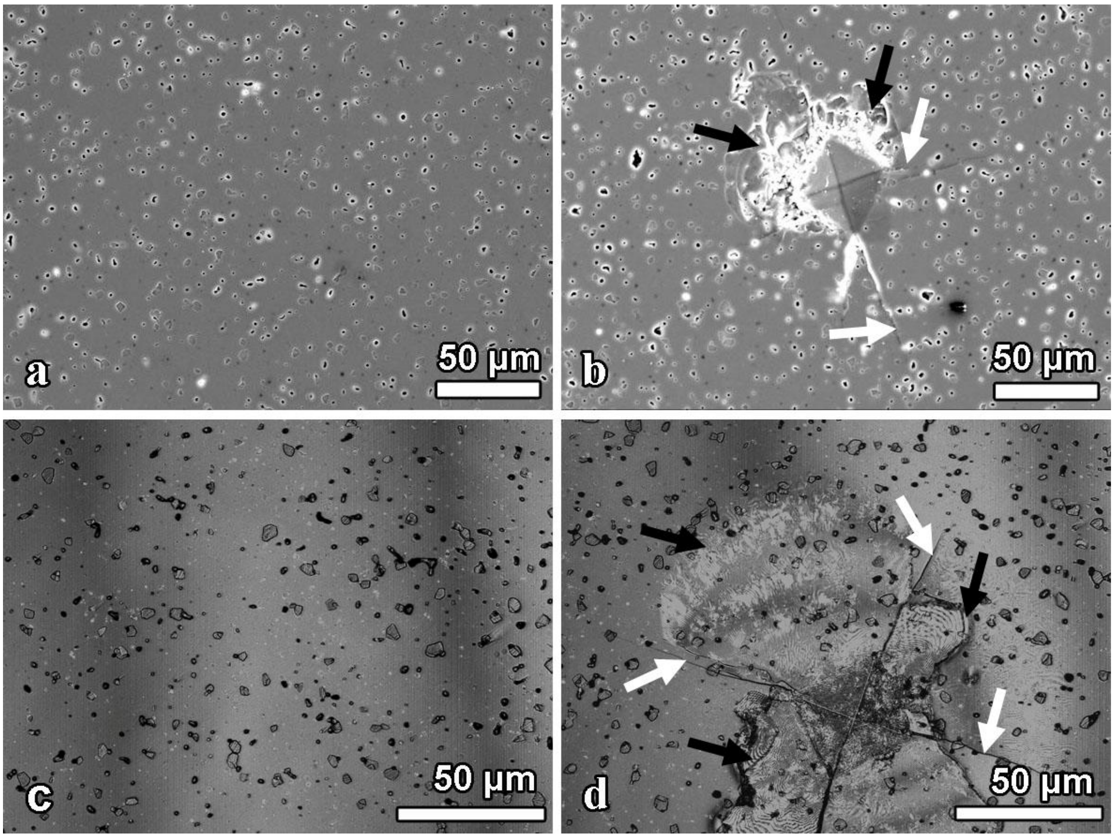

Figure 4.3 SEM image of (a) polished non-cracked HA surface and (b) cracked HA surface and CLSM Z-stack maximum reflection intensity projections of (c) polished non-cracked HA surface and (d) cracked HA surface. On the cracked HA surface, Vickers indentation impression is the center diamond shape. Accompanying radial cracks and lateral crack spalling are pointed out by white and black arrows, respectively.

In a fully developed crack system, microdamage from Vickers indentation contains lateral and radial cracks as well as the centrally located indentation impression as shown in Figure 4.1a. Materials and their microstructural properties such as porosity and grain size may affect the evolvement of the radial/lateral cracks [Osterstock et al. 1996, Tancret and Overstock 2003]. In a given material, the occurrence and development of radial/lateral cracks is load dependent (Chapter 8). The relative frequency for lateral cracks to occur is approximately 95% at 4.91 N in the HA specimens in this study (Chapter 8). The average size of the lateral cracks, *b*, and the half radial crack length, *a*, were 67.3 ± 17.5 µm and 90.6 ± 4.9 µm, respectively (Figure 4.1a).

OB attachment and alignment

OB attachment

At one and two hours post seeding, OBs were still somewhat rounded and not fully attached, but by four hours the cells began to elongate (Figure 4.4). The cell nuclei stained with Hoechst 33342 appeared blue, and the cell membranes stained with Rhodamine Phalloidin Actin stain appeared red (Figure 4.4). A significant increase of OB attachment onto cracked HA specimens was observed at four hours ($p<0.05$), but not at one and two hours (Figure 4.5).

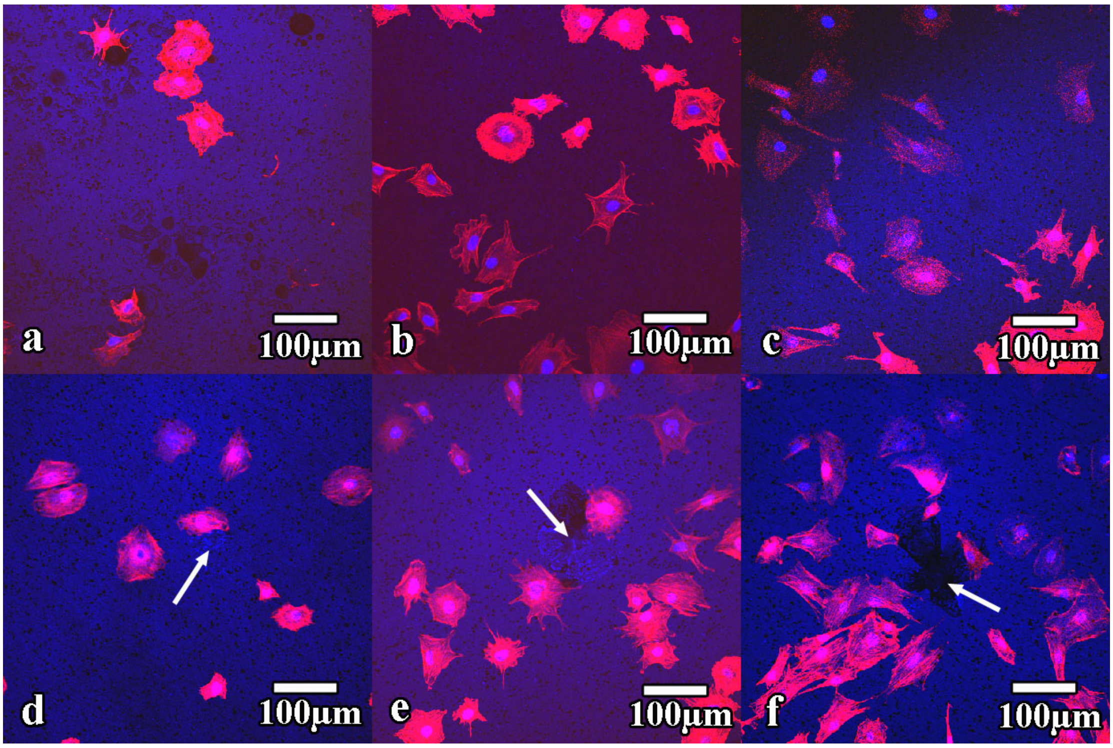

Figure 4.4 CLSM fluorescence images of OBs attached to non-cracked HA specimens at (a) 1 hour, (b) 2 hours and (c) 4 hours, and cracked HA specimens at (d) 1 hour, (e) 2 hours and (f) 4 hours. White arrows show positions of Vickers indentations and cracks. The OBs were stained with Rhodamine Phalloidin (Actin) and Hoescht 33342 (nucleus). The Rhodamine Phalloidin Actin fluorescence stain was excited at 543 nm and emission was detected through a BA560-620 nm emission filter (represented in red). The Hoechst 33342 nucleus stain was excited with UV light at 405 nm and emission was detected through a BA430-470 emission filter (represented in blue).

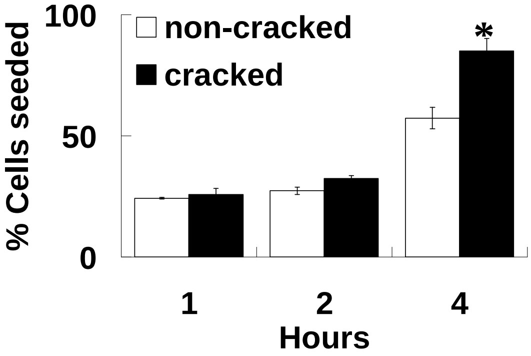

Figure 4.5 OB attachment is increased on cracked HA specimens at 4 hours. OBs were seeded at an initial density of 11,320 cells/cm^2. OB attachments on non-cracked and cracked HA specimens at 1, 2 and 4 hours are represented by the relative percentage of cells seeded. Error bars represent standard error. While no significant difference between OB attachment on non-cracked and cracked HA specimens were detected at 1 and 2 hours, significant increase of OB attachment by approximately 28% on cracked HA specimens was detected at 4 hours

using Student’s t-test (*$p<0.05$). Three specimens were used for each condition and the experiments were tripled.

CLSM micrographs of OB attachment at four hours

Figure 4.6 is a representative CLSM fluorescent micrograph of cells attached on cracked HA at four hours post-seeding. The alignment of the elongated cells towards the indentation center is described by the alignment angle, θ, as shown in Figure 4.6. The alignment angle, θ, was defined by two lines: one line (horizontal, yellow line in Figure 4.6) was drawn from the nucleus of each OB to the indentation center of the cracked samples. The other line (vertical, cyan line in Figure 4.6) was drawn through the nucleus and the longest part of the cell. For the few circular cells, having no apparent elongation (marked by black crosses on Figure 4.6), no alignment angle could be defined.

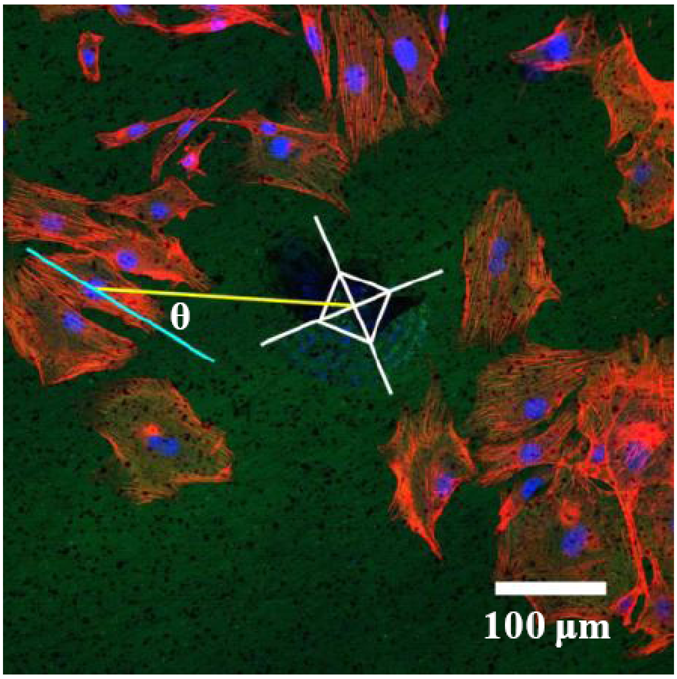

Figure 4.6 Illustration of angle θ between cell elongation direction (cyan line) and line connecting cell nucleus and indentation center (yellow line) on micrographs of cracked HA. The indentation impression and radial crack pattern are illustrated by white lines. The black crosses mark examples of cells showing no apparent elongation direction. The OBs were stained with Rhodamine Phalloidin (Actin) and Hoescht 33342 (nucleus). The Rhodamine Phalloidin Actin fluorescence stain was excited at 543 nm and emission was detected through a BA560-620 nm emission filter (represented in red). The Hoechst 33342 nucleus stain was excited with UV light at 405 nm and emission was detected through a BA430-470 emission filter (represented in blue).

Thus, the circular cells were excluded from the quantitative angular distribution analysis. Yang also excluded these circular cells in a quantitative analysis of OB alignment on grooved substrates [Yang et al. 2008]. A careful examination of the non-cracked HA micrographs showed that 45 out of 534 cells appeared circular with no apparent elongation direction, while in the microcracked HA micrographs, 17 out of 604 cells showed no obvious elongation direction. Thus, approximately 92% and 97% of the cells were elongated on the non-cracked and microcracked HA micrographs, respectively.

Alignment angle (θ) distribution

For the CLSM micrographs of the HA specimens, the alignment angle, θ, for the elongated cells, the coordinates of the crack center, O (X_0, Y_0) and the cell nucleus center C (X, Y) were determined via the software package Datathief [Tummers 2005]. The vector $\overset{\rightarrow}{OC} = (X - X_0, Y - Y_0)$ then gave the relative position of each cell with respect to the indentation center. For each cell, the elongation direction was described by another vector, $\overset{\rightarrow}{EF} = (X_2 - X_1, Y_2 - Y_1)$, where E ($X_1$, Y_1) and F (X_2, Y_2) are two points along the elongated cell filaments. The angle, θ, can then be calculated from equation (1),

$$\theta = arc\left|\cos\theta\right| = arc\left|(\overset{\rightarrow}{OC} \bullet \overset{\rightarrow}{EF}) \Big/ (\left|\overset{\rightarrow}{OC}\right|\left|\overset{\rightarrow}{EF}\right|)\right| \quad (1)$$

For the non-cracked (control) HA specimens, no Vickers indentations were made. Thus, in order to define the angle of alignment for cells on non-cracked HA, artificial origins of polar coordinate system were superimposed on the CLSM micrographs of the non-cracked HA specimens. These artificial origins were superimposed near the center of micrographs for non-cracked HA specimens, similar to the positions of the indentation centers on micrographs of cracked HA.

The alignment angle, θ, of cells can range from 0°to 90°with respect to the microcracked region centered at the indentation center, as shown schematically in Figure 4.7. Since no alignment angle θ could be determined for the few cells with no apparent elongation direction, these cells were excluded from the θ distribution analysis.

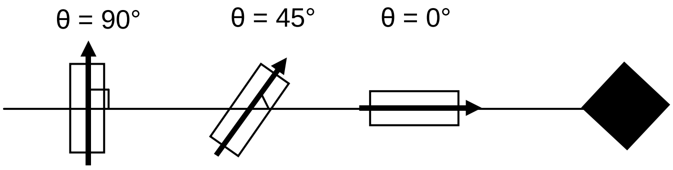

Figure 4.7 A schematic of cells with different elongation directions with respect to the indentation site. Cells with θ < 45° are considered as aligned cells, while cells with θ ≥ 45° are considered as non-aligned cells.

A total of 489 elongated cells from non-cracked HA micrographs and 587 elongated cells from microcracked HA micrographs were considered for the analysis of θ distribution. Figure 8 shows the probability density histograms of θ (probability versus θ) for the elongated cells measured from the CLSM micrographs of both the non-cracked and the cracked HA.

The distributions of the angle θ were then compared to a uniform distribution described by equation (2),

$$f(\theta) = \frac{1}{(b-a)}, a < \theta < b \tag{2}$$

where *a* and *b* are the two parameters for a uniform distribution and give the range of angle θ. The goodness of fit was determined using the Kolmogorov-Smirnov method [Massey 1951]. The uniform distribution of angle θ corresponds to the random cell orientations with respect to the origin of the polar coordinate system [Curray 1956, Fisher et al. 1985]. The θ distribution for OBs from the non-cracked HA micrographs is consistent with the uniform distribution (p>0.05) (Figure 4.8a), whereas the θ distribution for OBs from the microcracked HA micrographs was found to be significantly different from the uniform distribution ($p<0.05$) (Figure 4.8b).

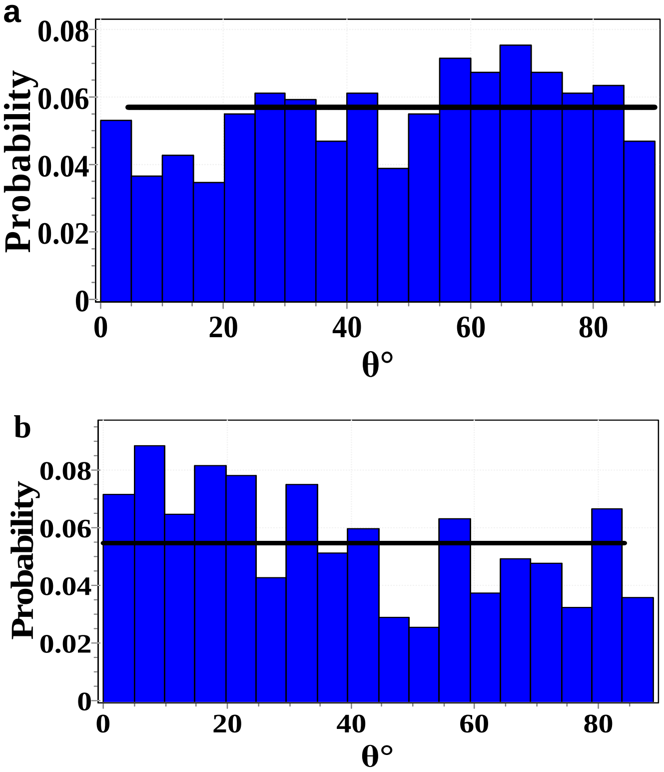

Figure 4.8 Probability density histograms of θ for a) non-cracked HA (N=489) and b) cracked HA (N=587) fit to uniform distribution as shown by the thick solid black line. N is the total number of cells considered in the probability density histograms. The goodness of fit was tested using the Kolmogorov-Smirnov method. The θ distribution for non-cracked HA fitted to uniform distribution ($p>0.05$). The θ distribution for cracked HA did not fit to the uniform distribution ($p<0.05$).

Comparison of aligned and non-aligned cells

When θ is less than 45°, the midpoint of the [0°, 90°] interval, cells with $\theta < 45°$ are considered to be aligned towards the microcracked region (Figure 4.7). To determine whether the OBs on the microcracked HA specimens aligned in the direction of the microcracked zone, centered at the indentation impression center, the cells were divided into three groups according to both their alignment angle and shape: (i) aligned cells ($\theta < 45°$), (ii) non-aligned cells ($\theta \geq 45^\circ$) and (iii) circular, cells for which alignment was indeterminate. The relative fraction of aligned cells ($\theta < 45^\circ$) and non-aligned cells ($\theta \geq 45^\circ$) were then calculated and compared. From the micrographs of non-cracked HA specimens, the relative fraction of aligned cells ($\theta < 45^\circ$) was significantly less ($p<0.05$) than the relative fraction of non-aligned cells ($\theta \geq 45^\circ$ and circular cells) as shown in Figure 4.9a. However, from the micrographs of cracked HA, the relative fraction of aligned cells ($\theta < 45^\circ$) was significantly more ($p<0.05$) than non-aligned cells ($\theta \geq 45^\circ$ and circular cells) as shown in Figure 4.9b.

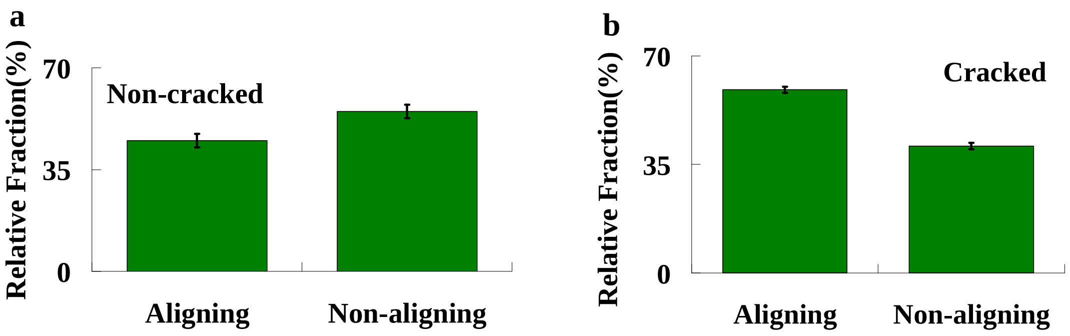

Figure 4.9 The relative fractions of aligned cells ($\theta<45^\circ$) and non-aligned cells ($\theta \geq 45^\circ$ and circular cells) on a) non-cracked HA and b) cracked HA at 4 hours. Significantly more non-aligned cells than aligned cells were detected from non-cracked HA micrographs, while the opposite was observed from cracked HA micrographs. The significance of difference was detected using Student's t-test ($p<0.05$).

The positions of aligning cells on microcracked HA

The location of the aligned cells ($\theta < 45^\circ$) was characterized by the distance (r) between each cell nucleus and the indentation center, which was obtained by calculating the length of vector $\overrightarrow{OC} = (X - X_0, Y - Y_0)$ described in earlier using equation (3),

$$r = \left|\overrightarrow{OC}\right| = \sqrt{(X - X_0)^2 + (Y - Y_0)^2} \qquad (3)$$

The micrographs of the microcracked HA surface were then partitioned into a circle centered at the indentation site, with increasing, concentric 15 µm-wide annuli as shown schematically in Figure 4.10a. The area for the central circle and each annulus was calculated from the 15 µm central circle radius and the 15 µm increments in radius, such that the center circle has an area of 706.85 µm^2, and the nth (n=1, 2, …) annulus has an area of π[15(n+1)]^2-π(15n)^2 (µm^2). The number of aligned cells within the central circle and each ring was then normalized by the circle/annulus area to give the cell density as a function of distance away from the indentation center as shown in Figure 4.10b.

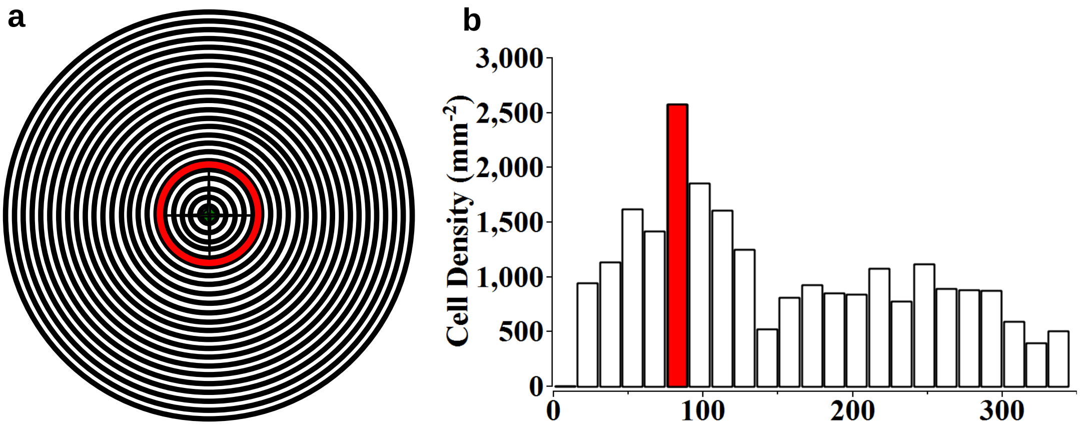

Figure 4.10 The micrograph was partitioned into a central circle of 15 µm in radius and 15 µm wide outer rings (a). The number of OBs with aligned tendency (θ<45°) in the center circle and outer rings (15 µm wide) were counted and normalized by the area respectively (b). Most cells with aligned tendency (θ<45°) were found in the annulus 75 to 90 µm from the indentation center (b), which is around the tip of the radial cracks from Vickers indentation (a).

The surface microcracked zone introduced using Vickers indentation contains the indentation impression, lateral cracks and radial cracks. The average lateral crack size and the half radial crack length were approximately 67.3 ± 17.5 µm and 90.6 ± 4.9 µm, respectively. The boundary region of the microcracked zone as determined by both lateral and radial cracks is thus an annulus approximately 67.3µm to 90.6 µm away from the indentation center. The highest density of aligned cells was found in the ring located 75 µm to 90 µm from the indentation center (Figure 4.10b). This concentric ring was similar in size to the boundary region of the microcracked zone determined by the lateral and radial cracks.

OB growth and maturation

Cell growth was measured to determine if increases in attachment led to more cell growth. However, no significant differences in OB number were detected between microcracked and non-cracked specimens at one, three and five days post-seeding (Figure 4.11), suggesting that OB expansion was similar on both surfaces, despite early differences in surface recognition/attachment.

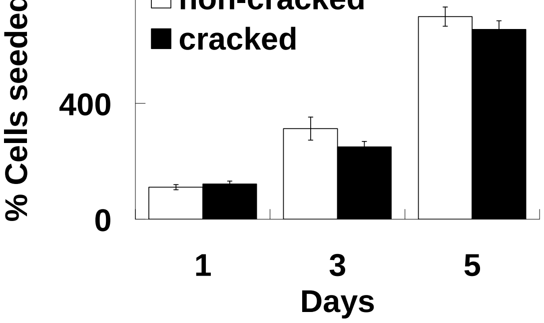

Figure 4.11 OB growth is not affected by the presence of cracks on HA specimens. OBs were seeded at an initial density of 11,320 cells/cm^2. OB growths on non-cracked and cracked HA specimens at 1, 3 and 5 days are represented by the relative percentage of cells seeded. Error bars represent standard errors. No significant differences between OB growths on non-cracked and cracked HA specimens were detected (*$p<0.05$). Three specimens were used for each condition and the experiments were tripled.

Alterations in surface structure and cell attachment can also impact the maturation of OBs, the effect of microcracking on OB phenotype markers were thus investigated. Cells were harvested at 21 days post-seeding, a time when OBs are in a mid to full stage of maturation. First, alkaline phosphatase activity and expression, markers of mid-to-late stage extracellular matrix maturation [Lian et al. 1998, Owen et al. 1990, Quarles et al. 1992] were measured. Cells on the microcracked surface had greater alkaline phosphatase RNA levels and correspondingly greater alkaline phosphatase activity compared to non-cracked surfaces (Figure 4.12).

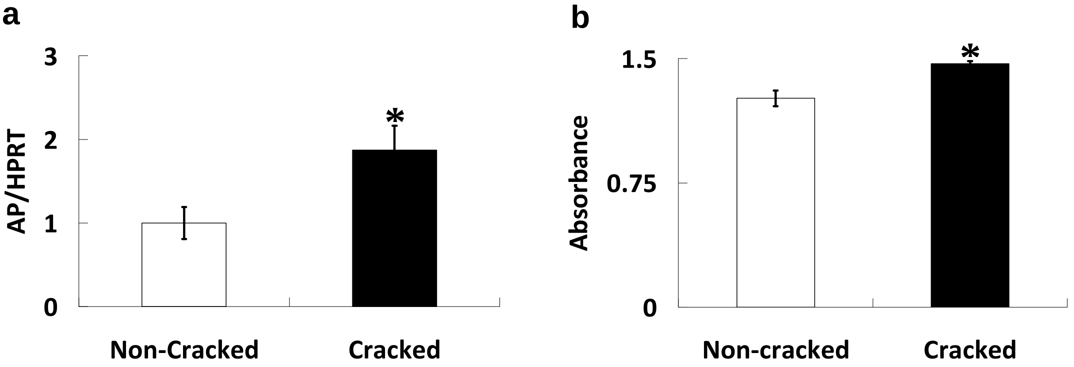

Figure 4.12 OB maturation characterized by (a) AP expression and (b) AP activity was enhanced on cracked HA specimens. OBs were seeded at initial density of 20,000 cells/cm^2. After 21 days of cell culturing, AP gene expression was examined using RNA extracted from cell layers. Gene expression was normalized to levels of an unmodified housekeeping gene, HPRT. AP activity was assessed on cell layers and then measured by spectrophotometer. Significant increases in both (a) AP gene expression and (b) AP activity were detected using Student's t-test (*$p<0.05$). Error bars represent standard errors. Three specimens were used for each condition and the experiments were tripled.

Further analysis of other gene expression levels indicated an increase in Runx-2 (a transcription factor important for OB lineage selection and maturation). Collagen I (a major bone extracellular matrix protein) RNA levels displayed a tendency to increase on HA surfaces but the data was variable and statistical significance could not be reached. Interestingly, no significant changes were observed in osteocalcin expression (a marker of late-stage OB maturation) (Figure 4.13) [Lian et al. 1998, Owen et al. 1990, Quarles et al. 1992].

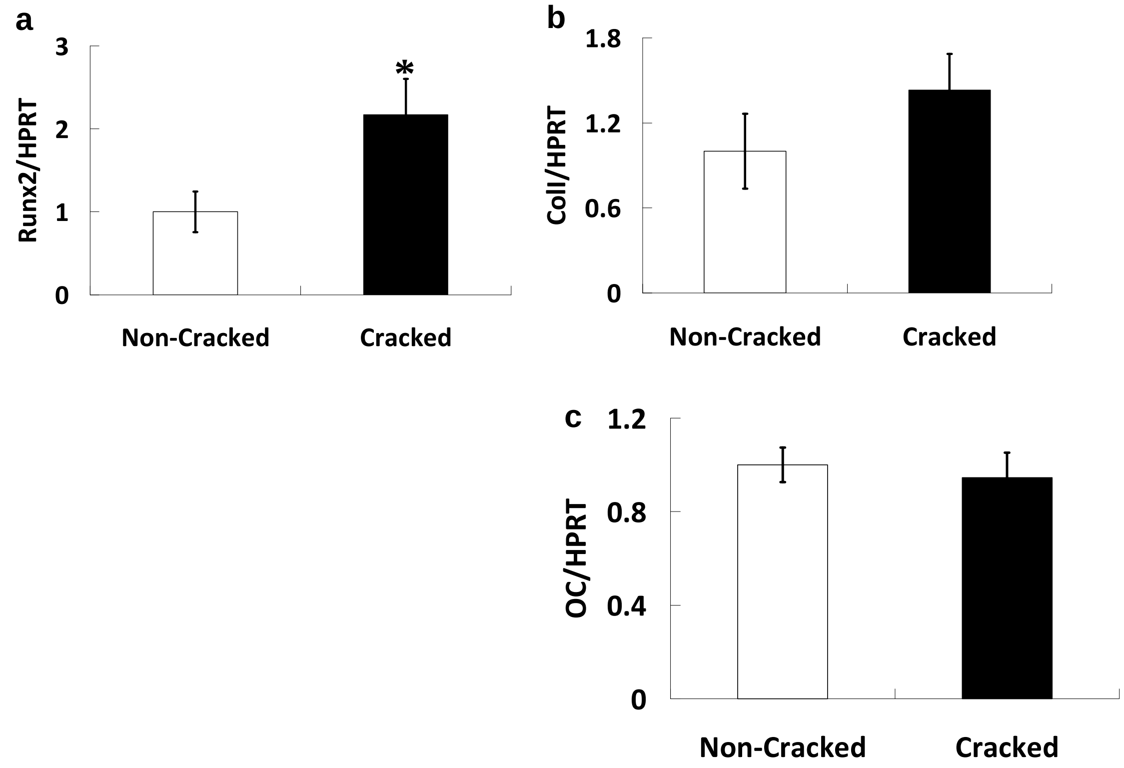

Figure 4.13 (a) Runx2, (b) Col-I and (c) OC expressions on non-cracked and cracked HA at 21 days. All gene expression was examined using RNA extracted from cell layers. Gene expression was normalized to levels of an unmodified housekeeping gene, HPRT. Significant increase in Runx2 expression on cracked HA specimens was detected using Student's t-test (*p ≤ 0.05). No significant differences in Col-I and OC expressions between non-cracked and cracked HA specimens were detected. Error bars represent standard errors. Three specimens were used for each condition and the experiments were tripled.

To determine if the identified phenotypic changes could impact OB bone formation on the cracked HA surface, we imaged OB mineralization on cracked and non-cracked HA at 21 days by CLSM. Surface analyses indicated that significantly more mineral deposition occurred on the cracked HA. The deposited minerals, which contained calcium stained by Xylenol Orange, were shown as orange dots in Figure 4.14. Non-cracked HA (Figure 4.14a) displayed mineral deposition that was scattered uniformly across the surface. In contrast, there was a zone of concentrated mineral deposition at the indentation site on the cracked HA (Figure 4.14b). This concentrated deposition was not apparent in parallel studies on HA scaffolds without cells (data not shown), suggesting that HA cracking stimulates osteoblast bone formation to repair of surface indentations and smooth the surface.

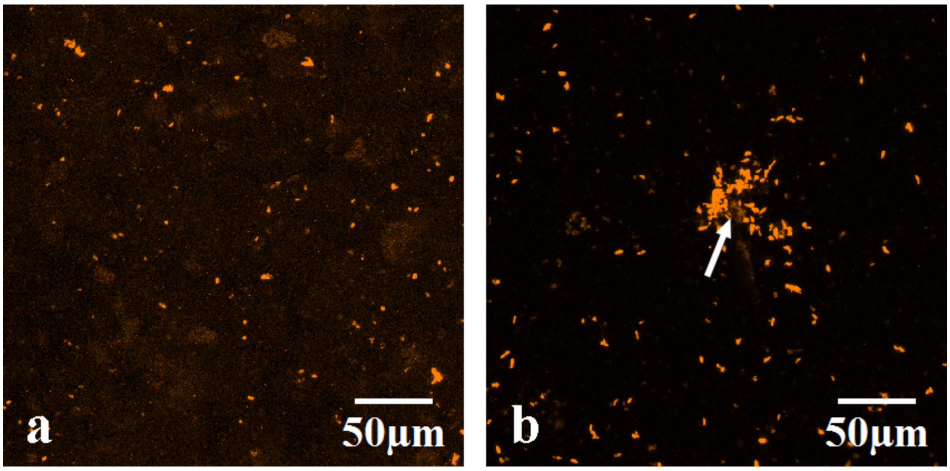

Figure 4.14 CLSM Z-stack maximum fluorescence intensity projections of OB mineral depositions on (a) non-cracked and (b) cracked HA at 21 days. The OBs were pulsed with Xylenol Orange every other day during culturing since day four. The Xylenol Orange fluorescence stain was excited at 543 nm and emission was detected through a BA560-620 emission filter (represented in orange).

DISCUSSION

OB attachment and growth

The interaction of OBs with the substrate surface includes cell attachment or adhesion, cell growth or proliferation, and finally cell differentiation or maturation phases [Anselme 2000]. Attachment or adhesion, being the first phase of OB/substrate interaction, plays an important role in determining the subsequent proliferation and differentiation stages [Anselme 2000]. In this study, the presence of microcracks was observed to increase OB attachment four hours after seeding but not at one or two hours (Figure 4.5). Observed differences between times may be related to the release rate of calcium from the free surface of the HA, the details of which are still under investigation by the authors.

The increase in OB attachment *in vitro* is usually taken as a strong indication for improved biocompatibility of the bone implant substrate [Gough et al. 2004, Balasundaram et al. 2006, Webster et al. 2000, Cai et al. 2006, Lim et al. 2004, Kopecek et al. 2008]. The improvement in observed OB attachment is likely a result of contributions from modification in substrate surface characteristics, such as the surface roughness/area [Gough et al. 2004, Webster et al. 2000 and Cai et al. 2006], the surface chemistry [Shu et al. 2003, Lim et al. 2004, MacDonald et al. 2004, Scotchford et al. 1998], the surface hydrophilicity and the surface free energy [Boyan et al. 2003, Zhao et al. 2005 and 2007, Olivares-Navarrete et al. 2007].

While OB attachment was observed to increase on cracked HA specimens (Figure 4.5), no enhancement in OB growth was observed (Figure 4.11), which showed that an increase in OB attachment did not necessarily lead to more OB growth. In a study conducted by Smith *et al.* OB attachment and growth also showed a similar trend, such that when OB attachment increased, OB growth did not show obvious differences or was even suppressed at longer times [Smith et al. 2006 a]. In another study by Shu et. al. [2003], OB growth was suppressed on HA when compared to plastic culture dishes, but an enhanced OB maturation (increased AP activity) on HA was observed, which is also found in the current study.

OB shape on the CLSM micrographs

We observed two main cell shape phenotypes at 4 hours post-seeding: circular and elongated. The circular cells result from three different cell behaviors: (1) cells not strongly adhered to the surface, as observed at one and/or two hours post seeding; (2) cells with focal adhesions in all directions [Tranquillo et al. 1999]; and/or (3) cells detaching from the surface during apoptosis [Grossman et al. 2002, Numaguchi et al. 2003]. Cell apoptosis is not a major concern in the current study, because HA has been shown to be an excellent substrate for OB culturing [Shu et al. 2003] and as a bone implant material [Hench 1991].

Cells elongate during cell attachment, an essential step for cell motility. Thus, in this study, the preferred elongation direction observed on cracked HA specimens may indicate cell movement towards or away from the microcracked zone. On the other hand, cell elongation also reflects the cell's response to the substrate surface, such that the formation of cytoskeletal focal adhesions is guided by the substrate physical/chemical properties in order to optimize cell functions on the substrate [Weiner et al. 1999, Ziv et al. 1996, Ascenzi et al. 1986, Lenhert et al. 2005, Zhu et al. 2005, Puckett et al. 2008, Yang et al. 2008 and Lee et al. 2006]. In this study, the observed cell elongation towards the microcracked zone was noted specifically at the crack boundaries. Thus, it is likely that the introduction of microcracks disturbed the local physical/chemical environment, which in turn altered the cell elongation direction when the cells were attaching in the vicinity of the microcracked zone.

Distribution of OB alignment angles

The uniform distribution of cell alignment angles, θ, on non-cracked HA specimens indicated that the OBs were randomly oriented and showed no preferential alignment towards the superimposed polar coordinate origins. The random orientation of the elongation axes for the cells also implies a random movement of cells on the non-cracked HA surfaces, which is consistent with observations of random cell movement on isotropic substrate surfaces by Tranquillo [1999] and Selmeczi et al. [2005]. The non-uniform distribution of the cell alignment angles (θ) on microcracked HA (Figure 4.8b) showed that the presence of the microcracks introduced by Vickers indentation affected the cell orientation.

OB alignment towards the microcracked zone

Based on our findings, OBs were more extensively aligned on microcracked HA specimens compared to non-cracked HA specimens, which indicates that the microcracked zone likely influences cell alignment. The elongated OBs that were aligned towards the indentation center may in turn lead to the alignment of the ECM, which interacts with cells through adhesive forces [Numaguchi et al. 2003, Ingber et al. 1989, Singhvi et al. 1994, Huang et al. 1998, Parker et al. 2002]. Alignment of OBs and/or mineralized ECM has been observed by researchers culturing OBs on substrate surfaces with anisotropic topographies, both at the nano- and the micro-scale [Zhu et al. 2005, Puckett et al. 2008, Lenhert et al. 2005, Yang et al. 2008]. The alignment of OBs on substrates with surface grooves was described by qualitative observations of representative micrographs by both Zhu and Puckett; however, no quantification of the cell alignment was conducted in their studies [Zhu et al. 2005, Puckett et al. 2008].

On the other hand, Lenhert and Yang provided a quantitative characterization of OB shape and alignment on the grooved surfaces, where the OB orientation angles were defined by the grooves and the elongation direction of the cells [Lenhert et al. 2005, Yang et al. 2008]. The cells with orientation angles less than 30° were considered to be aligned in Lenhert's study [Lenhert et al. 2005]; while in Yang's study, cells with orientation angles less than 10° were considered aligned [Yang et al. 2008].

Though the standards for defining alignment varied among researchers, the quantitative descriptions of cell alignment along surface grooves all showed significant differences between the proportions of aligned cells on grooved (experimental) and smooth (control) substrate surfaces [Lenhert et al. 2005, Yang et al. 2008]. On the grooved surfaces introduced by lithography techniques, 42% of cells aligned within 30° of the grooves in Lenhert's study [Lenhert et al. 2005], and more than 60% cells aligned within 10° of the grooves in Young's study [Young et al. 2008], while cells showed no preferred orientation on the control substrate surfaces. In cases where grooves/ridges are introduced by abrasion [Calzado-Martin et al. 2011], it is not possible to entirely separate whether the enhanced cell activity is due to the grooves/ridges or the microcracks associated with the abrasion [Couto et al. 1994].

It is important to address the difference between OB alignment towards the localized microcrack zone observed in this study and OB alignment along parallel ridges and/or grooves observed by others [Lenhert et al. 2005, Zhu et al. 2005, Puckett et al. 2008, Yang et al. 2008]. In these OB alignment studies, the focus was on mimicking the anisotropic nature of bone; while in this study, the interest was to determine whether alignment indicated enhanced bone formation around microcracks [Burr and Martin 1993, Mori and Burr 1993, Stafford et al. 1994].

It should be noted that when microcracking occurs *in vivo*, OBs do not necessarily have direct contact with the microcracked sites, but may be generated and migrate from the undamaged bone before mineralizing in the vicinity of the microcracks [Stafford et al. 1994]. The microcracked zone introduced using Vickers indentation is localized microdamage, mimicking the localized damage found from repetitive use injury in humans and animals [Burr and Martin1993, Mori and Burr 1993, Stafford et al. 1994].

In the other studies, cells remained in contact with the parallel ridges/grooves because the ridges or grooves covered the whole surface [Clark et al. 1990 and 1991, Lenhert et al. 2005, Zhu et al. 2005, Puckett et al. 2008, Yang et al. 2008]; while in our study, the cells were in contact with not only the surface microcracks, but also the surrounding un-cracked regions when seeded on the cracked HA (Figure 4.6). It is therefore important to address not only the shape and alignment of cells as discussed above, but also the locations of the aligned cells on the microcracked HA specimens with respect to the localized microcracked zone.

Relationship between aggregated aligned cells and the size of microcracked zone

The majority of the aligned cells were found at the annulus boundary region of the microcracked zone rather than accumulating at the indentation impression. So as not to confuse the Vickers indentation impressions with surface breaking pores, it is useful to note that the indentation impressions in this study have an average diagonal of 44.8 ± 1.4 µm and ~9 µm deep, too shallow to support bone ingrowth [Engh et al.1987, Karageorgiou and Kaplan 2005]. Therefore, it is reasonable that the majority of aligned cells are present at the indentation impression when we assess cell attachment and proliferation.

Bone ingrowth has been shown to occur with pore sizes >100 µm [Engh et al.1987, Karageorgiou and Kaplan 2005], which is comparable to the diameter of the Haversian bone osteons noted by Burg et al. [2000]. The size of the Vickers indentation impression (~45µm) in this study was significantly smaller than the pore size capable of inducing bone ingrowth documented in the literature (100 - 400 µm) [Hulbert et al. 1970, Bobyn et al. 1980, Martens et al. 1980]. Further, although interconnected pores approximately 50 µm in diameter [Klawitter et al. 1976, Itala et al. 2001] were also reported to induce bone ingrowth, the Vickers indentations in this study were not interconnected but isolated from each other. Because the Vickers indentation impression is a shallow divot rather than a real pore, the OB alignment towards the microcracked zone was not likely influenced by the Vickers indentations, but instead by the radial and lateral cracks.

Microcrack boundary defined by radial/lateral cracks

In this study, the length of the radial cracks (181.2 ± 9.8 µm) induced by Vickers indentations was within the range of linear microcracks found in bone (50 to 300 µm) [Taylor et al. 1998, Schaffler et al. 1989, Burr et al. 1990, Burr and Martin 1993, Morri and Burr 1993, Lee 1995, Lee et al. 1998]. These radial cracks thus can be considered as a reasonable model for fatigue microcracking in bone. When microcracking occurs in bone, as well as in engineering ceramics that are not completely dense, the crack propagation can be arrested by pores via crack tip blunting, an important energy absorption mechanism [Kruzic et al. 2003, Deng et al. 2004]. Cracks could also be deflected by the anisotropic collagen matrix in bone [Kruzic et al. 2003], particularly in the transverse directions [Taylor and Lee 1998].

In the HA specimens used in this study, the radial cracks from the Vickers indentations showed enhanced growth within the first hour following indentation, due to the release of residual strain energy from the plastic deformation zone beneath the indentation impression (Chapter 8). The radial crack length then reaches a plateau due to the exhaustion of the residual strain energy (Chapter 8). The radial crack extension in HA is also likely to be disrupted by the surface breaking pores via crack tip blunting [Deng et al. 2004] and/or deflected by grain boundaries [Faber et al. 1983, Suresh et al. 1983]. Thus, crack tip blunting is a likely mechanism inhibiting crack propagation in both bone and HA, which acts to redistribute localized strain energy at the crack tip, inhibiting further crack propagation.

Radial crack tips however only account for part of the microcracked zone introduced by Vickers indentations. The presence of lateral cracks should also be considered, because OBs were observed to align around the entire periphery, rather than merely clustering at the crack tips. Lateral crack chipping from Vickers indentations has been widely used to investigate the abrasive wear, erosive wear, and the surface material removal process in a variety of brittle materials [Ahn et al. 2003, Srinivasam et al. 1990, Thiruvengadaswamy et al. 1993, Swain et al. 1976, Zhang et al. 2000]. Lateral crack chipping in bone, on the other hand, has not been documented. However, in clinical cases [Matic et al. 2004, Suzuki et al. 2009] involving trauma from collisions and sudden falls, bone chipping may occur when a large physical force is applied over a small area of bone. Thus, lateral crack chipping could potentially serve as a model for bone chipping, which differs from fatigue microcracking as modeled by radial cracks.

The observed OB alignment at the periphery of the microcracked zone suggests two possible bone healing processes by examining both the radial and lateral cracks. The first is that crack tip blunting may be activated at the radial crack tips. This resembles bone healing in the case of fatigue microcracking *in vivo* observed by Muir et al. [1999], Zarrinkalam et al. [2005], Taylor and Lee [1998], O’Brien et al. [2003] and Hazenberg et al. [2009]. The second is the possible inhibition of lateral crack chipping that could occur in bone *in vivo*, a concept that has yet to be addressed in the literature.

OB maturation

In this study we found that microcracked HA further enhanced AP gene expression (Figure 4.12a, AP activity (Figure 4.12b) and Runx-2 expression (Figure 4.13a). Collagen I levels also exhibited an increasing trend (Figure

4.13b) but interestingly we did not observe a corresponding increase in osteocalcin (Figure 4.13c). This could indicate that HA and microcracking specifically enhance a subset of maturation associated genes that are associated with osteoblast maturation (Runx-2 and AP) and bone matrix synthesis (AP and Col-I) which are required for bone healing to begin. It is also possible that at a later time point, we would observe a microcrack-induced increase in more advanced maturation markers such as osteocalcin.

Since the main purpose of fabricating a bone tissue engineering implant is to enhance bone healing in the long term, OB maturation is an important reference in judging the biofunctionality of scaffolds. The increase in OB attachment and corresponding enhancement of OB maturation on cracked HA *in vitro* observed in the current study showed that the introduction of microcracks has the potential to enhance bone healing *in vivo*.

CONCLUSION

The current study is based on the knowledge of both the physical properties of HA and accumulated OB behaviors established by our group in previous studies [Hoepfner and Case 2002, 2003, and 2004, Ren et al. 2009, Fan et al. submitted Part I and II 2011, Singh et al. 2005 and 2006, Fan et al. submitted 2011, Case et al. 2005, Smith et al. 2006, Shu et al. 2003, Hossain et al. 2005, Xie et al. 2004]. The HA used in this study had a well-controlled density (~94%) and uniformly distributed spherical and/or quasi-spherical isolated surface breaking pores (2-3 µm in diameter). Vickers indentation was used to model localized microcracking.

The effect of microcracking on OB attachment and maturation has been demonstrated by increased cell attachment, alkaline phosphatase activity, and gene expression in *in vitro* cell studies. OB shape and alignment in the local vicinity of a microcrack was also affected at four hours post-seeding. The observed preferential alignment of OBs to the microcracked zone, especially at the circular boundary region, may in turn lead to enhanced OB maturation and localized mineralization as evidenced by CLSM images showing concentrated mineralization at the indentation center. These observations suggest two possible bone healing mechanisms: crack tip blunting at the radial crack tips and bone chipping inhibition at the lateral crack boundaries.

Though the exact mechanism as to how these cracks affect OB attachment and maturation is still not clear, the benefits of such cracks, in terms of enhanced OB maturation, brings a new dimension to designing scaffolds for bone tissue engineering. Future studies will address the detailed mechanism(s) by studying the local chemical environment in the crack vicinity and by examining the protein conformations at the cracked sites which are hypothesized to present a higher surface energy state. While radial cracks, resembling fatigue microcracking *in vivo*, have been widely observed, future studies will look for evidence of lateral crack chipping in bone, because lateral crack chipping may also trigger bone healing by guiding OB shape and alignment as observed in this study.

REFERENCES

REFERENCES

[Ahn et al. 2003] Ahn Y, Cho N, Lee S, and Lee D. Lateral crack in abrasive wear of brittle materials. Japan Society Mechanical Engineering International Journal Series A. 2003; 26: 140-144.

[An et al. 2011] An B, Liu Y, Arola D, and Zhang D. Fracture toughening mechanism of cortical bone: An experimental and numerical approach. Journal of the Mechanical Behavior of Biomedical Materials. Article in Press.

[Anselme 2000] Anselme K. Osteoblast adhesion on biomaterials. Biomaterials. 2000; 21: 667-681.

[Ascenzi and Benvenuti1986] Ascenzi A and Benvenuti A. Orientation of collagen fibers at the boundary between two successive osteonic lamellae and its mechanical interpretation. Journal of Biomechanics. 1986; 19: 455-463.

[Balasundaram et al. 2006] Balasundaram G, Sato M, and Webster TJ. Using hydroxyapatite nanoparticles and decreased crystallinity to promote osteoblast adhesion similar to functionalize with RGD. Biomaterials 2006; 27: 2798-2805.

[Bobyn et al. 1980] Bobyn JD, Pillar RM, Cameron HU, and Weatherly GC. The optimum pore size for the fixation of porous surface metal implants by ingrowth of bone. Clinical Orthopaedic and Related Research. 1980; 150: 263-270.

[Botolin and McCabe 2006] Botolin S and McCabe LR. Chronic hyperglycemia modulates osteoblast gene expression through osmotic and non-osmotic pathways. Journal of Cellular Biochemistry. 2006. 99: 411-424.

[Boyan et al. 2003] Boyan BD, Lossdorfer S, Wang L, and Zhao G. Osteoblasts generate an osteogenic microenvironment when grown on surfaces with rough microtopographies, European Cells and Materials. 2003; 5: 11-12.

[Brunkner et al. 1996] Brukner P, Bradshaw C, Khan KM, White S, and Crossley K. Stress fractures: A review of 180 cases. Clin J Sport Med. 1996; 6: 85-89.

[Burg et al. 2000] Burg KJL, Porter S, and Kellam JF. Biomaterial Developments for Bone Tissue Engineering. Biomaterials. 2000; 21: 2347-2359.

[Burr 1997] Burr DB. Bone, exercise and stress fractures. Exercise and Sport Sci Rev. 1997; 25: 171-194.

[Burr and Martin1993] Burr DB and Martin RB. Calculating the probability that microcracks initiate resorption spaces. J Biomech. 1993; 26: 613-616.

[Burr et al. 1985] Burr DB, Martin RB, Schaffler MB, and Radin E. Bone remodeling in response to *in vivo* fatigue microdamage. Journal of Biomechanics. 1985; 18: 189-200.

[Burr et al. 1990] Burr DB, Milgrom C, Boyd RD, Higgins WL, Robin G, and Radin EL. Experimental stress fractures of the tibia, Biological and mechanical aetiology in rabbits. Journal of Bone and Joint Surgery. 1990; 72B: 370-375.

[Cai et al. 2006] Cai KJ, Bossert J, and Jandt KD. Does the nanometer scale topography of titanium influence protein adsorption and cell proliferation? Colloids and Surfaces B: Biointerfaces 2006; 49: 136-144.

[Calzado-Martin et al. 2011] Calzado-Martin A, Mendez-Vilas A, Multigner M, Saldana L, Gonzalez-Carrasco JL, and Gonzalez-Martin ML et al. On the role of RhoA/ROCK signaling in contact guidance of bone-forming cells on anisotropic Ti6Al4V surfaces. Acta Biomater 2011; 7: 1890-1901.

[Case et al. 2005] Case ED, Smith IO, and Baumann MJ. Microcracking and porosity in calcium phosphates and the implications for bone tissue engineering. Mater Sci Eng A. 2005; 390: 246-254.

[Clark et al. 1990] Clark P, Connolly P, Curtis AS, Dow JA, and Wilkinson CD. Topographical control of cell behaviour: II. Multiple grooved substrata. Development. 1990; 108: 635-644.

[Clark et al. 1991] Clark P, Connolly P, Curtis AS, Dow JA and Wilkinson CD. Cell guidance by ultrafine topography *in vitro*. J Cell Sci. 1991; 99: 73-77.

[Cowin and Hegedus 1976] Cowin SC and Hegedus DH. Bone remodeling I: theory of adaptive elasticity. J Elasticity. 1976; 6: 313-326.

[Couto et al. 2004] Couto MS, Vanenckevort WJP, and Seal M. Diamond polishing mechanisms - an investigation by scanning-tunneling-microscopy. Phil Mag B 1994; 69: 621-641.

[Curray 1956] Curray JR. The analysis of two-dimensional orientation data. J Geol. 1956; 64: 117-131.

[Curtis and Wilkinson 1998] Curtis AS and Wilkinson CD. Reactions of cells to topography. J Biomaterials Sci, Polymer Ed. 1998; 9: 1313-1329.

[Deng et al. 2004] Deng Z, She J, Inagaki Y, Yang J, Ohji T, and Tanaka Y. Reinforcement by crack-tip blunting in porous ceramics. J Eur Ceram Soc. 2004; 24: 2055-2059.

[Engh et al. 1987] Engh CA, Bobyn JD, and Glassman AH. Porous-Coated Hip Replacement: The Factors Governing Bone Ingrowth, Stress Shielding, and Clynical Results. J Bone Joint Surg 1987; 69B: 45-55.

[Estberg et al. 1996] Esterberg L, Stover SM, Gardner A, Drake CM, Johnson B, and Ardans A. High speed exercise history and catastrophic racing fracture in thoroughbreds. Am J Vet Res 1996; 57: 1549-1555.

[Faber and Evans 1983] Faber KT and Evans AG. Crack deflection processes-II. Experiment. Acta Metall 1983; 31: 577-584.

[Fan et al. submitted 2011] Fan X, Case ED and Baumann MJ. The effect of indentation-induced microcracks on the elastic modulus of hydroxyapatite. To be submitted.

[Fan et al. submitted Part I 2011] Fan X, Case ED, Ren F, Shu Y, Baumann MJ. Weibull analysis of biaxial flexural strength of hydroxyapatite as a function of porosity, Part I. Submitted to J Mechanical Behavior of Biomedical Materials.

[Fan et al. submitted Part II 2011] Fan X, Case ED, Ren F, Shu Y, Baumann MJ. Biaxial flexure strength and elastic modulus of hydroxyapatite as a function of porosity, Part II. Submitted to J Mechanical Behavior of Biomedical Materials.

[Fisher et al. 1985] Fisher NI, Huntington JF, Jackett DR. Spatial analysis of two-dimensional orientation data. Mathematical Geology. 1985; 17: 177-194.

[Gauthier et al. 1998] Gauthier O, Bouler JM, Aguado E, Pilet P, Daculsi G. Macroporous biphasic calcium phosphate ceramics: influence of macropore diamter and macroporosity percentage on bone ingrowth. Biomaterials. 1998; 19: 133-139.

[Gough et al. 2004] Gough JE, Notingher I, and Hench LL. Osteoblast attachment and mineralized nodule formation on rough and smooth 45S5 bioactive glass monoliths, J Biomed Mater Res A 2004; 68: 640-650.

[Grossman 2002] Grossman J. Molecular mechanism of “detachment-induced apoptosis-Anoikis”. Apoptosis. 2002; 7: 247-260.

[Hadjidakis and Androulakis2006] Hadjidakis DJ and Androulakis II. Bone remodeling. Ann NY Acad Sci 2006; 1092: 385-396.

[Harrison 1912] Harrison RG. The cultivation of tissues in extraneous media as a method of morphogenetic study. Anat Rec 1912; 6: 181-193.

[Hazenberg et al. 2009] Hazenberg JG, Hentunen TA, Heino TJ, Kurata K, Lee TC and Taylor D. Microdamage detection and repair in bone: Fracture mechanics, histology, cell biology. Tech Health Care. 2009; 17: 67-75.

[Hench 1991] Hench LL. Bioceramics: From concept to clinic. J Am Ceram Soc 1991; 74: 1487-1510.

[Hing et al. 2003] Hing KA, Best SM, Tanner KE, Bonfield W, and Revell PA. J Biomed Mater Res A. 2003; 68: 187-200.

[Hoepfner and Case 2002] Hoepfner TP and Case ED. The porosity dependence of the dielectric constant for sintered hydroxyapatite. J Biomed Mater Res 2002; 60: 643-650.

[Hoepfner and Case 2003] Hoepfner TP and Case ED. The influence of the microstructure on the hardness of sintered hydroxyapatite. Ceram Int 2003; 29: 699-706.

[Hoepfner and Case 2004] Hoepfner TP and Case ED. An estimate of the critical grain size for microcracks induced hydroxyapatite by thermal expansion anisotropy. Mater Lett 2004; 58: 489 -492.

[Hossain et al. 2005] Hossain M, Irwin R, Baumann MJ and McCabe LR. Hepatocyte growth factor (HGF) adsorption kinetics and enhancement of osteoblast differentiation on hydroxyapatite surfaces. Biomaterials 2005; 26: 2595-2602.

[Huang et al. 1998] Huang S, Chen CS, Ingber DE. Control of cyclin Dl, p27kipl, and cell ccle progression in human capillary endothelial cells by cell shape and cytoskeletal tension. Molecular Biology of Cell. 1998; 9: 3179-3293.

[Huiskes et al. 1987] Huiskes R, Weinans H, Grootenboer HJ, Dalstra M, Fudala B and Slooff TJ. Adaptive bone-remodeling theory applied to prosthetic-design analysis. J Biomech 1987; 20: 1135-1150.

[Hulbert et al. 1970] Hulbert SF, Young RA, Mathew RS, Klawitter JJ, Talbert CD, Stelling FH. Potential of ceramic materials as permanently implantable skeletal prostheses. J Biomed Mater Res. 1970; 4: 433-456.

[Ingber 2002] Ingber DE. Mechanical signaling and the cellular response to extracellular matrix in angiogenesis and cardiovascular physiology. Circulation

Res. 2002; 91: 877-887.

[Ingber and Folkman 1989] Ingber DE, Folkman J. How does extracellular matrix control capillary morphogenesis? Cell. 1989; 58: 803-805.

[Itala et al. 2001] Itara AI, Ylanen HO, Ekholm C, Karlsson KH, Aro HT. Pore diameter of more than 100 μm is not requisite for bone ingrowth in rabbits. J Biomed Mater Res. 2001; 58: 679-683.

[Karageorgiou 2005] Karageorgiou V and Kaplan D. Porosity of 3D biomaterial scaffolds and osteogenesis. Biomaterials. 2005; 26: 5474-5491.

[Klawitter et al. 1976] Klawitter JJ, Bagwell JG, Weinstein AM, Sauer BW, and Pruitt JR. An Evaluation of Bone Growth into Porous High Density Polyethylene. J Biomed Mater Res. 1976; 10: 311-323.

[Kopecek et al. 2008] Kopecek M, Bacakova L, Vacik J, Fendrych F, Vorlicek V, Kratochvilova I et al. Improved adhesion, growth and maturation of human bone-derived cells on nanocrystalline diamond films. Physica Status Solidi a-Appl Mater Sci 2008; 205: 2146-2153.

[Kruzic et al. 2003] Kruzic JJ, Nalla RK, Kinney JH, and Ritchie RO. Crack blunting, crack bridging and resistance-curve fracture mechanics in dentin: effect of hydration. Biomaterials. 2003; 24: 5209–5221.

[Kujala et al. 2003] Kujala S, Ryhanen J, Danilov A and Tuukkanen J. Effect of porosity on the osteointegration and bone ingrowth of a weight-bearing nickel-titanium bone graft substitute. Biomaterials. 2003; 24: 4691-4697.

[Lee 1995] Lee TC. Functional adaptation in compact bone. Ph. D. Thesis, Univeristy of Dublin.

[Lee et al. 1998] Lee TC, Myers ER and Hayes WC. Fluorescence-aided detection of microdamage in compact bone. J Anat. 1998; 193: 179-184.

[Lee et al. 2006] Lee DH, Park BJ, Lee MS, Lee JW, Kim JK, Yang HC, and Park JC. Chemotactic migration of human mesenchymal stem cells and MC3T3-E1 osteoblast-like cells induced by cos-7 cell line expressing rhBMP-7. Tissue Engineering. 2006; 12: 1577-1586.

[Leheup et al. 1994] Leheup ER, Zhang D, and Moon JR. The Effect of Density on Fretting Wear of Sintered Iron. Wear. 1994; 176: 111-119.

[Lenhert et al. 2005] Lenhert S, Meier MB, Meyer U, Chi L, Wiesmann HP.

Osteoblast alignment, elongation and migragation on grooved polystyrene surfaces patterned by Langmuir-Blodgett lithography. Biomaterials. 2005; 26: 563-570.

[Lian et al. 1998] Lian JB, Stein GS, Stein JL, van Wijnen AJ. Osteocalcin gene promoter: Unlocking the secrets for regulation of osteoblast growth and differentiation. J Cellular Biochem. 1998. Suppl. 30-31: 62-72.

[Lim et al. 2004] Lim JY, Liu X, Vogler EA, Donahue HJ. Systematic variation in osteoblast adhesion and phenotype with substratum surface characteristics. J Biomed Mater Res Part A 2004; 68: 504-512.

[MacDonald et al. 2004] MacDonald DE, Rapuano BE, Deo N, Stranick M, Somasundaran P, Boskey AL. Thermal and chemical modification of titanium-aluminum-vanadium implant materials: effects on surface properties, glycoprotein adsorption, and MG63 cell attachment. Biomaterials 2004; 25: 3135-3146.

[Martens et al. 1980] Martens M, Ducheyne P, De Meester P, Mulier JC. Skeletal fixation of implants by bone ingrowth into surface pores. Arch Orthop Traum Surg. 1980; 97: 111-116.

[Martin 1992] Martin RB. A theory of fatigue damage accumulation and repair in cortical bone. J Orthop Res. 1992; 10: 818-825.

[Martin and Burr 1989] Martin RB and Burr DB. The structure, function and adaptation of cortical bone. Raven Press. 1989. New York.

[Massey 1951] Massey FJ. The Kolmogorov-Smirnov test for goodness of fit. J Am Stat Assoc. 1951; 46: 68-78.

[Matic and Manson 2004] Matic DB, Manson PN. Biomechanical analysis of hydroxyapatite cement cranioplasty. J Craniofacial Surg. 2004; 15: 415-422.

[McCabe et al. 1996] McCabe LR, Banerjee C, Kundu R, Harrison RJ, Dobner PR, Stein JL et al. Developmental expression and activities of specific Fos and Jun proteins are functionally related to osteoblast maturation: Role of Fra-2 and Jun D during differentiation. Endocrinology. 1996; 137: 4398-4408.

[Mori and Burr 1993] Mori S, Burr DB. Increased intracortical remodeling following fatigue damage. Bone. 1993; 14: 103-109.

[Motyl et al. 2011] Motyl KJ, Raetz M, Tekalur SA, Schwartz RC, McCabe LR. CAAT/enhancer binding protein beta-deficiency enhances type 1 diabetic bone phenotype by increasing marrow adiposity and bone resorption. Am J Physiol Regul Integr Comp Physiol 2011; 300: R1250-R1260.

[Muir et al. 1999] Muir P, Johnson KA and Ruaux-Mason CP. *In vivo* matrix microdamage in a naturally occurring canine fatigue fracture. Bone 1999; 25: 571-576.

[Numaguchi et al. 2003] Numaguchi Y, Huang S, Polte TR, Eichler GS, Wang N and Ingber DE. Caldesmon-dependent switching between capillary endothelial cell growth and apoptosis through modulation of cell shape and contractility. Angiogenesis. 2003; 6: 55-64.

[O’Brien et al. 2003] O’Brien FJ, Taylor D, Lee TC. Microcrack accumulation at different intervals during fatigue testing of compact bone. J Biomech 2003; 36: 973-980.

[Olivares-Navarrete et al. 2007] Olivares-Navavrrete R, Raz P, Zhao G, Chen J, Wieland M, Cochran DL et al. Integrin α2β1 plays a critical role in osteoblast response to micron-scale surface structure and surface energy of titanium substrates. Proc National Acad Sci 2007; 105: 5767-15772.

[Osterstock et al. 1996] Osterstock F, Monot I, Desgardin G, Mordike BL. Influence of grain size on the toughness and thermal shock resistance of polycrystalline $YBa_2Cu_3O_7$-delta. J Eur Ceram Soc. 1996; 16: 687-694.

[Owen 1et al. 990] Owen TA, Aronow M, Shalhoub V, Barone LM, Wilming L, Tassinari MS et al. Stein GS. Progressive development of the rat osteoblast phenotype in vitro reciprocal relationships in expression of genes associated with osteoblast proliferation and differentiation during formation of the bone extracellular-matrix. J Cell Phys 1990; 143: 420-430.

[Parker et al. 2002] Parker KK, Brock AL, Brangwynne C, Mannix RJ, Wang N, Ostuni E, Geisse NA, Adams JC, Whitesides GM, Ingber DE. Directional control of lamellipodia extension by constructing cell shape and orienting cell tractional forces. The FASEB Journal. 2002; 16: 1195-1204.

[Pineda et al. 1996] Pineda LM, Büsing M, Meinig RP, Sylwester Gogolewski S. Bone regeneration with resorbable polymeric membranes: III. Effect of poly(L-lactide) membrane pore size on the bone healing process in large defects. J Biomed Mater Res. 1996; 31: 385-394.

[Prendergast and Taylor 1994] Prendergast PJ and Taylor D. Prediction of bone adaptation using damage accumulation. J Biomech. 1994; 27: 1067-1076.

[Puckett et al. 2008] Puckett S, Pareta R, Webster TJ. Nano rough micron patterned titanium for directing osteoblast morphology and adhesion. Int J Nanomed. 2008; 3: 229-241.

[Quarles et al. 1992] Quarles LD, Yohay DA, Lever LW, Caton R, Wenstrup RJ. Distinct proliferative and differentiated stages of murine MC3T3-E1 cells in culture – An in vitro model of osteoblast development. J Bone Mineral Res. 1992. 7: 683-692.

[Radtke et al. 2003] Radtke CL, Danova NA, Scollay MC, Santschi EM, Markel MD, Gomez TD and Muir P. Macroscopic changes in the distal ends of the third metacarpal and metatarsal bones of thoroughbred racehorses with condylar fractures. Am J Vet Res. 2003; 64: 1110–1116.

[Ren et al. 2009] Ren F, Case ED, Morrison AQ, Tafesse M, Baumann MJ. Resonant ultrasound spectroscopy measurement of Young's modulus, shear modulus and Poisson's ratio as a function of porosity for alumina and hydroxyapatite. Phil Mag 2009; 89: 1163-1182.

[Schaffler et al. 1989] Schaffler MB, Radin EL, and Burr DB. Mechanical and morphological effects of strain rate on fatigue of compact bone. Bone. 1989; 10: 207-214.

[Scotchford et al. 1998] Scotchford CA, Cooper E, Leggett GJ, Downes S. Growth of human osteoblast-like cells on alkanethiol on gold self-assembled monolayers: The effect of surface chemistry. J Biomed Mater Res 1998; 41: 431-442.

[Selmeczi et al. 2005] Selmeczi D, Mosler S, Hagedorn PH, Larsen NB, and Flyvbjerg H. Cell motility as persistent random motion: Theories from experiments. Biophysical Journal. 2005; 89: 912-931.

[Shu et al. 2003] Shu R, McMullen R, Baumann MJ, McCabe LR. Hydroxyapatite accelerates differentiation and suppresses growth of MC3T3-E1 osteoblasts. J Biomed Mater Res A. 2003; 67: 1196-1204.

[Singh et al. 2005] Singh D, Gutierrez-Mora F, de la Cinta Lorenzo-Martin M, Routbort JL, and Case ED. Plastic deformation of hydroxyapatites and its application to joining. Int J Appl Ceram Tech 2005; 2: 247-266.

[Singh et al. 2006] Singh D, de la Cinta Lorenzo-Martin M, Gutierrez-Mora F, Routbort JL, and Case ED. Self-joining of zirconia/hydroxyapatite composites using a plastic deformation process. Acta Biomater 2006; 2: 669-675.

[Singhvi et al. 1994] Singhvi R, Kumar A, Lopez GP, Stephanopoulos GN, Wang DI, Whitesides GM and Ingber DE. Engineering cell shape and function. Science. 1994; 264: 696-698.

[Smith et al. 2006 a] Smith IO, McCabe LR, Baumann MJ, MC3T3-E1 osteoblast attachment and proliferation on porous hydroxyapatite scaffolds fabricated with nanophase powder. Int J Nanomed. 2006; 1: 189-194.

[Smith et al. 2006 b] Smith IO, Baumann MJ, Case ED. Induced microcracking affects osteoblast attachment on hydroxyapatite scaffolds for tissue engineering. Am J Biochem Biotech. 2006; 2: 105-110.

[Soballe et al. 1992] Soballe K, Hansen ES, B-Rasmussen H, Jorgensen PH, Bunger C. Tissue ingrowth into titanium and hydroxyapatite-coated implants during stable and unstable mechanical conditions. J Orthop Res. 1992; 10: 285-299.

[Srinivasam et al. 1990] Srinivasam S, Russ JC, and Scattergood RO. Fractal analysis of erosion surfaces. J Mater Res. 1990; 5: 2616-2619.

[Stafford et al. 1994] Stafford HJ, Roberts MT, Oni O, Hay J, and Gregg P. Localization of bone-forming cells during fracture healing by osteocalcin immunocytochemistry: An experimental study of the rabbit tibia. J Orthop Res. 1994; 12: 29-39.

[Suresh 1983] Suresh S. Crack deflection: Implications for the growth of long and short fatigue cracks. Metall Mater Trans A . 1983; 14: 2375-2385.

[Suzuki et al. 2009] Suzuki A, Nouh F, Soeharno H, Jansen S. Traumatic allogenic bone implantation. Eur J Trauma Emerg Surg. 2009; 35: 190-191.

[Swain and Lawn 1976] Swain MV and Lawn BR. Indentation fracture in brittle rocks and glasses. Int J Rock Mechan Mining Sci & Geomech Abs. 1976; 13; 311-319.

[Tancret and Overstock 2003] Tancret F, Overstock F. Indentation behavior of porous materials: application to the Vickers indentation cracking of ceramics. Phil Mag 2003; 83: 125-136.

[Taylor 1997] Taylor D. Bone maintenance and remodeling: A control system based on fatigue damage. J Orthop Res. 1997;15: 601-606.

[Taylor and Lee 1998] Taylor D and Lee TC. Measuring the shape and size of microcracks in bone. J Biomech. 1998; 31: 1177-1180.

[Taylor and Prendergast 1995] Taylor D and Prendergast PJ. Damage accumulation in compact bone – a fracture mechanics approach to estimate damage and repair rates. Adv Bioeng. 1995;13: 337-338.

[Thiruvengadaswamy and Scattergood 1993] Thiruvengadaswamy R and Scattergood RO. Indentation-cycling tests on soda-lime glass. J Am Ceram Soc 1993; 76: 1611-1614.

[Tranquillo 1999] Tranquillo RT. Self-organization of tissue-equivalents: the nature and role of contact guidance. Biochem Soc Symp. 1999; 65: 27-42.

[Tummers 2005] Tummers B. DataThief III manual v. 1.1. 2005; 1-52.

[Verborgt et al. 2000] Verborgt O, Gibson GJ, Schaffler MB. Loss of osteocyte integrity in association with microdamage and bone remodeling after fatigue in vivo. J Bone Miner Res 2000; 15: 60-67.

[Wang et al. 2006] Wang YH, Liu Y, Maye P, Rowe DW. Examination of mineralized nodule formation in living osteoblastic cultures using fluorescent dyes. Biotechnol Prog 2006; 22: 1697-1701.

[Webster et al. 2000] Webster TJ, Ergun C, Doremus RH. Specific proteins mediate enhanced osteoblast adhesion on nanophase ceramics. J Biomed Mater Res. 2000; 51: 475-483.

[Weiner et al. 1999] Weiner S, Traub W, Wagner HD. Lamellar bone: structure-function relations. J Struct Bio. 1999; 126: 241-255.

[Weiss 1941] Weiss P. Nerve patterns: The mechanics of nerve growth. Growth (suppl.) 1941; 5: 163-203.

[Xie et al. 2004] Xie J, Baumann MJ, McCabe LR. Osteoblasts respond to hydroxyapatite surfaces with immediate changes in gene expression. J Biomed Mater Res 2004; 71: 108-117.

[Yang et al. 2008] Yang J, Ting Y, Lai J, Liu H, Fang H, Tsai W. Quantitative analysis of osteoblast-like cells (MG63) morphology on nanogrooved substrata with various groove and ridge dimensions. J Biomed Mater Res A. 2009; 90: 629-640.

[Zarrinkalam et al. 2005] Zarrinkalam KH, Kuliwaba JS, Martin RB, Wallwork MA, Fazzalari NL. New insights into the propagation of fatigue damage in cortical bone using confocal microscopy and chelating fluorochromes. Eur J Morph. 2005; 42: 81-90.

[Zhang et al. 2000] Zhang QH, Wu CL, Sun JL and Jia ZX. The mechanism of material removal in ultrasonic drilling of engineering ceramics. Proc the Inst Mechan Eng B. 2000; 214: 805-810.

[Zhao et al. 2005] Zhao G, Schwartz Z, Wieland M, Rupp F, Geis-Gerstorfer J, Cochran DL, Boyan BD. High surface energy enhances cell response to titanium substrate microstructure. J Biomed Mater Res A 2005; 74: 49-58.

[Zhao et al. 2007] Zhao G, Raines AL, Wieland M, Schwartz Z, and Boyan BD. Requirement for both micron- and submicron scale structure for synergistic responses of osteoblasts to substrate surface energy and topography. Biomaterials 2007; 28: 2821-2829.

[Zhu et al. 2005] Zhu B, Lu Q, Yin J, Hu J, and Wang Z. Alignment of osteoblast-like cells and cell-produced collagen matrix induced by nanogrooves. Tissue Eng. 2005; 11: 825-834.

[Ziv et al.1996] Ziv V, Wagner HD, and Weiner S. Microstructure microhardness relations in parallel-fibered and lamellar bone. Bone. 1996; 18: 417-428.

CHAPTER 5

LOCAL SURFACE DAMAGE ACCELERATES HYDROXYAPATITE DISSOLUTION IN DISTILLED WATER

INTRODUCTION

Hydroxyapatite (HA or $Ca_{10}(PO_4)_6(OH)_2$) is widely used to supplement bone/dental grafts [LeGeros 2002, Wetzell et al. 1995, Yoshikawa et al. 2000], as a scaffold for bone tissue engineering [Karageorgiou and Kaplan 2005, Wei and Ma 2004, Hollister et al. 2002], and as a structural support material for catalysts, heavy metal removal, and sensors [Mori et al. 2003 and 2004, Venugopal and Scurrell 2003, Nagai and Nishino 1988, Owada et al. 1989]. During material handling and application, localized damage such as scratches and cracks can be generated, which may alter the local chemical/mechanical environment and the dissolution behavior of the material [Li et al. 2009]. The dissolution behavior of HA is important as it releases free calcium ions which affects the biofunctionality of HA. Increases in local calcium ion concentration, released as a result of the biological dissolution of implanted calcium phosphate coatings, was shown to influence mineralization *in vitro* [Morgan et al. 1996]. In Chang et al.'s [2000] study, supplementing with calcium ions was shown to promote bone cell mineralization. In another *in vitro* study by Yang et al. [2004], elevated extracellular calcium ion levels were also observed to induce cell to matrix mineralization. The biological dissolution of hydroxyapatite giving rise to an increased calcium ion concentration is thus likely associated with the biological response of bone cells *in vitro* [Ducheyne et al. 1993]. Besides calcium, phosphate ions, released as the HA dissolves, have also been shown to play a role in regulating osteoblast differentiation [Beck 2003] and apoptosis [Meleti et al. 2000].

The dissolution behavior of HA along with its mechanical stability in aqueous environments is well documented in the literature [Fazan and Marquis 2000, Zhang et al. 2003]. However, far less attention has been paid to HA dissolution around localized surface damage such as scratches and/or cracks, which are associated with local residual stresses. These residual stresses were found to affect the dissolution of HA coatings as shown by Han et al. [2001]. Also, in studies by Reis et al. [1994] and Raynaud et al. [1998], the degradation of HA was found to accelerate when the HA was subjected to cyclic tensile stresses.

In the current study, local surface damage was introduced to HA using the well-established Vickers indentation method, which generates consistent indentation impressions and radial/lateral crack patterns at each loading condition. The surface morphology evolution during dissolution of locally damaged HA was imaged using environment scanning electron microscopy (ESEM). The dissolution behavior of HA in distilled water, with and without indenting, were compared by measuring the calcium ion concentration over immersion periods ranging from 1 hour to 7 days.

MATERIALS AND METHODS

Hydroxyapatite (HA) specimens were made from fine powders (Taihei

Chemical Industry, Osaka, Japan) with a vendor specified particle size of 4 to 6 µm. Powders were uniaxially pressed at 27.7 MPa for 1 minute in a 32 mm diameter steel pellet die. The green powder compacts were then sintered at 1360ºC for 4 hours in an electrical resistance furnace (CM Inc., Model #0100277, Bloomfield, NJ) at a ramp rate of 10ºC/minute during both heating and cooling. The sintered specimen surfaces were polished using diamond paste of grit size down to 0.5 µm prior microindentation.

Vickers indentation was used to introduce local damage to the specimen surfaces using Shimadzu microhardness tester (HMV2000, Kyoto, Japan) at a peak indentation load of 4.91 N. The loading time at the peak load was 5 seconds and both the loading and unloading rates were 70 µm/s. The indentations were made in a 7X7 grid pattern at 2-mm intervals as described in the previous chapter.

Both the polished specimens (control group) and indented specimens (experiment group) were immersed in distilled water and maintained at 37ºC which mimics the normal body temperature. The immersion periods (1 hr, 1.5 hr, 2 hr, 3 hr, 4 hr, 6 hr, 8 hr, 13 hr, 18 hr, 1 day, 2 days, 3 days, 4 days, 5 days, and 7days) ranged from 1 hour to 7 days. The dissolution of one representative indentation impression and its accompanying radial/lateral cracks were imaged using ESEM at 0, 4, and 24 hours.

HA dissolution was characterized by measuring the calcium ion (Ca^{2+}) concentration in distilled water sampled at each time interval using atomic absorption spectrophotometry (AAS, model 3110, PerkinElmer, Massachusetts, 0.01 mg/L) where the emission light wavelength for Ca^{2+} is 422.7 nm.

RESULTS AND DISCUSSION

ESEM of indentation damage during HA dissolution

ESEM was used to capture the HA surface dissolution in and around the indentations and accompanying cracks (0 immersion time) and following immersion in distilled water for 4 and again for 24 hours. Figure 5.1 shows the morphological evolution of the same indentation impression prior to water immersion as well as 4 and 24 hours after immersion.

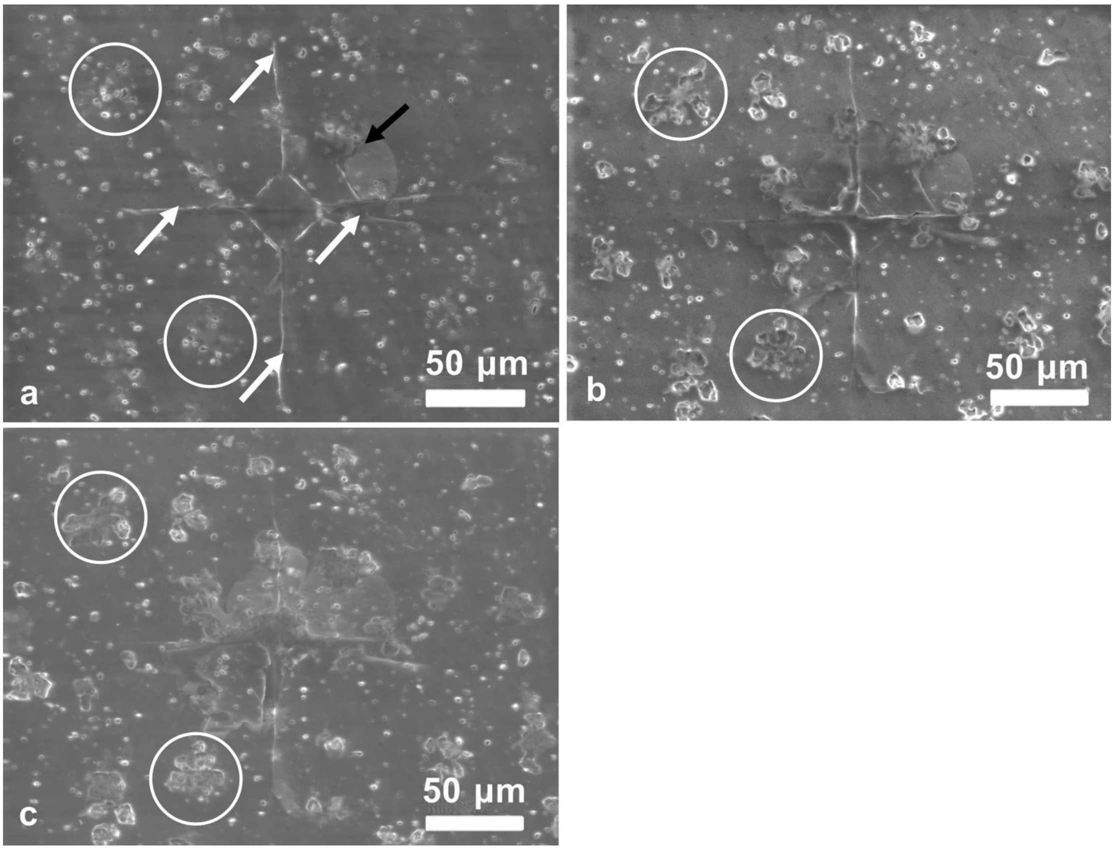

Figure 5.1 ESEM images of the same indentation impression on HA surface (a) before immersing in distilled water, (b) 4 hours after immersion in distilled water, and (c) 24 hours after immersion in distilled water.

Figure 5.1a depicts the indentation impression, radial cracks (white arrow) and lateral crack (black arrow) prior to distilled water immersion. The indentation impression is characterized by sharp edges and a readily distinguishable diagonal cross formed from the rectangular pyramid shape of the Vickers indenter tip. Two pairs of radial cracks extended along the indent impression in a diagonal direction (white arrows). One instance of quarter-plate lateral crack spalling was observed in the upper right region (black arrow). Surrounding the indentation impression, and the radial/lateral cracks, were isolated spherical and quasi-spherical pores, uniformly distributed across the surface. The occasional pore cluster was also present (white circles).

After immersion in distilled water for 4 hours (Figure 5.1b), the indentation impression edges became less distinct when compared to no immersion time (Figure 5.1a). The surface radial cracks appeared to open up in the indentation impression rather than opening at the indentation diagonals as shown in Figure 5.1a. Also, more lateral crack spalling appeared in the upper left, upper right, and lower left regions as indicated by the black arrows. The isolated pore clusters prior to water immersion (white circles, Figure 5.1a) have now coalesced, forming larger surface cavities (white circles, Figure 5.1b).

Following 24 hours of immersion in distilled water (Figure 5.1c), the indentation impression lost its distinguishable diamond shape. The radial crack openings which appeared in the indentation impression at 4 hours (Figure 5.1b) disappeared by 24 hours (Figure 5.1c). On the other hand, lateral cracks became more apparent on the surface and appeared to coalesce with some of the surface pore clusters (Figure 5.1c) that appeared at early immersion times (Figure 5.1a and b).

AAS measurements of HA dissolution and surface area increase

The concentration of calcium ions released into distilled water from both non-cracked and cracked HA as a function of time are shown in Figure 5.2.

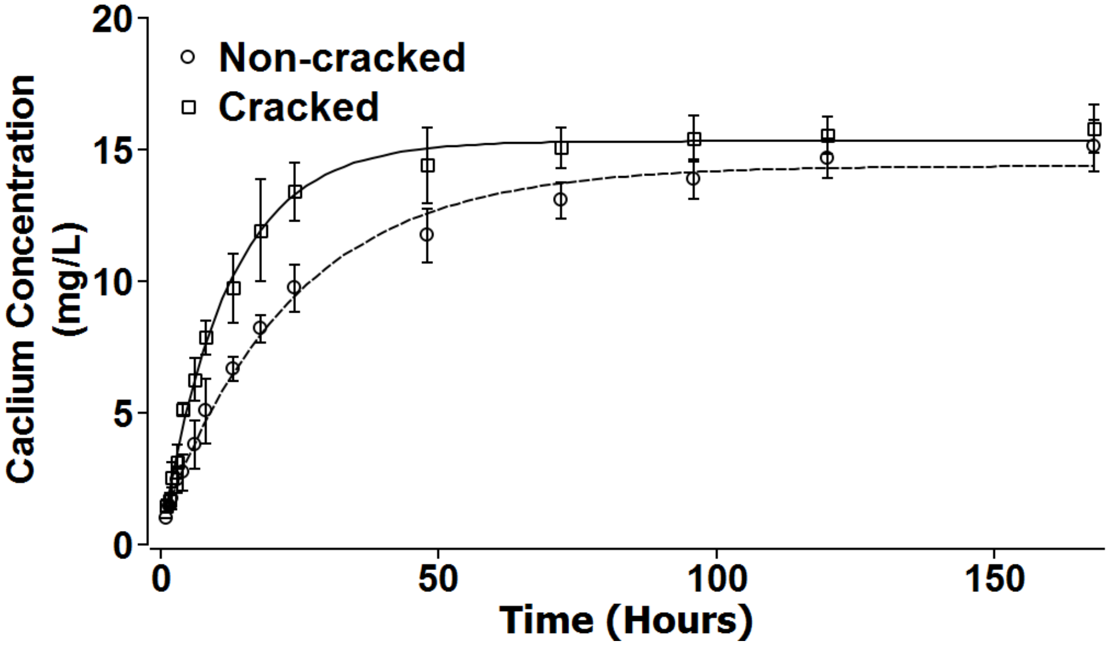

Figure 5.2 The calcium ion concentrations released from non-cracked (○) and cracked (□) HA specimens as a function of time. Error bars represent standard deviations. Both the non-cracked HA calcium release data and the cracked HA calcium release data were fit to equation (1), which yielded a coefficient of determination $R^2 = 0.994$ and $R^2 = 0.996$, respectively.

Figure 5.2 shows that the calcium ions released from both non-cracked HA (○) and cracked HA (□) increased exponentially with immersion time in distilled water. The data from both the non-cracked and the cracked HA specimens were fit to equation (1) via a least squares technique,

$$C = C_s - (C_s - C_0)\exp(-t/\tau) \tag{1}$$

where C is the calcium ion concentration released into distilled water from cracked HA, t is the immersing time, C_s corresponds to the plateau value of calcium concentration at $t \to \infty$, C_0 corresponds to the calcium concentration in distilled water at $t=0$, and τ is a time constant that inversely correlates to the changing rate of calcium ion concentration.

The least squares fit for non-cracked HA yields $C_s = 14.38 \pm 0.26$ mg/L, C_0-$C_s = -13.64 \pm 0.31$ mg/L (such that C_0 is approximately 0.74 mg/L), and $\tau = 23.74 \pm 0.003$ *hours*, with a coefficient of determination, R^2 of 0.994. The least squares fit of the cracked HA data yields $C_s = 15.32 \pm 0.18$ mg/L, C_0-$C_s = -15.11 \pm 0.30$ mg/L (such that C_0 is around 0.21 mg/L), and $\tau = 12.01 \pm 0.004$ *hours*, with a coefficient of determination, R^2 of 0.996.

From Figure 5.1, the concentration of calcium ions released from cracked HA becomes significantly higher than from non-cracked HA at four hours. The calcium release rate from the cracked HA surface is faster than that from non-cracked HA surfaces as indicated by the time constant τ, which is inversely correlated to the calcium ion release rate, such that the smaller the value of τ, the faster the release rate. For non-cracked HA, $\tau = 23.74 \pm 0.003$ *hours*, which is about twice the value for the time constant for the cracked HA, where $\tau = 12.01 \pm 0.004$ hours. Both the higher calcium concentration and the faster calcium release rate from the cracked HA surface shows that the dissolution of the HA surface was enhanced by the presence of microcracks and possibly the increase in surface area from pore dissolution.

Besides the changes in HA dissolution behavior, the introduction of Vickers indentations can also lead to surface area increases. This increased surface area resulting from Vickers indentation can be calculated using equation (2),

$$\Delta A \approx d^2/1.8544 - d^2/2 \tag{2}$$

where ΔA is the surface area increase, and d is the indentation diagonal [ASTM E384-11]. The surface increase from each indentation is thus In the current study, the indentation diagonal d is approximately 45 μm, and the increase in surface area from each indentation is calculated to be 79.5 μm^2. Keeping in mind that pore coalescence is a constant for both the cracked and the non-cracked HA, the total increase in surface area from the 7X7 indentation grid is thus approximately 3,894.6 μm^2 which when compared to the non-cracked surface (2.9 cm^2), represents only a 1.3×10^{-3}% increase.

Calcium ion signaling is known to control OB growth and differentiation [Zayzafoon 2006]. Accompanying the release of calcium ions, HA dissolution releases inorganic phosphate ions, which have also been found to signal OB differentiation [Beck 2003]. In our study, this increase in calcium ion concentration is associated with a negligible increase in overall surface area.

Therefore, the enhanced cell activity described previously can be said to result from the presence of the cracks (leading to enhanced Ca and likely P ion release) and not from the slight added surface area or surface features. To verify this hypothesis, future studies should examine OB attachment on microcracked (Vickers indented) and non-microcracked alumina specimens of comparable surface finish, density and grain size. Alumina should be used because any enhanced cell activity would only arise from the presence of the cracks and not from a chemical effect as alumina has been shown by multiple groups to be inert with respect to osteoblast activity [Malik et al. 1992, Marti 2000, Fischer et al. 2005].

CONCLUSION

Calcium ion release in distilled water from HA is increased by the presence of microcracks as shown by both a higher calcium concentration in the early hours and a faster calcium release rate when compared to non-cracked HA. It is likely that the observed enhanced OB response to microcracked specimens in the previous chapter is related in part to the calcium ion concentration changes in the microenvironment at the presence of the microcracks, and not to the negligible increase in surface area.

REFERENCES

REFERENCES

[ASTM E384-11] Standard test method for Knoop and Vickers hardness of materials.

[Beck 2003] Beck GR. Inorganic phosphate as a signaling molecule in osteoblast differentiation. J Cell Biochem 2003; 90: 234-243.

[Chang et al. 2000] Chang YL, Stanford CM, Keller JC. Calcium and phosphate supplementation promotes bone cell mineralization: Implications for hydroxyapatite (HA)-enhanced bone formation. J Biomed Mater Res 2000; 52: 270-278.

[Ducheyne et al. 1993] Ducheyne P, Radin S and King L. The effect of calcium phosphate ceramic composition and structure on *in vitro* behavior. I. Dissolusion. J Biomed Mater Res 1993; 27: 25-34.

[Fazan and Marquis 2000] Fazan F and Marquis PM. Dissolution behavior of plasma-sprayed hydroxyapatite coatings. J Mater Sci: Mater Med 2000; 11: 787-792.

[Fischer et al. 2005] Fischer H, Niedhart C, Kaltenborn N, Prange A, Marx R, Niethard, Rainer Telle. Bioactivation of inert alumina ceramics by hydroxylation. Biomaterials 2005; 26: 6151-6157.

[Han et al. 2001] Han Y, Xu K, Lu Jian. Dissolution response of hydroxyapatite coatings to residual stresses. J Biomed Mater Res 2001; 55: 596-602.

[Hollister et al. 2002] Hollister SJ, Maddox RD, Taboas JM. Optimal design and fabrication of scaffolds to mimic tissue properties and satisfy biological constraints. Biomaterials 2002; 23: 4095-4103.

[Karageorgiou and Kaplan 2005] Karageorgiou V and Kaplan D. Porosity of 3D biomaterial scaffolds and osteogenesis. Biomaterials 2005; 26: 5474-5491.

[LeGeros 2002] LeGeros RZ. Properties of osteoconductive biomaterials: Calclium phosphates. Clin Orthop Relat Res 2002; 395: 81-98.

[Li et al. 2009] Li D, Yang MX, Muralidhar P, Wu C, and Yang F. Local surface damage and material dissolution in 45S5 bioactive glass: effect of the contact deformation. J Non-Crystal Solids 2009; 355: 874-879.

[Malik et al. 1992] Malik MA, Puleo DA, Bizios R, Doremus RH. Osteoblasts on hydroxyapatite, alumina and bone surfaces *in vitro*, morphology during the first

2 h of attachment. Biomaterials 1992; 13: 123-128.

[Marti 2000] Marti A. Inert bioceramics (Al_2O_3, ZrO_2) for medical application. Injury Int J Care Injured 2000; 31: S-D33-36.

[Meleti et al. 2000] Meleti Z, Shapiro IM and Adams CS. Inorganic phosphate induces apoptosis of osteoblast-like cells in culture. Bone 2000; 27: 359-366.

[Morgan et al. 1996] Morgan J, Holtman KR, Keller JC, Stanford CM. *In vitro* mineralization and implant calcium phosphate-hydroxyapatite crystallinity. Implant Dentistry 1996; 5: 264-271.

[Mori et al. 2003] Mori K, Hara T, Mizugaki T, Ebitani K, and Kaneda K. Hydroxyapatite-bound cationic ruthenium complexes as novel heterogeneous lewis acid catalysts for diels-alder and aldol reactions. J Am Chem Soc 2003; 125: 11460-11461.

[Mori et al. 2004] Mori K, Hara T, Mizugaki T, Ebitani K, and Kaneda K. Hydroxyapatite-supported palladium nanoclusters: a highly active heterogeneous catalyst for selective oxidation of alcohols by use of molecular oxygen. J Am Chem Soc 2004; 126: 10657-10666.

[Nagai and Nishino 1988] Nagai M, Nishino T. A new type of CO2 gas sensor comprising porous hydroxyapatite ceramics. Sensor and Actuat 1988; 15: 145-151.

[Owada et al. 1989] Owada H, Yamashita K, Umegaki T, Kanazawa T. Humidity-sensitivity of yttrium substituted apatite ceramics. Solid State Ionics 1989; 35: 401-404.

[Raynaud et al. 1998] Raynaud S, Champion E, Bernache D. Dynamic fatigue and degradation in solution of hydroxyapatite ceramics. J Mater Sci Mater Med 1998; 9:221–227.

[Reis et al. 1994] Reis RL, Monterio FJ, Hastings GW. Stability of hydroxyapatite plasma-sprayed coated Ti-6Al-4V under cyclic bending in simulated physiological solutions. J Mater Sci Mater Med 1994; 5:457–462.

[Venugopal and Scurrell 2003] Venugopal A, Scurrell MS. Hydroxyapatite as a novel support for gold and ruthenium catalysts: Behavior in the water gas shift reaction. Appl Catal A: Gen 2003; 245: 137-147.

[Wei and Ma 2004] Wei GB, Ma PX. Structure and properties of nano-hydroxyapatite/polymer composite scaffolds for bone tissue engineering.

Biomaterials 2004; 25: 4749-4757.

[Wetzel et al. 1995] Wetzell AC, Stich H, Caffesse RG. Bone apposition onto oral implants in the sinus area filled with different grafting materials-a histological study in beagle dogs. Clin Oral Implan Res 1995; 6: 155-163.

[Yang et al. 2004] Yang H, Curinga G, Giachelli CM. Elevated extracellular calcium levels induce smooth muscle cell matrix mineralization *in vitro*. Kidney Int 2004; 66: 2293-2299.

[Yoshikawa et al. 2000] Yoshikawa T, Ohgushi H, Nakajima H, Yamada E, Ichijima K, Tamai S, Ohta T. *In vivo* osteogenic durability of cultured bone in porous ceramics-A novel method for autogenous bone graft substitution. Transplantation 2000; 69: 128-134.

[Zayzafoon 2006] Zayzafoon M. Calcium/calmodulin signaling controls osteoblast growth and differentiation. J Cell Biochem 2006; 97: 56-70.

[Zhang et al. 2003] Zhang Q, Chen J, Feng J, Cao Y, Deng C and Zhang X. Dissolution and mineralization behavior of HA coatings. Biomaterials 2003; 24: 4741-4748.

CHAPTER 6

CALCIUM PHOSPHATE PRECIPITATION ON HYDROXYAPATE IN THE ABSENCE OF CELL CULTURE

INTRODUCTION

In chapter 4, mineral deposition on both non-cracked and cracked HA was observed after cell culturing for 21 days. However, since the dissolution of HA and the release of calcium ions were observed in the previous chapter and calcium phosphate crystals can grow on HA surface [Nancollas and Tomazic 1974], one may wonder how the mineral nodules may form in the absence of bone forming cell. In other words, it is necessary to find out how the calcium phosphate precipitation would occur on hydroxyapatite surfaces in the absence of cells. Thus, in order to compare with mineral deposition by the cells observed at 21 days in chapter 4, a parallel study was done on non-cracked and cracked HA surfaces in the absence of cells.

MATERIALS AND METHODS

Non-cracked (control) and cracked HA (experiment) specimens are prepared as described in previous chapters. Both control and experiment groups were pulsed with 20 μM Xylenol Orange [Stuart and Smith 1992] in differential media. The time interval and duration of the Xylenol orange pulse are the same as described in Chapter 4. In the presence of OB culture (Chapter 4), Xylenol orange was pulsed every other day starting from day four (cells reach confluency and start differentiation), ended on day 20 and were imaged on day 21. In this parallel study, we did not have to wait until day four since no cells were present. However, the amount of fluorescent Xylenol orange stain should still be consistent with what had been used in Chapter 4. The Xylenol orange was thus pulsed every other day starting on day one until day 17 and calcium deposition was imaged on day 18.

RESULTS AND DISCUSSION

Figure 6.1 shows the CLSM micrographs of calcium deposition on non-cracked (Figure 6.1a) and cracked (Figure 6.1b) HA surfaces. The orange dots represent the free calcium that has re-deposited onto the substrate surfaces

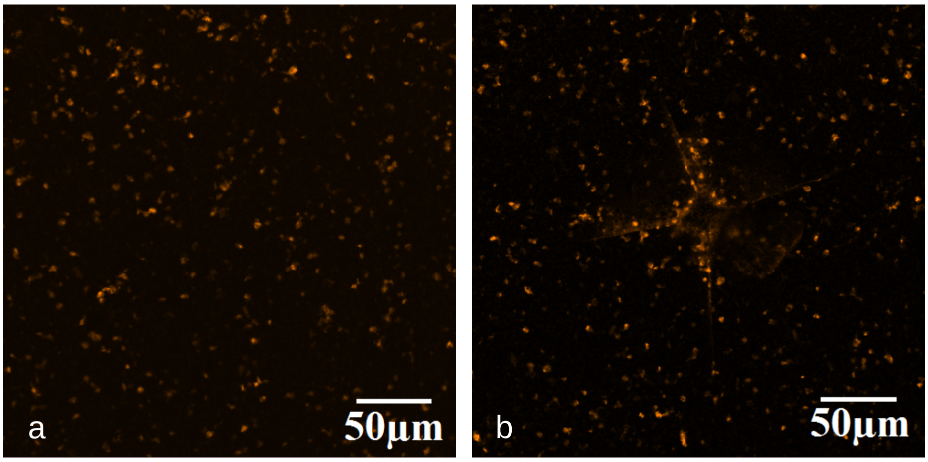

Figure 6.1 CLSM Z-stack maximum fluorescence intensity projections of calcium depositions on (a) non-cracked and (b) cracked HA in the absence of cell culture. The OBs were pulsed with Xylenol Orange every other day during culturing since day four. The Xylenol Orange fluorescence stain was excited at 543 nm and emission was detected through a BA560-620 emission filter (represented in orange).

Figure 6.1 shows that even in the absence of osteoblasts, calcium phosphate can precipitate from the HA surfaces. Moreover, comparing to non-cracked HA surface (Figure 6.1a), the radial cracks and edges of indentation impression on the cracked HA surface (Figure 6.1b) are outlined by more orange dots which correspond to more calcium precipitaion localized at the radial cracks and indentation edges based on a qualitative observation. The vicinity of indentation on cracked HA surface shows similar calcium deposition as non-cracked HA surface.

However, the localized calcium precipitation in the absence of OBs (Figure 6.1b) is different from the localized mineral deposition by the OBs (Figure 4.14b). In Figure 6.1b, where no cells were involved, the orange dots were concentrated at radial cracks and indentation edges, but none in the indentation center. In Figure 4.14b, where cells were involved, the concentrated orange dots were filling in the indentation impression rather than lying along the radial cracks or indentation edges.

In the absence of cells (Figure 6.1b), calcium precipitation is correlated with the active surface features such as radial cracks and edges. In the case of OB culture (Figure 4.14b), however, calcium deposition depends on the cellular matrix secreted by the bone forming cells [Hessel et al. 2002].

The reason why no calcium precipitation was observed along the radial cracks at the presence of cells can be explained by considering the relative size of radial cracks and the bone forming cells. The radial crack opening is a few nanometers [Burghard et al. 2004] and thus likely to be covered by the osteoblasts (10 ~ 20 µm) and secreted extracellular matrix in the early attachment and proliferation stages. Since the fluorescent Xylenol orange was only applied upon cell confluence, it is likely that the mineralized cellular matrix rather than the free HA surface was stained. Different from the radial cracks, the indentation impression is about 45 µm, which serves as a natural concave well for the OBs. The ECM secreted by the “trapped” cells could have altered conformation comparing to the cellular matrix on the flat surface. The possible alteration in ECM matrix may in turn lead to the localized mineralization in the indentation impression observed in Figure 4.14b.

CONCLUSIONS

In this study, calcium phosphate precipitation on the HA surfaces were observed in the absence of osteoblasts. Moreover, the radial cracks and the edges of the indentation impression on the cracked HA surface showed more active calcium precipitation as compared to the non-cracked regions.

Different from the observed calcium phosphate deposition along the cracks and indentation edges, the matrix mineralization in the presence of cells in Chapter 4 was localized in the indentation impression. This observed difference is likely due to the relative sizes of radial crack opening, the osteoblast cells, and the indentation impression. In the absence of cells, the calcium precipitation from the free HA surface was stained; while at the presence of cells, the calcium precipitation from the HA surface was overwhelmed by the mineralization of the cellular matrix.

The CLSM imaging method used in this chapter did not provide a quantitative measurement of calcium ion concentration as measured using

AAS in the previous chapter. However, it could potentially be used to identify localized calcium precipitation from the cell-free cracked HA surface at early times.

REFERENCES

REFERENCES

[Burghard et al. 2004] Burghard Z, Zimmermann A, Rodel J, Aldinger F and Lawn BR. Crack opening profiles of indentation cracks in normal and anomalous glasses. Acta Materialia 2004; 52: 293-297.

[Hessel et al. 2002] Hessle L, Johnson KA, Anderson HC, Narisawa S, Sali A, and Goding JW et al. Tissue-nonspecific alkaline phosphatase and plasma cell membrane glycoprotein-1 are central antagonistic regulators of bone mineralization. Proceed National Acad Sci 2002; 99: 9445-9449.

[Nancollas and Tomazic 1974] Nancollas GH and Tomazic B. Growth of calcium phosphate on hydroxyapatite crystals, effect of supersaturation and ionic medium. J Phys Chem 1974; 78: 2218–2225.

[Stuart and Smith 1992] Stuart AJ and Smith DA. Use of the fluorochromes Xylenol orange, calcium green, and tetracycline to document bone deposition and remodeling in healing fractures in chickens. Avian Disease 1992; 36: 447-449.

CHAPTER 7

OSTEOBLAST SPATIAL DISTRIBUTION AFTER 1, 2 AND 4 HOURS ATTACHMENT

In this chapter, osteoblast distribution on non-cracked and cracked HA were discussed and compared. The distribution data were collected from fluorescent micrographs. The micrographs of cracked HA were taken in a way such that the indentations were located in the center of the image in order to include cells from all directions. A polar coordinate system was set up on each micrograph by choosing the indentation center as the origin and an arbitrary half radial crack direction as the 0º axis as shown schematically in Figure 7.1. The cell location is depicted by the blue nucleus and characterized by the radial distance r and angle α (Figure 7.1).

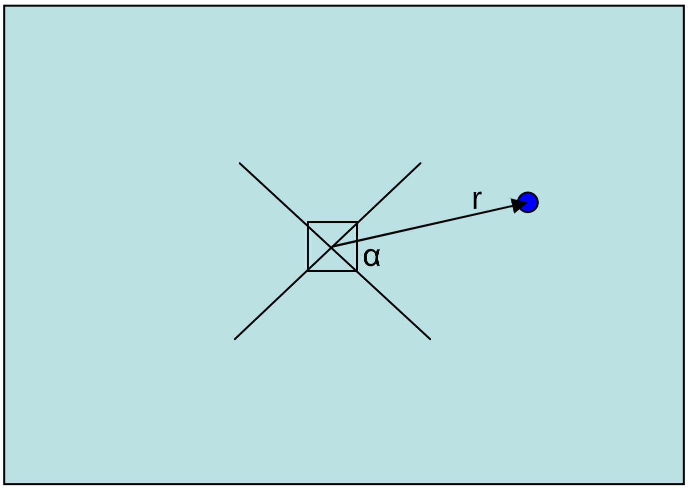

Figure 7.1 Schematic of the measurement of osteoblast location with respect to the indentation region on a cracked HA micrograph. The cell location is characterized by the radial distance from indentation center, r and angle α.

The distribution of cells on non-cracked HA surfaces was also examined in the same way. Since no indentations were made on non-cracked HA, the origin was chosen as the center of the micrograph, which allows the measurement of cells in all directions.

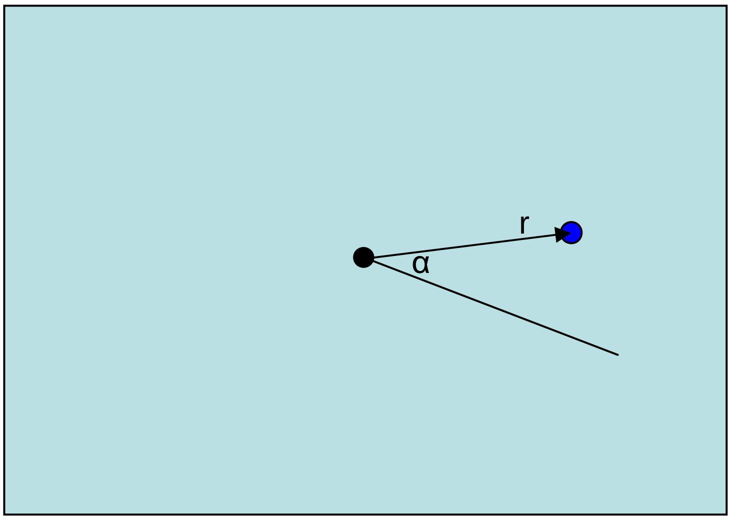

Figure 7.2 Schematic of the measurement of osteoblast location with respect to the indentation region on a non-cracked HA micrograph. The cell location is characterized by the radial distance from indentation center, r and angle α.

The cells on both non-cracked and cracked HA specimens were imaged after 1, 2 and 4 hours attachment. In order to have a large enough cell population for a statistical cell distribution analysis, data from 90 images were pooled together. The data pooling is valid considering that both cell and cell culture conditions were well controlled and specimen surfaces properties are comparable.

The cell distribution was considered in a polar coordinate system, where the indentation center (cracked) or image center (non-cracked) was chosen as the origin and the arbitrary indentation diagonal as the 0° axis. If the cells are randomly distributed about the origin, the radial distribution and angular distribution should fit with Rayleigh and Uniform distribution, respectively [Kuruoglu et al. 2004].

Equation (1) gives the probability density function of one-parameter Rayleigh distribution:

$$f(r;\sigma) = \frac{r}{\sigma^2}\exp(-\frac{1}{2}(\frac{r}{\sigma})^2),\ (r\quad 0) \qquad (1)$$

where r is the distance from origin, and σ is a continuous scale parameter [EasyFit]. The probability density function of Uniform distribution is:

$$f(\alpha) = \frac{1}{(b-a)}, a < \alpha < b \qquad (2)$$

where θ is the angle from the polar coordinates [EasyFit].

Figure 7.3 shows the radial distance and angular distribution for cell on non-cracked HA at 1, 2, and 4 hours. The radial distance distributions were fit to Rayleigh distribution model (equation 1) and the angular distributions were fit to uniform model (equation 2). The goodness of fitting for cell distributions on non-cracked HA is listed in Table 7.1.

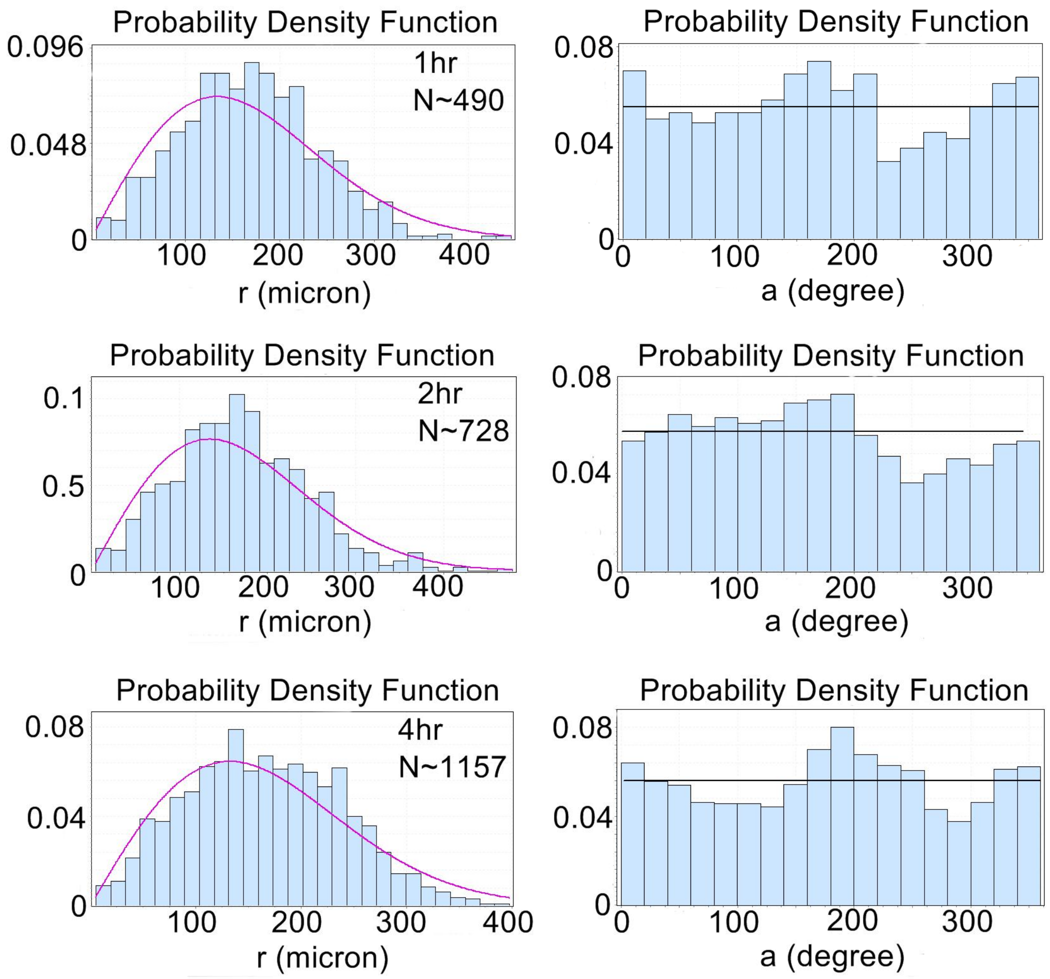

Figure 7.3 The radial distance, r distributions (left column) and the angle, α distributions (right column) after 1 (first row), 2 (second row) and 4 hours (third row) of attachment on non-cracked HA. The r distributions were fit to Rayleigh distribution (mauve solid line), and the α distributions were fit to Uniform distribution (black solid line) using EasyFit. The radial distance r distributions did not fit to Rayleigh distribution at all hours (p<0.01), while the angle α distributions were uniform at all hours.

Table 7.1 Goodness of fitting tests for cell distribution data on non-cracked HA

α=0.01	Radial distance data fit to Rayleigh distribution	Angle data fit to Uniform distribution
Goodness of fitting test	Chi-Square	Kolmogorov-Smirnov
1 hour	p=2.1130E-7	Fit
2 hour	p=4.6263E-8	Fit
4 hour	p=4.4409E-16	Fit

Figure 7.4 shows the radial distance and angular distribution for cell on

cracked HA at 1, 2 and 4 hours. The radial distance distributions were fit to Rayleigh distribution model (equation 1) and the angular distributions were fit to uniform model (equation 2). The goodness of fitting for cell distributions on cracked HA is listed in Table 2.

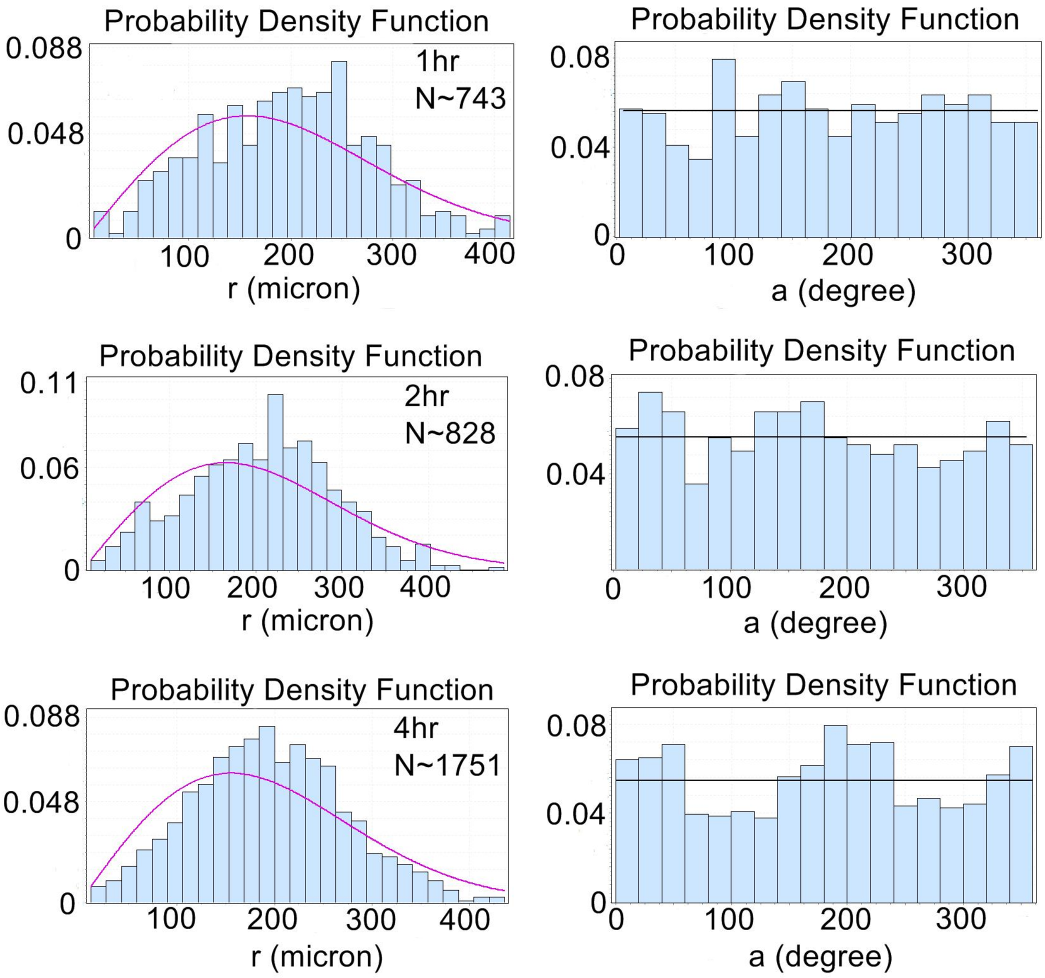

Figure 7.4 The radial distance, r distributions (left column) and the angle, α distributions (right column) after 1 (first row), 2 (second row) and 4 hours (third row) of attachment on cracked HA. The r distributions were fit to Rayleigh distribution (mauve solid line), and the α distributions were fit to Uniform distribution (black solid line) using EasyFit. The radial distance r distributions did not fit to Rayleigh distribution at all hours ($p<0.01$), while the angle α distributions were uniform all hours.

Table 7.2 Goodness of fitting tests for cell distribution data on cracked HA

α=0.01	Radial distance fit to Rayleigh distribution	Angle fit to Uniform distribution
Goodness of fitting test	Chi-Square	Kolmogorov-Smirnov
1 hour	p=3.9891E-8	Fit
2 hour	p=6.6613E-16	Fit
4 hour	p=0	Fit

The spatial distribution for cells on both non-cracked and cracked HA showed uniform angular distribution. However, the radial distance distributions disagreed with the Rayleigh distribution, which showed that the cells were not randomly distributed on the HA surface. It is reasonable since cells are not isolated from each other but could communicate with each other through membrane proteins such as integrin and cadherin [Anselm 2000].

A closer examination of the p value from the Chi-square tests for Rayleigh distribution showed two trends: first, for both control and experimental groups, the p value decreases with increasing time, which indicates that the deviation of cell distribution from random distribution increases with time; second, at a given time, the p value obtained from cracked HA data is at least one magnitude smaller than the p value from non-cracked HA data, which indicates that cell distribution on cracked HA is more deviated from random distribution comparing to cells on non-cracked HA.

REFERENCES

REFERENCES

[Anselme 2000] Anselme K. Osteoblast adhesion on biomaterials. Biomaterials 2000; 21-667-681.

[Kuruoglu and Zerubia 2004] Kuruoglu EE and Zerubia J. Modeling SAR images with a generalization of the Rayleigh distribution. IEEE Trans Image Proc 2004; 13: 527-533.

CHAPTER 8

SLOW GROWTH OF MICROCRACKS IN HYDROXYAPATITE DURING AGING

ABSTRACT

Hydroxyapatite ($Ca_{10}(PO_4)_6(OH)_2$ or HA) is a brittle material that is subject to environmentally assisted slow crack growth. While most slow crack growth studies are carried out after aging, this study examines the slow growth of radial cracks induced by Vickers indentation in dense HA (94% of theoretical density) during aging in ambient air, where the observed crack growth is consistent with a process in which residual stress drives crack growth. For indentation loads of 0.98 N, 1.96 N, 2.94 N, and 4.91 N, the average radial crack length increased exponentially with time for indentation loads of 0.98 N, 1.96 N, 2.94 N, and 4.91 N, with crack lengths saturating within one hour following indentation. However, no radial crack growth was observed for 9.81 N loads. The load dependence of radial crack growth is proposed to be linked to the partitioning of residual strain energy by the lateral crack growth, which has not been reported in the literature.

INTRODUCTION AND BACKGROUND

Hydroxyapatite ($Ca_{10}(PO_4)_6(OH)_2$ or HA) has been widely applied as a catalytic substrate [Mori et al. 2003 and 2004, Venugopal and Scurrell 2003], CO_2 gas and humidity sensors [Nagai and Nishino 1988, Owada et al. 1989], insulating materials for electric circuits, dielectric layers for microwave applications [Hontsu et al. 1997], substrates for heavy metal removal [Silva et al. 2006, Raicevic et al. 2005], and for hard biological tissue replacement [Park and Lakes 2007]. During the in-service lifetime, fabrication and handling of brittle materials, both residual stresses and cracks can be introduced by structural mismatch, thermal expansion anisotropy, as well as by interactions among contacting parts [Withers and Bhadshia 2001]. Slow crack growth may lead to catastrophic failure, which in turn limits a component's useful life [Michalske and Freiman 1983, Connally and Brown 1992, Tomozawa 1996, West and Hench 1998].

Slow crack growth behavior in HA and other brittle ceramics is usually described in terms of a V-K_I relationship where V refers to the crack velocity and K_I, the mode I stress intensity factor (equation 1) [Wiederhorn 1974].

$$V = AK_I^n \tag{1}$$

where A is a constant and n is a propagation exponent which characterizes the material's resistance to mechanical fatigue. For HA, the n value is lower than 30, and thus is considered as materials with high susceptibility to slow crack growth [Choi et al. 2006]. Both indirect static/dynamic fatigue tests [Raynaud et al. 1998, Barinov et al. 2003, Schell et al. 2010] and direct measurements of crack velocity via double torsion tests [Benaqqa et al. 2004 and 2005] have been used to explore the V-K_I behavior of brittle materials. The slow crack growth exponent, n, obtained from either indirect or direct methods, describes a materials' resistance to delayed mechanical fatigue [Wiederhorn 1974]. For HA, the n value is lower than 30, and is considered as materials with high susceptibility to slow crack growth [Choi et al. 2006].

The relative ease in controlling the load, loading time, and indentation location has led to Vickers indentation cracks as crack growth models for studies of slow crack growth [Dwivedi and Green 1995, Salomonson et al. 1996], thermal shock/thermal fatigue [Anderson and Rowcliffe 1996, Lee et al. 2002], thermally-induced crack healing [Chlup et al. 2008, Wilson and Case 1997 and 1999], cracking/delamination in coatings [Galmen et al. 1991, Ibrahim et al. 2007], contact flaws introduced during processing or handling of brittle materials [Lawn and Wilshaw 1975, Lawn et al. 1993], and *in vitro* cell responses to microcracks in bioceramics [Smith 2007, Shu submitted 2011].

In general, during Vickers indentation, the residual stress from plastic deformation left upon unloading is responsible for the development of both the radial and the lateral crack systems [Lawn et al. 1980, Marshall et al. 1982]. The detailed role of residual stresses in crack formation and propagation during Vickers indentation is described in Appendix A of this chapter. The relationship between equilibrium radial crack length c^R and the maximum indentation load, *F,* is described by equation (2),

$$c^{R} = \left\{ \S_{r}^{R} (\cot\psi)^{2/3}[(E/H)^{1/2}/K_{C}] \right\}^{2/3} F^{2/3} \qquad (2)$$

where $\S_r^R$ is a dimensionless constant independent of indenter and specimen ($\S_r^R$ =0.032), ψ (68°) is the half angle for Vickers indenter tip, the Young’s modulus, *E*, hardness, *H*, and fracture toughness, K_C can all be considered invariant for a system at equilibrium with its surroundings [Lawn et al. 1980]. A similar relationship between equilibrium lateral crack length c^L and the maximum indentation load, *F*, is described by equation (3),

$$c^{L} = \left\{ (\zeta_{L}/G^{1/2})(\cot\psi)^{5/6}[(E/H)^{3/4}/K_{c}H^{1/4}] \right\}^{1/2} F^{5/8} \qquad (3)$$

where ζ_L is a dimensionless constant independent of indenter and specimen (ζ_L =0.025)**,** *G* is a dimensionless geometrical constant and has a value of 3/4 when the lateral crack length is less than the radial crack length (quarter plate) [Marshall et al. 1982].

Radial cracks received most attention as model cracks, and the crack velocities are typically measured after the release of residual stresses via the aging process [Ritter et al. 1971, Marshall and Lawn 1980, Chantikul et al. 1981]. However, the literature does not address crack growth behavior during the aging process.

This study focuses on slow crack growth during aging in ambient air for Vickers indentation induced radial cracks in 94% dense HA. Radial crack lengths were measured after indentation and during room temperature aging in air at loads of 0.98 N to 9.81 N. The occurrence and relative size of lateral cracks at all loads are also evaluated to assess the perturbation from lateral cracks during the slow growth of radial cracks.

EXPERIMENTAL PROCEDURE

Materials and characterization methods

HA powders (Taihei Chemical Industry, Osaka, Japan) with vendor-specified particle size of 4 to 6 µm were uniaxially pressed at 27.65 MPa for one minute in a 32 mm diameter steel pellet die. The specimens were then sintered in an electrical resistance furnace (CM Inc., Model #0100277, Bloomfield, NJ) at 1360^{o}C for 4 hours in air at a ramp rate of 10^{o}C per minute during both heating and cooling. The sintered specimens were polished using diamond paste of grit size down to 0.5 µm before microindentation.

Specimen mass and dimensions were measured using an electronic analytical balance (Denver Instrument Company, Arvada, CO; accuracy, ±0.001 gram) and an electronic digital caliper (Davis Calibration, Carol Stream, IL; accuracy, ±0.01 mm) respectively. Bulk densities were calculated from the mass and dimension measurements.

One polished specimen was thermally etched in air at 1360^{o}C for 1 hour in the same furnace used for sintering the indented specimens. Following thermal etching, the specimen was coated with a 21 nm thick film of Au using a gold sputter coater (EMSSCOPE SC500, Ashford, Kent, Great Britain). The microstructure (grain size and porosity) was examined using a scanning electron microscope (JEOL-6400V SEM, JEOL Ltd., Japan) using an accelerating voltage of 20 kV and a working distance of 39 mm.

For chemical and phase composition characterization, X-ray diffraction (XRD) analysis was performed on both the as-received HA powders and pulverized powder from sintered HA specimens, as described in detail in Chapter 4.

Vickers indentation and crack length measurement.

Radial and lateral cracks on polished surfaces were introduced by Vickers indentations in ambient air using Shimadzu microhardness tester (HMV2000, Kyoto, Japan) at five loads (0.98 N, 1.96 N, 2.94 N, 4.91 N and 9.81 N). For each load, a total of 15 indentations were made with a loading time of 5 seconds. The hardness, H, and fracture toughness, K_C, of HA specimens included in this study were determined from the measurements of indentation diagonal and initial radial crack length.

The indentation impression centers were placed at least five times of the radial crack length ($2c^R$) apart to minimize possible interactions between adjacent radial cracks. The radial crack lengths ($2c^R$) were measured at approximately fifteen minute intervals during the first, third, and fifth hours following indentation, using an optical microscope mounted on the Shimadzu microhardness tester. The lateral cracks lengths (c^L) visible on the polished specimen surfaces were measured in the same way as the radial cracks.

RESULTS AND DISCUSSION

Material characterization

The sintered HA specimens reached an average of 94% of theoretical density (3.16 g/cm^3) [Anthony et al. 2000]. The average grain size of sintered HA specimen is approximately 7.9 µm as determined by linear intercept method (a total of 210 intercepts) on micrographs of polished specimen surfaces using a stereographic projection factor of 1.5 (Figure 8.1a) [Fulrath and Pask et al. 1968]. The polished HA surfaces has uniformly distributed spherical or quasi-spherical isolated pores with diameters ~3 µm (Figure 8.1b). From a previous study [Shu submitted 2011], the XRD analysis of as-received HA powder and pulverized sintered HA specimen showed only the crystalline HA phase was present (JCPDS 9-432, Joint Committee on Powder Diffraction Standards, Swarthmore, PA).

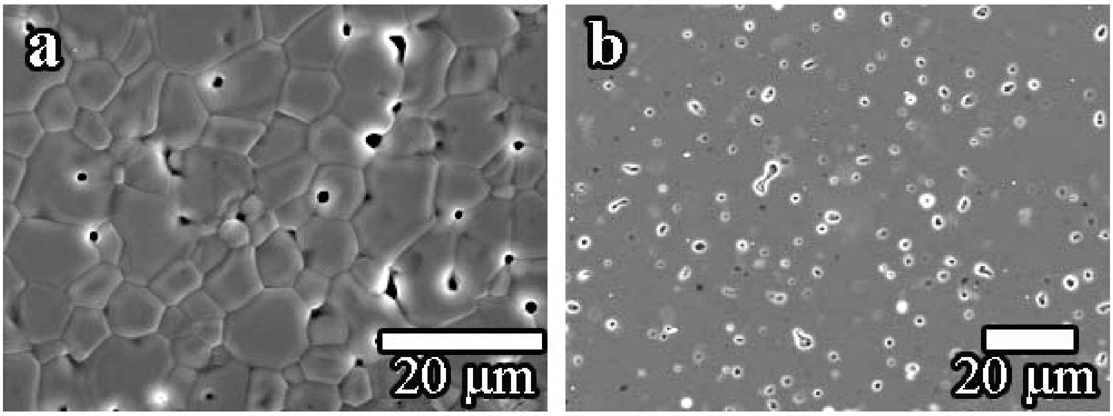

Figure 8.1 SEM images of (a) a thermally etched surface of a 94.3% dense HA specimen, where the average grain size calculated using line intercept method (a total of 210 intercepts) was 7.9 µm and (b) a polished surface of a 95.4% dense HA specimen, where uniformly distributed spherical or quasi spherical pores with a few interconnected or entrapped pores were observed. The diameters of the surface-breaking pores are less than 3 µm.

***E, H,* and *K_c* for HA specimens**

The porosity dependence of Young's modulus, E, can be described by equation (4),

$$E = E_0 \, exp(-b_E P) \tag{4}$$

where E_0 is the Young's modulus for theoretically dense specimen, b_E is a dimensionless material-dependent constant, and P is porosity [Spriggs 1961]. In Fan et al.[submitted 2011] and Ren et al.'s [2009] studies of HA with porosity ranging from 0.05 to 0.62, the Young's modulus data measured at different porosity, a least-squares fit to equation (4) yielded E_0 = 133.3 GPa, b_E = 3.8 and a coefficient of determination, R^2=0.974. Using equation (4) and E_0 and b_E values from Fan and Ren et al.'s studies yields E = 106.1 GPa for the HA specimens (P = 0.06) included in this study.

The Vickers hardness was calculated using equation (5) [ASTM C 1327-03],

$$H = 1.8544F/d^2 \tag{5}$$

where F is the maximum indentation load and d is the Vickers indentation diagonal. The average H of HA specimens used in this study was 4.50 ± 0.19 GPa.

The hardness of ceramics is also a function of porosity as described by equation (6),

$$H = H_0 \, exp(-b_H P) \tag{6}$$

where H_0 is the hardness for theoretically dense specimen, b_H is a dimensionless constant dependent on material properties, and P is porosity [Rice 1996]. The hardness values calculated from Hoepfner's and Dey's data using equation (6) are 4.17 GPa and 4.16 GPa respectively, which are similar to the H=4.50 ± 0.19 GPa for HA in this study.

The fracture toughness was obtained from equation (7) [Lawn et al. 1980, Antis et al. 2006],

$$K_C = \delta(\frac{H}{E})^{-1/2} \frac{F}{c_0^R} \tag{7}$$

where the empirically determined constant δ = 0.016, independent of material properties. F is the maximum indentation load and c_0^R is the initial half radial crack length. Using equation (7), and E = 106.1 GPa and H = 4.50 ± 0.19 GPa (as described above) yielded the average K_C = 0.484 ± 0.26 MPa·m$^{1/2}$ for HA specimens in this study. The K_C of HA coatings (P = 0.11) measured by Dey *et al.* was approximately 0.6 MPa·m$^{1/2}$, which is slightly higher than the K_C of bulk HA specimens in this study [Dea and Mukhopadhyay 2011].

Load dependence of initial radial and lateral crack lengths

The average of 30 initial radial crack lengths at each of the loads (0.98 N, 1.96 N, 2.94 N, 4.91 N and 9.81 N) was fit via a least-squares technique to equation (8) (Figure 8.2a) which is a simplified form of equation (2),

$$l_0 = B^R F^{2/3} \tag{8}$$

where l_0 is the average initial radial crack length ($l_0 = 2c_0^R$), B^R is a constant that depends on material properties, and F is the indentation load (Figure 8.2a) [Lawn et al. 1980]. The initial radial crack length, l_0, increases when the load, F, increases as described by equation (8), where a value of B^R = 65.2 ± 1.1 μm·N$^{-2/3}$ was obtained by the least squares fit, with the coefficient of determination, $R^2 = 0.997$.

The constant B^R in equation (8), which depends on materials properties, can also be calculated from the knowledge of E, H, and K_C determined for HA specimens used in this study (section 4.2). The calculated B^R value is approximately 62.3 μm·N$^{-2/3}$, which is a factor of 0.04 lower than the value of 65.2 ± 1.1 μm·N$^{-2/3}$ obtained for B^R from the least square fitting of initial radial crack length versus indentation load data to equation (8). The measurement of radial crack length thus yielded a constant that was close to the constant determined by the material properties (E, H, and K_C).

Similarly, the initial lateral crack lengths measured at all loads (0.98 N, 1.96 N, 2.94 N, 4.91 N and 9.81 N) were least-squares fit to equation (9) (Figure 8.2b) which is a simplified form of equation (3),

$$c_0^L = B^L F^{5/8} \tag{9}$$

where c_0^L is the average initial lateral crack length, B^L is a constant depending on material properties and indenter geometry when referring to equation (3) such that

$B^L = \{(\zeta_L / G^{1/2})(\cot\psi)^{5/6}[(E/H)^{3/4} / K_c H^{1/4}]\}^{1/2}$, *F* is the indentation load (Figure 8.2b) [Marshall et al. 1982]. The initial lateral crack length, c_0^L increases when the load, *F*, increases as described by equation (9), where a value of B^L = 24.9 ± 0.6 μm·N$^{-5/8}$ was obtained by the least squares fit, with the coefficient of determination, R^2 = 0.998.

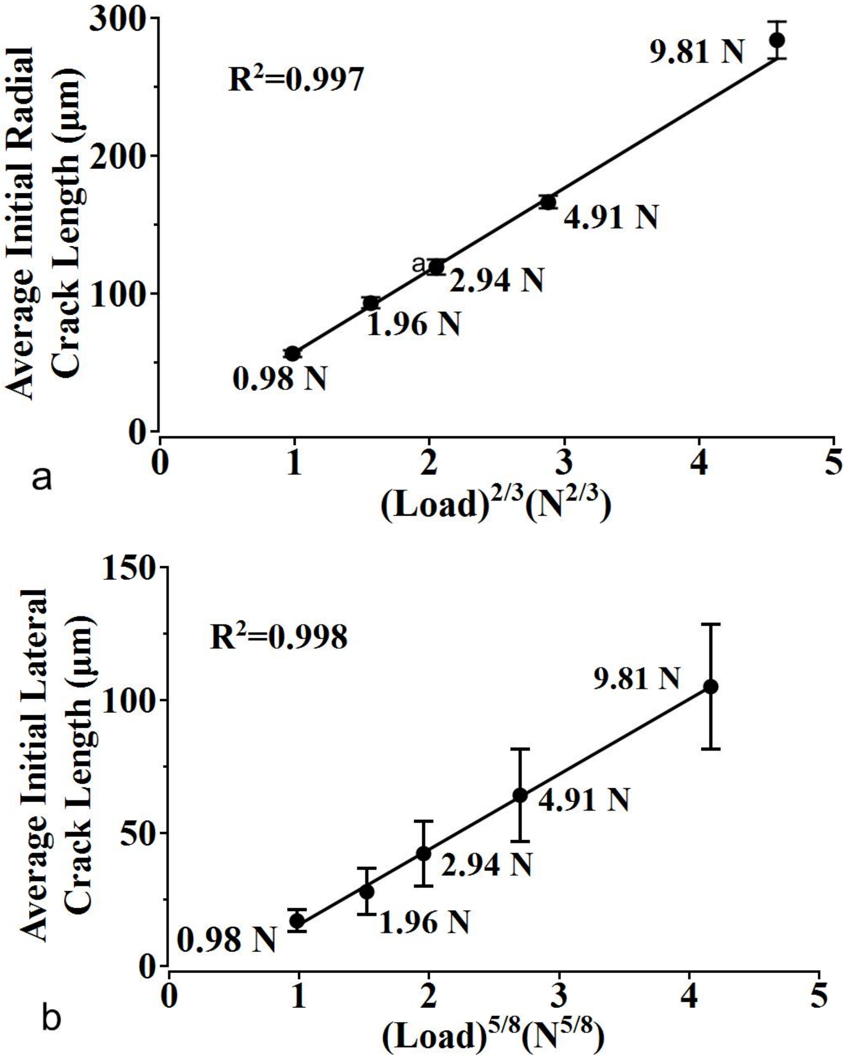

Figure 8.2 (a) The average initial radial crack length as a function of Vickers indentation loads. The error bars represent the standard deviations. The collected data were fit to equation (8). The coefficient of determination R^2 is 0.997. (b) The average initial lateral crack length as a function of Vickers indentation loads. The error bars represent the standard deviations. The collected data were fit to equation (9). The coefficient of determination R^2 is 0.998.

Using the E, *H,* and K_c values for the HA specimens used in this study, the B^L value is calculated to be 8.8 μm·$N^{-5/8}$, which is a factor of 0.65 lower than the value of for B^L obtained from the least square fitting of the initial lateral crack length versus indentation loads data to equation (9). In contrast to radial cracks (section 4.3.1), the measurement of lateral crack length yielded a constant that largely deviated from the constant determined by materials properties (E, H, and K_c).

Up to this point only the load dependence of initial radial and lateral crack lengths was considered. The cracks evolve with time and the evolution as well as the final stage of both radial/lateral crack systems will now be considered, since in choosing model crack, one must consider not only the crack initiation itself but rather the temporal development of the crack during aging in specific environments, such as ambient air or aqueous environment [Dwivedi and Green 1995, Salomonson et al. 1996]. In the following section, the slow growth of radial cracks and the perturbation from lateral cracks during aging in ambient air at room temperature are discussed.

Radial crack growth and perturbation from lateral cracks during aging

Load dependent exponential growth of radial cracks

The radial crack lengths, l, increased significantly within the first hour following indentation and reached a plateau for indentation loads at 0.98 N, 1.96 N, 2.94 N, and 4.91 N (Figure 8.3). The physical radial crack growth process, for the release of residual strain energy after Vickers indentation (Chapter 8 - Appendix A) resembles the evolution processes of many physical systems. In those systems, there is a physical quantity that decreases exponentially with time, such as the electric charge in the case of capacitor discharging, number of particles in the case of radioactive decay [Halliday et al. 1997], thermal energy in the case of Newtonian free cooling [Burmeister 1993], or the vibrational energy in the case of internal friction damping in solids [Reed-Hill 2009]. For the four physical systems listed above, the evolution of all physical quantities is such that the time rate change of each physical quantity is a linear function of the physical quantity itself. If we relate this to our current observation with radial cracks, we may consider the growth rate of radial cracks as a linear function of the radial crack length.

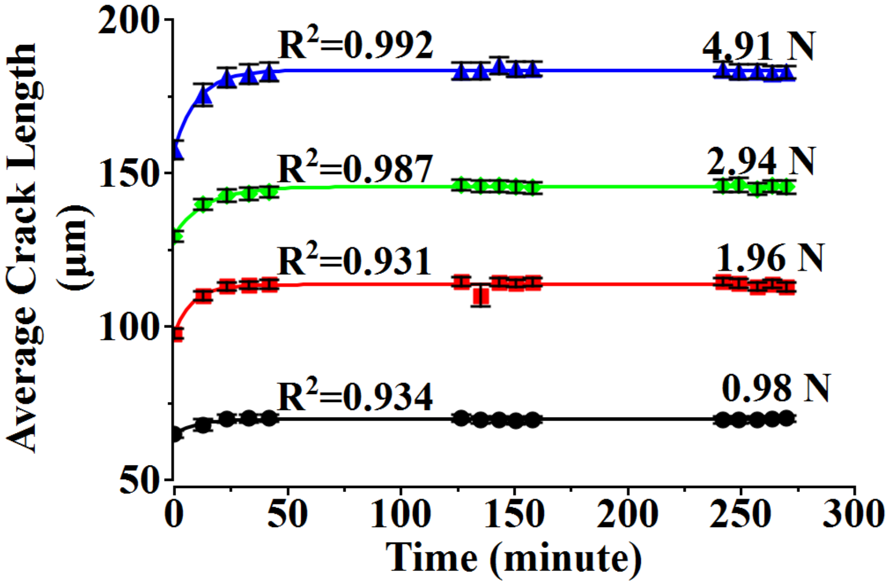

Figure 8.3 The average radial crack length as a function of time, normalized with respect to the initial radial crack length at each load. The normalized values were then plotted versus time with a common unit value at time zero. The error bars represent the standard deviation. The collected data were fit to equation (11). The coefficient of determination R^2 for the 0.98 N, 1.96 N, 2.94 N, and 4.91 N loads were 0.934, 0.931, 0.987, and 0.992, respectively.

When the time rate of change of a dependent variable, $\dot{y}$, is linear with respect to its value, *y*, the time dependence of *y* is described by equation (10)

[Apostol 1962].

$$\dot{y}(t) = Cy(t) + D \tag{10}$$

where C (nonzero) and D are constants.

If we apply equation (10) to the slow radial crack growth problem (Figure 8.3), the variable y is replaced by radial crack length, l ($l=2c^R$). The boundary conditions are $l=l_0$ at $t=0$, and $l=l_S$ at $t\to\infty$, where l_0 and l_S are the initial and saturated (steady state) crack length respectively. In this case l_0 is obtained by direct measurement of the initial radial crack length (Figure 8.2a) and l_S is determined from the plot of radial crack length versus time (Figure 8.3). Applying the boundary conditions, the solution of equation (10) yields an exponential relationship between l and t, as given by equation (11).

$$l = l_s - (l_s - l_0)\exp(-t/\tau) \tag{11}$$

where τ is a time constant that is inversely related to the time rate of change of crack length, i.e., larger the τ value, slower the crack growth. The observed exponential radial crack growth is probably a combined result from the residual strain energy dissipation and the existence of water in the ambient air, as the presence of water may reduce the energy barrier required for the formation of new fracture surfaces [Michalske and Freiman 1983].

While the exponential growths of radial cracks were observed for the lower four loads (0.98 N, 1.96 N, 2.94 N, and 4.91 N), no radial crack growth was observed for the highest load, 9.81 N, which indicates that the exponential growth of radial cracks is load dependent. A closer examination of τ for the four indentation loads that induced exponential radial crack growth did not yield a specific pattern as shown by Figure 8.4, which indicates that the crack growth rate may not be load dependent.

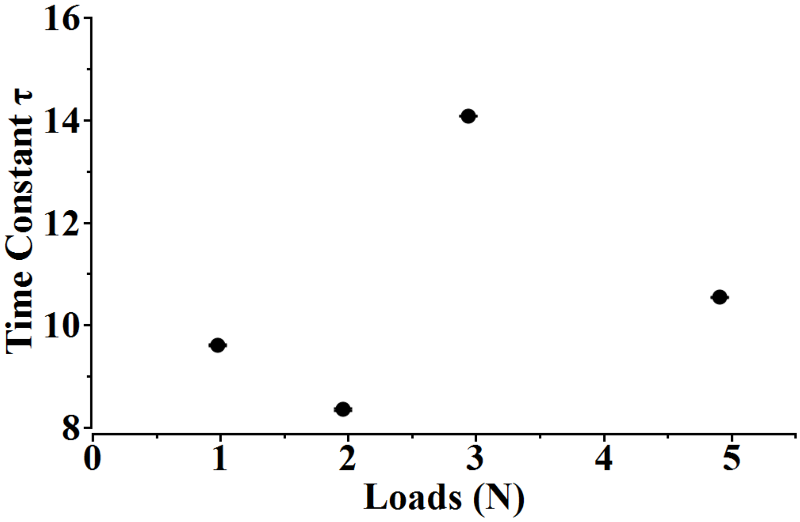

Figure 8.4 The time constant τ obtained from the least-square fit of equation (11) to the average radial crack length versus time data for the 0.98 N, 1.96 N, 2.94 N, and 4.91 N loads. The error bars represent the standard deviation from each curve fitting.

It is important to note that the exponential growth model was deduced by considering radial crack growth as a result of the release of residual strain energy. In the Vickers indentation system, however, lateral cracks may also occur in parallel with radial cracks and share the same residual strain energy reservoir for growth. Thus, the perturbation from lateral cracks may contribute to the lack of radial crack growth at 9.81 N and influence the radial crack growth rate at the four lower loads.

Perturbation from lateral crack

Ideally, after Vickers indentation, a completely evolved crack system has two radial cracks aligned with the indentation impression diagonals and four lateral cracks in the subsurface region near the hemispherically deformed zone, intercepting the specimen surface in quarter sections divided by radial cracks (shown schematically in Figure 8.5) [Lawn et al. 1980]. Lateral cracks that have initiated but not fully evolved are subsurface and difficult to observe until they intercept the free surface of the specimen.

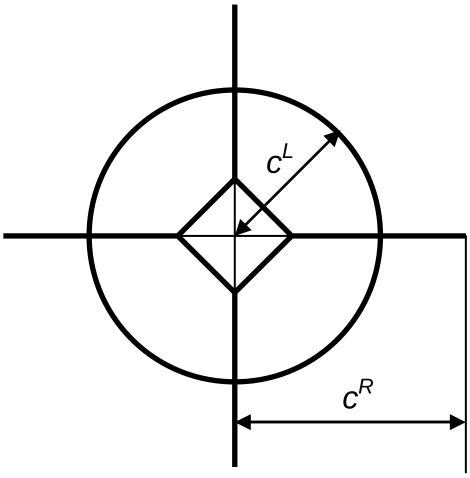

Figure 8.5 A schematic of the fully developed indentation crack system, where c^R is the half radial crack length and c^L is the lateral crack size.

In this study, 30 individual radial cracks were observed for each load (two radial cracks from each of the 15 indentation sites for a given load). However, instead of 60 lateral cracks (four from each indentation site), the number of observed lateral cracks were 37 at 0.98 N, 47 at 1.96 N, 58 at 2.94 N, 57 at 4.91 N, and 59 at 9.81 N, respectively (Figure 8.6). Thus, while the radial crack systems were completely evolved at all loads, the lateral cracks were less likely to intersect the specimen surface at lower loads, although they may have initiated near the hemispherical deformation zone. However, with increasing load, there is an increasing likelihood of a fully developed lateral crack system (Figure 8.6).

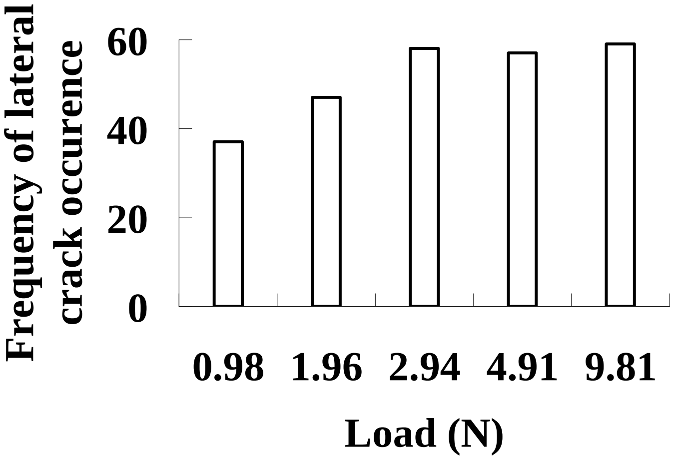

Figure 8.6 The relative frequency of lateral cracks observed intersecting with free surface from 15 indentations at each of the five Vickers indentation loads (0.98 N, 1.96 N, 2.94 N, 4.91 N, and 9.81 N).

For all indentation loads, significant increases from initial lateral crack lengths to saturated lateral crack lengths were detected using paired student's t-test ($p < 0.01$) [Bethea et al. 1985]. The ratio of c_0^L / c_0^R and c_s^L / c_s^R are calculated and compared at all loads, where c_0^L and c_0^R are initial lateral and radial crack lengths, while c_s^L and c_s^R are saturated lateral and initial crack lengths, respectively.

As shown in Figure 8.7, both the relative initial crack length c_0^L / c_0^R and the relative saturated crack length c_s^L / c_s^R increased with increasing load. Also, the saturated c_s^L / c_s^R ratio were lower than the initial c_0^L / c_0^R ratio for the four lower loads, and the contrary trend was observed for the highest load (9.81 N), which strongly indicates that the energy partitioning by lateral cracks increases with increasing load and lateral crack growth becomes dominant at higher load.

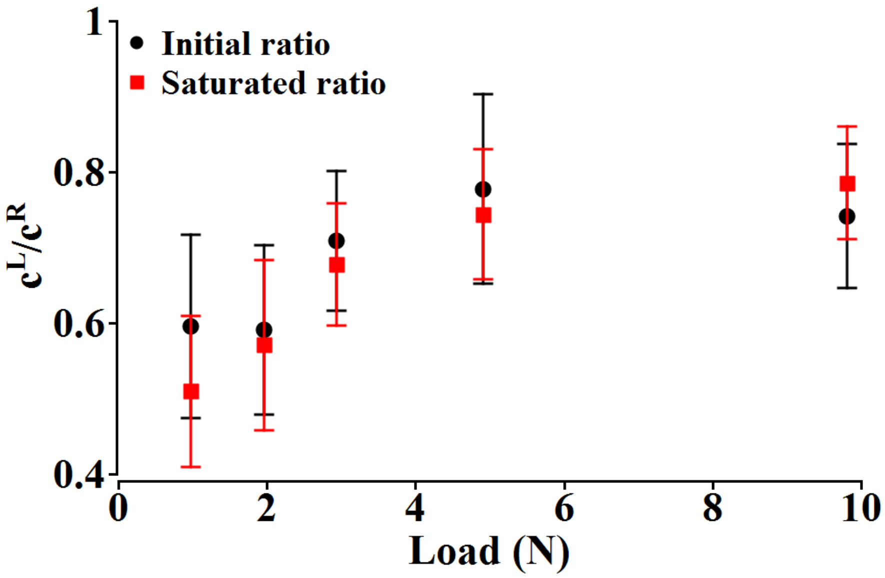

Figure 8.7 The average ratio of initial lateral crack length (c_0^L) over half initial radial crack length (c_0^R) (●), and the average ratio of saturated lateral crack length (c_S^L) over half saturated radial crack length (c_S^R) (■) as a function of Vickers indentation loads. The error bars represent the standard deviations.

Under the assumption that the stored strain energy is partitioned between radial and lateral cracks, the load dependence of the radial cracks growth (section 4.4.1) thus is directly related to the evolvement of the lateral cracks (Figure 8.6 and 8.7). As load increases, the total plastic strain energy increases, however, the relative fraction of residual strain energy available for driving radial cracks growth may decrease due to the increasing share of companying lateral crack. This explains the absence of radial crack growth with time at 9.81 N, in which case the residual strain energy was likely consumed mostly by the lateral crack growths.

Other factors that may affect the growth of radial cracks

In addition to perturbation from lateral cracks, other factors such as microcracking, porosity as well as grain size and shape, can affect the growth of indentation cracks. Any material with lower atomic symmetry than cubic is subject to microcracking due to TEA [Case et al. 2005]. Since HA is not cubic (the unit cell of HA (a = b = 9.432 Å, c = 6.881 Å) [Kay et al. 1964], HA is a noncubic material. Microcracking in single phase HA has been confirmed by Case et al [2005]. Pre-existing microcracks from TEA may in turn affect the indentation crack behavior via crack branching [Nie et al. 2009, Zhang et al. 2003] and by lowering the local [Swan 1990] as well as the global [Sridhar et al. 1994] elastic modulus.

Since isolated quasi-spherical pores are present in the HA substrates used in this study (Figure 8.2), it is necessary to keep in mind that porosity also influences crack behavior. In a study of SiC, Deng *et. al.* identified that the reinforcement of porous ceramics through crack tip blunting [Deng et al. 2004], where crack propagation in a dense body showed a sharp crack-tip, but showed a blunt crack-tip in porous ceramic body.

The mean grain size of HA specimens in this study is approximately 7.9 µm, which is smaller than the dimensions of the smallest indentation impression (19 µm at 0.98 N). However, when the grain size and indentation size become comparable, local grain failure can disrupt the radial/lateral crack pattern [Shivakuma and Crews 1987]. Also, though not observed in the current study, the variation in grain shape and orientation may affect the fracture pattern of Vickers indentation, since grain boundaries can deflect crack propagation [Faber and Evans 1983, Suresh 1983].

Ambient environment may also affect the slow crack growth behavior. Environmentally assisted crack growth refers to an enhancement in crack growth that takes place due to a stress-enhanced chemical reaction at the highly strained region near a crack tip [Michalske and Freiman 1983, Wiederhorn 1968, Freiman et al. 2009]. In particular, when exposed to water, HA exhibits higher susceptibility to slow crack growth than in air as indicated by n values of 10 ± 4, 11.3, 11 measured in water, which are lower than the n values measured in ambient air ($n = 22.5 \pm 2$, 19.8, 23) [Raynaud et al. 1998, Barinov and Shevchenko 1995, Barinov et al. 2003].

SUMMARY AND CONCLUSIONS

This paper addresses the slow growth behavior for Vickers indentation induced radial/lateral cracks in hydroxyapatite during the aging process in ambient air at room temperature. For each of the five applied indentation loads F, the residual strain energy was released through radial and/or lateral crack propagation during the first hour of aging in air.

The radial cracks grew exponentially (equation 11) at four indentation loads (0.98 N, 1.96 N, 2.94 N, 4.91 N) (Figure 8.3). No specific trend was observed for radial crack growth rate as characterized by the time constant τ for the four indentation loads (0.98 N, 1.96 N, 2.94 N and 4.91 N) selected in this study (Figure 8.4).

However, the radial cracks did not grow at $F = 9.81$ N, likely due to a load dependent change in the partitioning of strain energy from the hemispherically deformed zone to the radial and lateral cracks, with the result being that post-indentation lateral crack growth became dominant at higher load levels. With increasing indentation load, we observed an increase in both (1) the frequency of occurrence of the lateral cracks (Figure 8.6) and (2) the relative lateral/radial crack ratio (Figure 8.7), both of which reflect the increase in the relative “share” of the residual strain energy with the radial crack system.

This study suggests that the slow growth of radial cracks is a load dependent process, which has not been reported previously in the literature. Using measurements of the time dependent radial and lateral cracks lengths along with a simple model of the energy partitioning, we propose that the load dependence of radial crack growth is linked to this partitioning of residual strain energy.

If lateral crack growth very suppressed, then the extension of radial crack length due to adding in a humid or aqueous environment may occur for all loads. However, indentation-induced residual stress and the emergence of both a median/radial crack system and a lateral crack system add complexity to Vickers indentation induced radial crack growth behavior [Lawn et al. 1980, Marshall et al. 1982].

Thus, when using Vickers indentation radial crack as the model crack as mentioned in the introduction section, both the environmental assisted slow growth of radial crack and the disturbance from lateral cracks should be treated carefully. Also, it is important to note that when there are concentrated residual stress introduced into a brittle material body, crack propagation may take place in the form of both radial cracks (cracking) and/or lateral cracks (chipping, spalling or flaking) [Ahr et al. 2003, Srinivasam et al. 1990, Swain and Lawn 1976].

APPENDIX A THE ROLE OF RESIDUAL STRESS IN CRACK FORMATION/PROPAGATION DURING VICKERS INDENTATION

This study focuses on the time and load dependence of Vickers radial and lateral cracks as they evolve during post-indentaion aging in humid air. Vickers indentation tips with an included angle of 136° were described by Chiang et al. [1982] as generating an elastic/plastic deformation mode. During a complete cycle of loading and unloading of a Vickers indentation, median, radial and lateral cracks may form. The two crack systems were classified according to their orientations with respect to the loading plane, where median/radial cracks lay within the loading plane while lateral cracks lay in planes parallel to the surface [Lawn et al. 1980]. During loading, downward tensile stress favors the propagation of the median crack, and the radial/lateral crack propagation was prevented by the asymmetric compressive stress within the elastic field. Upon unloading, the residual plastic zone remained, driving radial/lateral crack growth [Lawn et al. 1980]. Both radial and lateral cracks were observed upon unloading in the current study at all indentation loads (0.98 N, 1.96 N, 2.94 N, 4. 91 N, 9.81 N).

Since in the current study, the growth of radial/lateral cracks were observed when no external stresses were applied, it is then curious that where the driving energy may come from and how many energy sources there might be. In a comprehensive review of indentation fracture, Lawn and Wilshaw proposed a simplified model of the stress field about Vickers indentations [Lawn and Wilshaw 1975]. The material directly in contact with the indenter tip was assumed to form a “hydrostatic core” which exerts pressure on the surrounding material and results in the formation of a “plastic zone”, where both the plastic zone and the hydrostatic core were assumed to be spherically symmetric. Beyond the “plastic zone” was the “elastic matrix” [Lawn and Wilshaw 1975]. An irreversible residual plastic deformation zone was created during loading and persisted after unloading beneath the indentation impression as a compressed semi-sphere within the elastic matrix [Lawn et al. 1980]. The stored residual strain energy in that hemispherical deformation zone is thus what is left to provide the driving energy for the observed growth of both radial and lateral cracks in this study.

The role of residual stress in driving the observed crack growth should not be confused with the role of water discussed in section 2. Residual stresses from the plastic deformation zone under Vickers indentation is acting like an energy reservoir for the growth of both radial and lateral cracks upon unloading. However, the existence of water does not provide energy but rather lower the energy barrier required for the advance of radial cracks tips. Also, note that only cracks on the free surface are exposed to water, thus water may assist the growth of radial cracks but could not affect the subsurface propagation of lateral cracks.

The role of residual stress in driving both radial/lateral cracks upon unloading showed that there must be a partitioning between the stored strain energy between radial and lateral cracks as pointed out multiple times in the paper.

REFERENCES

REFERENCES

[Ahr et al. 2003] Ahr Y, Cho N, Lee S, Lee D. Lateral crack in abrasive wear of brittle materials. Japan Soc Mech Eng Int J A 2003; 26: 140-144.

[Anderson and Rowcliffe 1996] Anderson T, Rowcliffe DJ. Indentation thermal shock test for ceramics. J Am Ceram Soc 1996; 79: 1509-1514.

[Anthony et al. 2000] Anthony JW, Bideaux RA, Bladh KW, and Nichols MC. Handbook of mineralogy Volume IV. Virginia: Mineral Data Publishing, 2000.

[Antis et al. 2006] Antis GR, Chantikul P, Lawn BR, and Marshall DB. A critical evaluation of indentation techniques for measuring fracture toughness: I, Direct crack measurements. J Am Ceram Soc 2006; 64: 533-538.

[Apostol 1962] Apostol TM. *Calculus: Volume II*, John Wiley & Sons, New York, 1962.

[ASTM 1465] Standard test method for determination of slow crack growth parameters of advanced ceramics using constant stress-rate flexural testing at elevated temperatures, 2003.

[ASTM C 1327-03] Standard Test Method for Vickers Indentation Hardness of Advanced Ceramics, 2003.

[ASTM C1368] Standard test method for determination of slow crack growth parameters of advanced ceramics using constant stress-rate flexural testing at ambient temperature, 2003.

[Barinov and Shevchenko 1995] Barinov SM and Ja V. Shevchenko, Dynamic fatigue of porous hydroxyapatite ceramics in air. J Mater Sci Lett 1995; 14: 582-583.

[Barinov et al. 2003] Barinov SM, Tumanov SV, Fadeeva IV, and Bibikov VY. Environment effect on the strength of hydroxyl- and fluorohydroxyapatite ceramics. Inorganic Mater 2003; 39: 877-880.

[Benaqqa et al. 2004] Benaqqa C, Chevalier J, Saadaoui M, and Fantozzi G. *Slow Crack Growth in Bioactive Ceramics*, Trans Tech Publications, Switzerland, 2004.

[Benaqqa et al. 2005] Benaqqa C, Chevalier J, Saadaoui M, Fantozzi G. Slow crack growth behaviour of hydroxyapatite ceramics. Biomaterials 2005; 26: 6106-6112..

[Bethea et al. 1985] Bethea RM, Duran BS, Boullion TL (ed.), *Statistical Methods for Engineers and Scientists*, Marcel Dekker Inc., NewYork, 1985.

[Burmeister 1993] Burmeister LC. Convective heat transfer, 2nd edition, published by Wiley Interscience (1993) 107.

[Case et al. 2005] Case ED, Smith IO, and Baumann MJ. Microcracking and porosity in calcium phosphates and the implications for bone tissue engineering. Mater Sci Eng A 2005; 390: 246-254.

[Chantikul et al. 1981] Chantikul P, Lawn BR, and Marshall DB. Micromechanics of flaw growth in static fatigue: Influence of residual contact stresses. J Am Ceram Soc 1981; 64: 322-325.

[Chiang et al. 1982] Chiang SS, Marshall DB, and Evans AG. The response of solids to elastic/plastic indentation. I. Stresses and residual stresses. J Appl Physic 1982; 53: 298-311.

[Chladek et al. 2004] Chladek J, Muller R, Weh L, Reinsch S. Viscous flow and surface crystallization caused by Vickers indentation. Glass Sci Technol 2004; 77: 1 – 6.

[Chlup et al. 2008] Chlup Z, Flasar P, Kotoji A, Dlouhy I. Fracture behaviour of Al2O3/SiC nanocomposite ceramics after crack healing treatment. J Eur Ceram Soc 2008; 28: 1073 – 1077.

[Choi et al. 2006] Choi SR, Nemeth NN, Gyekenyesi JP. Slow crack growth of brittle materials with exponential crack velocity under cyclic fatigue loading. Int J Fatig 2006; 28: 164-172.

[Connally and Brown 1992] Connally JA and Brown SB. Slow crack growth in single-crystal silicon. Science, New Series 1992; 256: 1537-1539.

[Dey and Mukhopadhyay 2011] Dey A and Mukhopadhyay AK. Fracture toughness of microplasma-sprayed hydroxyapatite coating by nanoindentation. Int J Appl Ceram Technol 2011; 8: 572-590.

[Deng et al. 2004] Deng Z, She J, Inagaki Y, Yang J, Ohji T, Tanaka Y. Reinforcement by crack-tip blunting in porous ceramics. J Eur Ceram Soc 2004; 24: 2055-2059.

[Dwivedi and Green 1995] Dwivedi PJ and Green DJ. Determination of subcritical crack growth parameters by in situ observation of indentation cracks. J Am Ceram Soc 1995; 78: 2122-2128.

[Faber and Evans 1983] Faber KT, Evans AG. Crack deflection processes-II. Experiment. Acta Metallurgica 1983; 31: 577-584.

[Fan et al. submitted 2011] Fan X, Case ED, Ren F, Shu Y, Baumann MJ. Part II: Fracture strength and elastic modulus as a function of porosity for hydroxyapatite and other brittle materials. Submitted to Phil Mag 2011.

[Freiman et al. 2009] Freiman SW, Wiederhorn SM, Mecholsky JJ. Environmentally enhanced fracture of glass: A historical perspective. J Am Ceram Soc 2009; 92: 1371-1382.

[Gamlen et al. 1991] Gamlen CA, Case ED, and Reinhard DK. Adhesion of Diamond Thin Films on Silicon Wafers. J Appl Phys Lett 1991; 59: 2529 2531.

[Halliday et al. 1997] Halliday D, Resnick R, and Walker J. *Fundamentals of Physics Part 3 and Part 5*, John Wiley & Sons, New York, 1997.

[Hontsu et al. 1997] Hontsu S, Matsumoto T, Ishii J, Nakamori M, Tabata H, Kawai T. Electrical properties of hydroxyapatite thin films grown by pulsed laser deposition. Thin Solid Films 1997; 295: 214-217.

[Ibrahim et al. 2007] Ibrahim A, Lima RS, Berndt CC, Marple BR. Fatigue and mechanical properties of nanostructured and conventional titania (TiO2) thermal spray coatings. Surf Coat Technol 2007; 201: 7589 – 7596.

[Kay et al. 1964] Kay MI, Young RA, and Posner AS. Crystal structure of hydroxyapatite, Nature 1964; 204: 1050-1052.

[Lawn and Wilshaw 1975] Lawn B, Wilshaw R. Indentation Fracture: Principles and Applications. J Mater Sci 1975; 10: 1049-1081.

[Lawn et al. 1980] Lawn BR, Evans AG and Marshall DB. Elastic/Plastic Indentation Damage in Ceramics: The Median/Radial Crack System. J Am Ceram Soc 1980; 63: 574-581.

[Lawn et al. 1993] Lawn BR, Padture NP, Braun LM, Bennison SJ. Model for Toughness Curves in Two-Phase Ceramics: I, Basic Fracture Mechanics. J Am Ceram Soc 1993; 76: 2235-2240.

[Lee et al. 2002] Lee SK, Moretti JD, Readey MJ, Lawn BR. Thermal shock resistance of silicon nitrides using an indentation-quench test. J Am Ceram Soc 2002; 85: 279-281.

[Marshall and Lawn 1980] D. B. Marshall and B. R. Lawn, Flaw characteristics in dynamic fatigue: The influence of residual contact stresses, Journal of American Ceramic Society 63 (1980) 532-536.

[Marshall et al. 1982] Marshall DB, Lawn BR, and Evans AG. Elastic/plastic indentation damage in ceramics: The lateral crack system. J Am Ceram Soc 1982; 65: 561-566.

[Michalske and Freiman 1983] Michalske TA and Freiman SW. A molecular mechanism for stress corrosion in vitreous silica. J Am Ceram Soc-Green 1983; 66: 284-288.

[Mori et al. 2003] Mori K, Hara T, Mizugaki T, Ebitani K, and Kaneda K. Hydroxyapatite-bound cationic ruthenium complexes as novel heterogeneous lewis acid catalysts for diels-alder and aldol reactions. J Am Chem Soc 2003; 125: 11460-11461.

[Mori et al. 2004] Mori K, Hara T, Mizugaki T, Ebitani K, and Kaneda K. Hydroxyapatite-supported palladium nanoclusters: a highly active heterogeneous catalyst for selective oxidation of alcohols by use of molecular oxygen. J Am Chem Soc 2004; 126: 10657-10666.

[Nagai and Nishino 1988] Nagai M, Nishino T. A new type of CO2 gas sensor comprising porous hydroxyapatite ceramics. Sensor and Actuat 1988; 15: 145-151.

[Nie et al. 2009] X. W. Nie, S.G. Lu, K. L. Wang, T. C. Chen, C. J. Niu, Mater. Sci. Eng. A 502 (2009) p. 85.

[Owada et al. 1989] Owada H, Yamashita K, Umegaki T, Kanazawa T. Humidity-sensitivity of yttrium substituted apatite ceramics. Solid State Ionics 1989; 35: 401-404.

[Park and Lakes 2007] Park J and Lakes RS. *Biomaterials: An Introduction*, Springer, Madison, 2007.

[Raicevic et al. 2005] Raicevic S, Kaludjerovic-Radoicic T, Zouboulis AI. In situ stabilization of toxic metals in polluted solids using phosphates: theoretical prediction and experimental verification. J Hazard Mater B 2005; 117: 41-53.

[Raynaud et al. 1998] Raynaud S, ChampionE, Bernache-Assolant D, Tetard D. Dynamic fatigue and degradation in solution of hydroxyapatite ceramics. J Mater Sci: Mater Med 1998; 9: 221-227.

[Reed-Hill 2009] Reed-Hill RE. *Physical Metallurgy Principles*, Cengage

Learning, Stamford, 2009.

[Ren et al. 2009] Ren F, Case ED, Morrison A, Tafesse M, and Baumann MJ. Resonant ultrasound spectroscopy measurement of Young’s modulus, shear modulus and Poisson’s ratio as a function of porosity for alumina and hydroxyapatite. Phil Mag 2009; 89: 1163-1182.

[Rice 1996] Rice RW. Porosity dependence of physical properties of materials: A summary review, Source: Porous Ceramic Materials, Book series: Key Engineering Materials, Vol. 115 (1996) 1-19.

[Ritter and Sherburne 1971] Ritter JE, Jr. and Sherburne CL. Dynamic and static fatigue of silicate glasses. J Am Ceram Soc 1971; 54: 601-605.

[Salomonson et al. 1996] Salomonson J, Zeng K and Rowcliffe D. Decay of residual stress at indentation cracks during slow crack growth in soda-lime glass. Acta Materialia 1996; 44: 543-546..

[Schell et al. 2010] Schell KG, Bucharsky EC, Oberacker R, and Hoffmann MJ. Determination of subcritical crack growth parameters in polymer-derived SiOC ceramics by biaxial bending tests in water environment. J Am Ceram Soc 2010; 93: 1540-1543.

[Shivakuma and Crews 1987] Shivakumar KN and Crews JH Jr. Energy dissipation associated with crack extension in an elastic-plastic material. Eng Fract Mech 1987; 28: 319-330.

[Shu submitted 2011] Shu Y, Baumann MJ, Case ED, Irwin RI, Meyer SE, McCabe LR. submitted to J Biomed Mater Res-A 2011.

[Silva et al. 2006] Silva OG, Filho ECS, Gonseca MG, Arakaki LNH, Airoldi C. Hydroxyapatite organofunctionalized with silylating agents to heavy cation removal. J Colloid Interface Sci 2006; 302: 485-491.

[Smith 2007] Smith IO, *The effect of grain size, microcracking and grain boundary grooving on osteoblast attachment in hydroxyapatite*, Ph. D. dissertation, Michigan State University, 2007.

[Spriggs 1961] Spriggs RM. Expression for effect of porosity on elastic modulus of polycrystalline refractory materials, particularly aluminum oxide. J Am Ceram Soc 1961; 44: 628-629.

[Sridhar et al. 1994] Sridhar N, Yang W and Srolovitz DJ. Microstructural mechanics model of anisotropic-thermal-expansion-induced microcracking. J

Am Ceram Soc 1994; 77: 1123-1138.

[Srinivasam et al. 1990] Srinivasam S, Russ JC, and Scattergood RO. Fractal analysis of erosion surfaces. J Mater Res 1990; 5: 2616-2619.

[Suresh 1983] Suresh S. Crack deflection: Implications for the growth of long and short fatigue cracks. Metall Mater Trans A 1983; 14: 2375-2385.

[Swain and Lawn 1976] Swain MV and Lawn BR. Indentation fracture in brittle rocks and glasses. Int J Rock Mech Mining Sci & Geomech Abs 1976; 13: 311-319.

[Swain 1990] Swain MV. R-Curve behavior and thermal shock resistance of ceramics. J Am Ceram Soc 1990; 73: 621-628.

[Tomozawa 1996] Tomozawa M. Fracture of glasses. Annu Rev Mater Sci 1996; 26: 43-74.

[Underwood et al. 1968] Underwood EE, Colcord AR and Waugh RC. Ceramic Microstructures, edited by Fulrath RM and Pask JA. New York: John Wiley and Sons, 1968, Page 25.

[Venugopal and Scurrell 2003] Venugopal A, Scurrell MS. Hydroxyapatite as a novel support for gold and ruthenium catalysts: Behavior in the water gas shift reaction. Appl Catal A: Gen 2003; 245: 137-147.

[West and Hench 1998] West JK and Hench LL. The effect of environment on silica fracture: Vacuum, carbon monoxide, water and nitrogen. Phil Mag A 1998; 77: 85-113.

[Wiederhorn 1968] Wiederhorn SM. Moisture assisted crack growth in ceramics. Int J Fract Mech 1968; 4: 171-177.

[Wiederhorn 1974] Wiederhorn SM. *Subcritical crack growth in ceramics*, in *Fracture Mechanics of Ceramics*, R. C. Bradt, eds., Plenum Publishers, New York, 1974, p. 613.

[Wilson and Case 1997] Wilson BA and Case ED. In situ microscopy of crack healing in borosilicate glass. J Mater Sci 1997; 32: 3163-3175.

[Wilson and Case 1999] Wilson BA and Case ED. Effect of humidity on crack healing in glass from in-situ investigations using an ESEM. J Mater Sci 1999; 34: 247-250.

[Withers and Bhadshia 2001] Withers PJ and Bhadshia HKDH. Residual stress part 2-nature and origins. Mater Sci Tech 2001; 17: 366-375.

[Zhang et al. 2003] Zhang H, Wang D, Chen S, Liu X. Toughening of MoSi2 doped by La2O3 particles. Mater Sci Eng A 2003; 345: 118-121.

CHAPTER 9

SUMMARY AND FUTURE DIRECTIONS

This project is illustrated by anecdotal data showing that in the fractured bones of racing horses and/or greyhound, microcracks coincided with bone densification. The formation of microcracks not only dissipates excessive energy and prevents catastrophic fracture, but may also induce bone remodeling. Though microcracks are a widely-recognized defect in engineering ceramics, it may also be a beneficial feature in bone scaffold design in terms of stimulating bone formation. The current project is thus designed to investigate the osteoblast (bone forming cell) response to microcracks.

In this project, microcracks were introduced into hydroxyapatite scaffold using Vickers indentation. The temporal development of osteoblasts on non-cracked (control) and cracked (experiment) were compared. The presence of microcracks was shown to induce OB alignment and enhance OB attachment as well as maturation, which indicates that microcracks are able to signal faster bone formation *in vitro*.

The underlying mechanism for the observed OB response to microcracks may be attributed to the increase in calcium ion concentration (Chapter 5) and the alteration in the extracellular matrix (Chapter 6 and Appendix A) due to the presence of microcracks. It is likely that at the early attachment phase, the calcium ion increase in the local environment guides cell migration towards the cracks. The radial crack tips as well as the lateral crack spalling may be then sensed by the arriving cells, which results in varied conformation of their extracellular matrix. The alteration of the arriving cells may further affect other approaching cells and leads to the observed OB alignment around the crack boundary.

With extended time, the cells on the HA surface become confluent and proceed into the differentiation stage. The cells and their ECM that fill in the indentation impression is likely to have a different conformation and present a different mechanical strain field as compared to the cells and ECM on the flat surfaces. According to the local strain-cue model (Appendix A) [Cox 2010], local variations in the mechanical strain field may contribute to the localized mineral deposition observed in the CLSM micrographs shown in Chapter 4.

In order to prove the above hypothesized mechanisms, future studies should be done to verify the following two aspects: First, osteoblast migration in response to calcium gradients in the local environment should be assessed by introducing calcium source, such as soluble calcium phosphate during cell culturing; second, alteration in the strain field within the cell and ECM localized at the microcrack region should be measured using computational methods. A live cell imaging could be carried out to monitor the cell migration, which may provide an experimental basis for establishing a strain-cue model to simulate the cellular response to the presence of microcracks.

In the current study, microcracks were introduced using Vickers indentations as described in Chapter 4. Though Vickers indentations can be well controlled, the radial and lateral crack patterns, as well as the indentation impression, comprise a complex surface feature. Thus, other machining methods that can separate radial cracks, lateral cracks, and the indentation impression could be used. One possible choice is to use the Sonic Mill, which enables the introduction of slots or any other surface features of interests onto substrate surfaces. The flexibility of Sonic Mill could be applied to introduce desired surface features to investigate cellular responses in future studies. Comparing to Vickers indentation, slots introduced using Sonic Mill will not present sharp tips as radial cracks and their sizes (length and opening) will be considerably larger than cracks introduced using Vickers indentation.

Besides probing into the underlying mechanism, future studies could also be done to investigate the practical value of introducing microcracks to artificial scaffolds that are already on the market, to study the *in vivo* bone healing process in animal models.

APPENDICES

APPENDIX A

BONE RESPONSE TO MECHANICAL STIMULI AND THE LOCAL STRAIN-CUE HYPOTHESIS

The adaptability of bone to mechanical stress/strain had long aroused people's interests. Wolff's law which stated that the distribution of bone mass was determined by the distribution of mechanical stress was proposed in 1892 [Wolff 1892]. Twenty years later, Thomson [1961] emphasized the importance of mechanical strain rather than stress in directly stimulating bone growth [Thompson 1961]. Frost [1964] further pointed out there was a minimum strain threshold to be met for bone adaption to happen in 1964. Liskova and Hert [1971] made an important leap by demonstrating dynamic strains rather than static strains that induced bone increase in 1971. After that, the importance of peak strain and loading waveform frequency (the number of cycles per second) to bone adaptation were proved by Rubin and Lanyon [1985 and 1994] around 1980s. Turner et al [1995] further confirmed the importance effects of strain rate and loading frequency in modifying bone growth. Following the discovery of the importance of dynamic/cyclic loading, a saturation of bone mass increase was demonstrated after a short loading period by Rubin and Lanyon [1984] using avian ulna, and by Umemura et al [1997] using rat tibia. Further more, bone adaptation was more driven by "abnormal" loading conditions rather than "normal" daily activities as proposed by Lanyon [1992], which showed the possibility of accommodation of bone to routine activities within a certain range on a cellular level.

Extensive studies had also been carried out to investigate the dependence of bone adaptation on strain type, magnitude, frequency, and distribution. The bone adaptation studies have been carried out both *in vitro* and *in vivo* and at both macro and micro levels by different researchers.

In order to carry out experiments that could simulate bone growth *in vivo*, the quantification of strain experience by bone is a must. Fritton and Rubin [2001] had reviewed the peak strain and strain rate measured in different species and different activities, which could vary from less than 1000 microstrain to 5000 microstrain. However, this gives only the information of normal functional strain, the driving force for bone adaption as proposed by Lanyon [1992] (i.e., the abnormal loading superimposed on normal functional strain) is not determined. Lots of studies found a correlation between strain magnitude and frequency, such that the minimum strain magnitude required to induce bone growth decreases with an increase of frequency. For example, in Rubin et al's study with the isolated avian ulna model, a mechanical load of 500 microstrain had no effect on osteogenesis at 1 Hz, while obviously enhanced osteogenesis at 10 Hz and above [Rubin and McLeod 1994]. Robling and Turner [2009] found that at 1 Hz, the minimum strain needed to initiate bone formation is 1820 microstrain, but dropped to 1180 microstrain at 5 Hz, and dropped to only 650 microstrain at 10 Hz.

The mechanical stimuli occur *in vivo* include compression, tension, fluid shear components. Each of the above components and/or combinations of them has been extensively studied by different researchers using various techniques. Dong et al [2001] analyzed the alkaline phosphatase activities by subjecting osteoblast seeded on a porous hydroxyapatite scaffold under a set of low pressures, which were 760 mmHg (normal atmospheric pressure), 500 mmHg, 250 mmHg, 100 mmHg, 50 mmHg, and 10 mmHg for durations of 4 weeks and 8 weeks. They found that the 100 mmHg showed highest ALP acitivity, and ALP activity was higher at 4 weeks than 8 weeks in all groups. Song et al [2007] studied the proliferation of human bone marrow mesenchymal cells (hMSCs) by applying cyclic longitudinal mechanical stretch with different magnitude, frequency, and duration. At a fixed strain 10% and duration of 15 minutes, 1.0 Hz showed highest relative proliferation (normalized with control 0 Hz) compared with 0.01 Hz, 0.1 Hz, 0.5 Hz, and 1.5 Hz. At a fixed frequency 1.0 Hz, proliferation of hMSCs was enhanced at 5% strain for 15, 30, and 60 minutes, was enhanced at 10% strain for 15 and 30 minutes, was enhanced at 15% for 30 and 50 minutes, and longer durations of 12 hours and 24 hours blocked proliferation. Shivaram et al [2010] applied a maximum shear stress of 1 Pa using a sinusoidal wave form at 1 Hz to MC3T3-E1 osteoblasts, and showed an up-regulation of 103 known genes and expressed sequence tags (ESTs) and down-regulation of 67 known genes and ESTs.

Techniques could be applied to simulate mechanical input in vivo such as compressive, tensile, and shear strain were reviewed in great detail by

Brown [2000]. Compressive stresses could be achieved by using hydrostatic pressure and/or direct platen abutment; tensile stresses could be applied using uniaxial tension, substrate bending and out-of-plane or in-plane circular substrate distention (Flexercell uses vacuum to realize substrate deformation); shear stress could be introduced using cone and plate flow chamber and/or parallel plate flow chamber [Brown 2000]. Other techniques that combine substrate distension and fluid shear were also developed. One approach used by Benbrahim et al [1994] was to grow cultures on the inner wall of highly distensible tubes, where the shear stress was pressure gradient dependent, and substrate distension was internal pressure dependent.

To fully understand the reason behind bone adaptation to mechanical stimuli, people had long intended to explore the story at cellular level. Ehrlich and Lanyon [2002] gave a detailed review on mechanical strain and bone cell function. They mainly discussed the release of prostanoids, nitric oxide, and insulin-like growth factors (IGFs) during bone adaptation to mechanical stiumuli, which suggested the involvement of cation channels and intracellular calcium increase in bone cell repose to mechanical stimuli [Ehrlich and Lanyon 2002, Klein-Nulend et al 1998, Zaman 1999 and Ralston 1997]. Iqbal and Zidi [2005] discussed molecular regulation of mechanotransduction on a more general base regardless of cell types, which summarized the role of integrin in interacting with environment, mediating the increase of intracellular Ca^{2+} levels and activating MAP kinase cascades that led to ERK1/2 phosphorylation, which then activated the AP-I family of transcription factors for pro-growth response involving up-regulation of the genes *c-fos*, IFG-I, cyclooxygenase, and osteocalcin. Nesbitt et al [2009] found that mechanical loading of bone cell could stimulate Wnt/β-catenin signaling, which could result in the generation of new bone mass.

While the above mechanical stimuli are global and have high strain rate ($>1s^{-1}$), Cox [2010] brought up a strain-cue theory which hypothesized that the cell migration and cell network formation was cued by localized strain (nearest 100 cells) generated in the host media (host cell and extracellular matrix). Cox built his strain-cue model by considering the invasion of cells to a densely packed host media, such that when accommodating the new invading cell, the host media must displace and thus lead to changes in the local strain field. The invading cells tend to migrate in the direction perpendicular to the tensile direction. Cox model considers only the variation of the strain field but not the diffusion distance of chemical signals.

The simulated strain rate from Cox's model is 10^{-4} s^{-1} during loading and 10^{-5} to 10^{-6} s^{-1} during unloading, which are much lower than the strain rates used in conventional mechanical stimuli studies. The localized as well as low strain rate generated by the host media during accommodating invading cells may be referred to explain our observation of localized mineralization in the indentation center as discussed in chapter 4.

However, the diffusion of chemical signals, in our case calcium should not be neglected. At the early cell attachment phase, the ECM matrix and host cells are not closely packed and thus the local strain-cue may not be effective until the cells reach confluency at later times.

APPENDIX B

CALCIUM CONCENTRATION MEASUREMENT USING ATOMIC ABSORPTION SPECTROSCOPY

Atomic absorption spectroscopy (AAS) is a chemical analysis method first proposed by Walsh in 1955 [Walsh 1955]. As shown in Figure B-1, the atomic absorption spectrophotometer consists of four major parts: the light source, the flame or atomizer, the monochrometer and the detector.

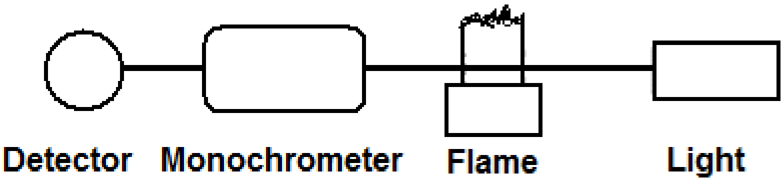

Figure B-1 Schematic of atomic absorption spectrophotometer structure.

The light source is a hollow cathode lamp, where the cathode is made from either the element to be measured or its alloy. The lamp emits light that could be absorbed by the to-be-measured atoms in the sample. Thus in the case of calcium measurement, a calcium cathode lamp is used as the light source, which generate a light wavelength of 422.7 nm.

In the sample compartment, the sample is atomized by heat dissociation. The heat can be generated either from a chemical flame or an electrical furnace. In our case, an oxygen rich flame (2000 to 3000 ºC) is used to dissociate the sample into free atoms. The free atoms can absorb the radiant energy of their specific resonance wavelength. The light absorbance after passing through the flame is proportional to the number of free atoms in the flame. The concentration of the target element, in this case calcium can be obtained by measuring the light absorbance.

The monochrometer selects the wavelength to analyze the target element. The analysis wavelength for calcium is 422.7 nm. The detector then converts light into electrical signals.

Prior to the measurement of calcium concentration in the sample solutions, a concentration versus absorbance curve was plotted using standard calcium solutions. The standard solutions are made by diluting the stock calcium solution (1g/L) in distilled water. The concentrations of standard calcium solutions are 1, 3 and 10 mg/L, respectively. Each standard solution is aspirated into the sample compartment and the absorbance of light is determined. Distilled water is also aspirated as the blank background with 0 calcium concentration. From the above data, a calibration curve of calcium concentration versus absorbance is plotted. After plotting the standard curve, the calcium concentration in the unknown sample solutions can then be measured by aspirating them into the AA flame.

APPENDIX C

SOLID STATE SINTERING OF HYDROXYAPATITE AT 1360℃

In a cooperative study with Fan et al., the porosity dependence of Weibull modulus and strength of brittle ceramics was investigated [Fan et al. submitted 2011]. Hydroxyapatite was chosen as the model ceramic due to its wide application and availability in our research group. In order to obtain a wide range of HA porosity, Fan tried different sintering profiles by changing sintering temperature and time. While HA specimens in the lower (>90%) and higher porosity (<80%) ranges were obtained with consistency in color, the intermediate porosity range specimens were found to show pink-colored spot and tend to break at the interface between different color regions. The un-uniform color is likely caused by uneven heating gradient experienced by the powder compact. However, the detailed cause and mechanism for the occurrence of pink spots remain unclear. We solved the color problem by employing a thick powder bed (at least 3 mm thick) and by maintaining sintering boat in the center of the furnace chamber. In this appendix, the porosity and/or density evolution of HA sintered at a fixed temperature 1360℃ with time is presented and discussed, which provided a map for determining sintering profile for desired densities.

Sintering is defined as “the process that transforms powder compacts into solid, dense body upon heating” [Barsoum 2003]. Sintering could happen with and without liquid phases, which are referred as liquid-phase and solid state sintering respectively. The driving force for sintering is surface energy reduction globally and curvature differences that lead to partial pressure differences locally (equation 1) [Barsoum, 2003].

$$P_{curv} = P_{flat}(1 + \frac{2\Omega_{MX}\gamma_{sv}}{rkT}) \qquad (1)$$

where P_{curv} and P_{flat} are partial pressures above the curved surface and the flat surface respectively, Ω_{MX} is the volume of a formula unit, γ_{sv} is the solid/vapor surface energy, r is the radius of a sphere (negative for concave surfaces and positive for convex surfaces), k (= $1.3806503 \times 10^{-23}$ m^2 kg $s^{-2}K^{-1}$) is the Boltzmann constant such that, and T is the temperature. According to equation (1) and the signs given to concave (-) and convex (+) surfaces, the partial pressure is the highest above a convex surface, followed by flat surface, and lowest above a concave surface.

There are five mass transfer mechanisms: evaporation-condensation, surface diffusion, volume diffusion, grain boundary diffusion, and viscous flow [Barsoum 2003]. The diffusion sink is always the “neck area”, while the diffusion source could be the surfaces or grain boundaries. Depending on the diffusion path in the powder compacts, coarsening (surface to neck area) or densification (grain boundary to neck area) could take place during sintering [Barsoum 2003].

When coarsening and densification take place, shrinkage, grain, and pore sizes of the sintered body could evolve depending on the initial particle sizes, sintering temperature and time. The volume change of a powder compact after sintering could be described by equation (2).

$$\frac{\Delta V}{V_0} = A(T)t^n(1/r)^m \tag{2}$$

where ΔV is the volume change after sintering, V_0 is the initial volume of the green powder compact, A(T) is temperature dependent function, t is sintering time, the observed n often ranges from 0.1 to 0.5, r is the initial particle size, m varies from 1 to 2.

For a given particle size and a fixed sintering temperature, Equation 2 could be simplified and rewritten as equation (3).

$$\ln(\frac{\Delta V}{V_0}) = \ln(1 - \frac{\rho_0}{\rho_t}) = C + n\ln t \tag{3}$$

where ρ_0 and ρ_t are initial and final densities of the specimen, C is a constant depending on temperature and particle size.

The green HA specimens fabricated the same way as described in chapter 4 were sintered at 1360°C for 1, 5, 12, 20, 23, 27, and 30 minutes respectively. A powder bed about ~3 mm thick was employed both beneath and on top of the specimens. The sintering boat was always kept in the center bottom of the furnace chamber. The density of HA specimens were calculated from density and dimensions measurement as described in previous chapters.

The sintering profiles (temperature, time and ramp rate) and the calculated values of density/porosity as well as volume change are given in Table C-1. The average density/porosity is calculated from three specimens.

Table C-1 List of sintering profile, density, porosity and volume change

Temperature (ºC)	Time (min)	Average Density(%)(N*=3)	Porosity (%)	Ramp (ºC/min)	$\Delta V/V_0$	$\ln(\Delta V/V_0)$	lnt
Green	0	40	60		0		
1360	1	72.16	27.84	10	0.445676	-0.80816	0
1360	5	76.59	23.41	10	0.477739	-0.73869	1.609438
1360	12	82.69	17.31	10	0.516266	-0.66113	2.484907
1360	20	84.52	15.48	10	0.526739	-0.64105	2.995732
1360	27	87	13	10	0.54023	-0.61576	3.295837
1360	30	88.5	11.5	10	0.548023	-0.60144	3.401197

The last two columns $\ln(\Delta V/V_0)$ and lnt in Table C-1 are plotted as shown in Figure C-1. The data were fit to equation (3) via least squares technique, which yielded C=0.8175 and n = 0.0608±0.0042.

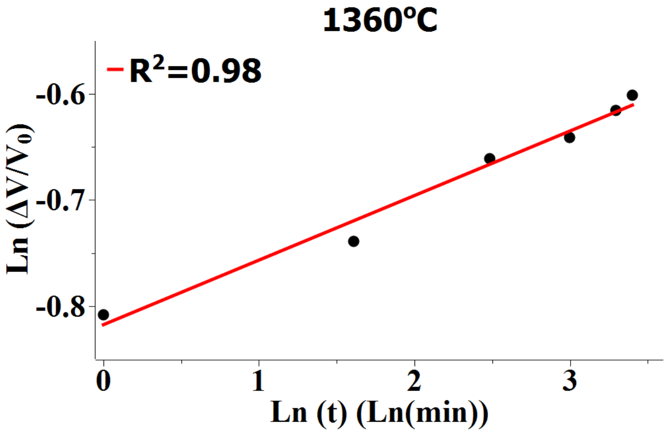

Figure C-1 The logarithm of volume change increases linearly with the logarithm of time. The data were fit to equation (3). The coefficient of determination $R^2 = 0.98$.

For the HA powders used in our group, any desired density could be obtained fairly well by referring to the relationship between volume change and sintering time as shown in Figure C-1.

REFERENCES

REFERENCES

[Barsoum 2003] Barsoum MW. Fundamentals of Ceramics. Institute of Physics Publishing 2003; 302-318.

[Benbrahim et al. 1994] Benbrahim AL, Italien GJ, Milinazzo BB, WarnockDF, Dhara S, Gertler JP, Orkin RW, Abbott WM. A compliant tubular device to study the influences of wall strain and fluid shear stress on cells of the vascular wall. Journal of Vascular Surgery 1994; 20: 184-194.

[Brown TD 2000] Brown TD. Techniques for mechanical stimulation of cells in vitro: a review, Journal of Biomechanics 2000; 33: 3-14.

[Dong et al. 2001] Dong J, Uemura T, Koji H, Kikuchi M, Tanaka J, Tateishi T. Application of low-pressure system to sustain in vivo bone formation in osteoblast porous hydroxyapatite composite. Materials Science and Engineering 2001; C17: 37-43.

[Ehrlich and Lanyon 2002] Ehrlich PJ and Lanyon LE. Mechanical strain and bone cell function: a review. Osteoporos is Intetnational 2002; 13: 688-700.

[Fritton and Rubin 2001] Fritton SP and Rubin CT. In vivo measurement of bone deformations using strain gauges. In: Cowin SC, eds. Bone mechanics handbook. Boca Raton, FL: CRC Press, 2001: 8-10-8-34.

[Frost 1964] Frost HM. The Laws of Bone Structure. Spring field, IL: Thomas; 1964.

[Iqbal and Zaidi 2005] Iqbal J and Zaidi M. Molecular regulation of mechanotransduction, Biochemical and Biophysical Research Communications 2005; 328: 751-755.

[Klein-Nulend et al. 1998] Klein-Nulend J, Helfrich MH, Sterch JG et al. Nitric Oxide response to shear stress by human bone cell cultures is endothelial nitric oxide synthase dependent. Biochem Biophys Res Commun 1998; 250: 108-14.

[Lanyon 1992] Lanyon LE. The success and failure of the adaptive response to functional loading-bearing in averting bone fracture. Bone 1992; 13: S17-S21.

[Liskova nad Hert 1971] Liskova M and Hert J. Reaction of bone to mechanical stimuli. Part 2. Periosteal and endosteal reaction to tibial diaphysis in rabbit to intermittent loading. Folia Morphol 1971; 19: 301-317.

[Nesbitt et al. 2009] Nesbitt RSA, Macione J, Debroy A, Kotha SP. Bone generation through mechanical loading, World Academy of Science, Engineering and Technology 2009; 58: 125-127.

[Ralston 1997] Ralston SH. The Michael Mason Prize Essay 1997. Nitric oxide and bone: what a gas! Br J Rheumatol 1997; 36: 831-8.

[Robling and Turner2009] Robling AG and Turner CH. Mechanical Signaling for Bone Modeling and Remodeling. Critical Reviews in Eukaryotic Gene Expression 2009; 19: 319-338.

[Rubin and Lanyon 1984] Rubin CT and Lanyon LE. Regulation of bone formation by applied dynamic loads. J Bone Jt Surg 1984; 66A: 397-402.

[Rubin and Lanyon 1985] Rubin CT and Lanyon LE. Regulation of bone mass by mechanical strain magnitude. Calcif Tissue Int 1985; 37: 411-417.

[Rubin and McLeod 1994] Rubin CT and McLeod KJ. Promotion of bony ingrowth by frequency specific, low-amplitude mechanical strain. Clin Orthop Rel res 1994; 298: 165-174.

[Shivaram et al. 2010] Shivaram GM, Kim CH, Batra NN, Yang W, Harris SE and Jacobs CR. Novel early response genes in osteoblasts exposed to dynamic fluid flow. Phil Trans R Soc A 2010; 368: 605-616.

[Song et al. 2007] Song G, Ju Y, Soyama H, Ohashi T and Sato M. Regulation of cyclic longitudinal mechanical stretch on proliferation of human bone marrow mesenchymal stem cells. MCB 2007; 4: 201-210.

[Thomson 1917] Thompson D. In : Bonner JT Ed. On Growth and Form (Ambridged Edition). Cambridge Press; 1917;

[Turner et al.1995] Turner CH, Owan I, and Takano Y. Mechanotransduction in bone: Role of strain rate 1995; 269: 438-442.

[Umemura et al. 1997] Umemura Y, Ishiko T, Yamauchi T, Kurono M, and Mashiko S. Five jumps per day increase bone mass and breaking force in rats. J Bone Miner Res 1997; 12: 1480-1485.

[Walsh 1955] Walsh A. The application of atomic absorption spectra to chemical analysis. Spectrochim Acta 1955; 7: 108-117.

[Wolff 1892] Wolff J. Das Gesetz der Transformation der Knochen. Berlin : Hirschwald. 1892.

[Zaman 1999] Zaman G, Pitsillides AA, Rawlinson SC et al. Mechanical strain stimulates nitric oxide production by rapid activation of endothelial nitric oxide synthase in osteocytes. J Bone Miner Res 1999; 14: 1123-31.